A geochemical investigation of regional sedimentary-hosted Pb-Zn mineralization in the Paleoproterozoic Karrat Group, West Greenland

A Thesis Submitted to the
College of Graduate and Postdoctoral Studies
in Partial Fulfillment of the Requirements
For the Degree of Master of Science
In the Department of Geological Sciences
University of Saskatchewan, Saskatoon

By

Ty Magee

I. PERMISSION TO USE:

In presenting this thesis/dissertation in partial fulfillment of the requirements for a Postgraduate degree from the University of Saskatchewan, I agree that the Libraries of this University may make it freely available for inspection. I further agree that permission for copying of this thesis/dissertation in any manner, in whole or in part, for scholarly purposes may be granted by the professor or professors who supervised my thesis/dissertation work or, in their absence, by the Head of the Department or the Dean of the College in which my thesis work was done. It is understood that any copying or publication or use of this thesis/dissertation or parts thereof for financial gain shall not be allowed without my written permission. It is also understood that due recognition shall be given to me and to the University of Saskatchewan in any scholarly use which may be made of any material in my thesis/dissertation.

Requests for permission to copy or to make other uses of materials in this thesis/dissertation in whole or part should be addressed to:

Head of the Department of Geological Sciences
114 Science Places
University of Saskatchewan
Saskatoon, Saskatchewan S7N 5E2
Canada

OR

College of Graduate and Postdoctoral Studies
University of Saskatchewan
105 Administration Place
Saskatoon, Saskatchewan S7N 5A2
Canada

II. Abstract

Pb-Zn mineralization is hosted in two formations of the Karrat Group in arctic West Greenland: the Marmorilik Formation (carbonate-hosted, 12.3% Pb, 4.0% Zn, 29ppm Ag), home to the historical Black Angel Mine, and the recently defined Qaarsukassak Formation (shale-carbonate-hosted, ~20% Zn). These two sedimentary units were deposited directly on crystalline basement rocks and might have similar depositional timing, however, they are separated by a basement topographic high and are not observed in stratigraphic contact. The timing of their mineralization is also enigmatic. This study uses a combination of field and geochemical approaches to understand the origin of the Pb-Zn mineralization in both formations by using the following methods: field mapping, petrography, pyrite and ore sulfide sulfur isotope analysis, Pb isotopic analysis, and Re-Os analysis of pyrite grains associated with the mineralization. Marmorilik and Qaarsukassak mineralization textures suggest a late stage remobilization event after the emplacement of ore mineralization. Additionally, remobilized sulfides from both formations are linked to the regional D3 deformation, thus constraining the mineralization prior to D3 deformation. Sulfur isotope results from both traditional isotope-ratio mass spectrometry and secondary ion mass spectrometry show a range of $\delta^{34}S$ values between +0.2‰ and +7.2‰ on sulfide minerals, suggesting contributions from both bacterially reduced and thermochemically reduced seawater sulfate. Pb-Pb isotopic analysis of galena from the Marmorilik Formation shows a homogenous signature ($^{206}Pb/^{204}Pb$ = 16.091-16.102 and $^{207}Pb/^{204}Pb$ = 15.378-15.385), with Pb isotopic compositions consistent with a crustal source for Pb, indicating local basement as a likely source for the metals. Results from Re-Os analysis of pyrite grains derive an indicated age of 1919 Ma ± 44 Ma, providing a maximum age constraint for the mineralization. Combining structural, petrographic, and Re-Os isotopic data, a timeframe for the Pb-Zn mineralization of ca. > 1900 to < 1830 Ma is proposed. Sulfur isotope results suggest a SEDEX model for the mineralization, while petrographic, Pb-Pb, and Re-Os isotope results could indicate either a SEDEX or MVT type model.

III. Acknowledgments

This study was supported logistically and financially by several sources including the Geological Survey of Denmark and Greenland (GEUS), the Ministry of Mineral Resources (MMR), the NSERC Discovery Grant (to Dr. Camille Partin), the Mineralogical Association of Canada student research grant, and the Saskatchewan Opportunity and Innovation award scholarship (to Ty Magee).

The completion of this thesis would not have been possible without the help and support I've receive over the past couple of years from my colleagues, family, and friends.

Helpful correspondence and thoughtful discussions with several researchers from the Karrat Zinc project, namely Michelle DeWolfe, Pierpaolo Guarnieri, Jochen Kolb, Diogo Rosa, Crystal LaFlamme, Annika Dziggelm, and Robert Zimmermann were incredibly useful and helpful in understanding the huge complexity that is the geology of the Karrat Group area. It was an amazing experience to do field work and research among such talented geologists.

I would also like to thank my committee members, Dr. Kevin Ansdell and Dr. Bruce Eglington for providing endless support and valuable advice throughout this project and various other projects throughout my time as a student here at the University of Saskatchewan. A special acknowledgment to my long and suffering editor, supervisor, and mentor, Dr. Camille Partin (and her "associates", Hastings and Cashew) who provided outstanding support, direction, and the right balance of "tough love" and sympathetic support throughout this entire process. I am fortunate to have the opportunity to be one of your graduate students. Thank you very much.

IV. Table of Contents

V. List of Tables

VI. List of Figures

VII. List of Abbreviations

AZ - Angel ore zone

BHT – Broken-Hill type deposit

BSE – Backscatter electron detector

BSR – Bacterial sulfate Reduction

Cpy – Chalcopyrite

DISC – Discovery Proper

DIZ – Deep Ice ore zone

Gn – Galena

Hem- Hematite

IRMS – Isotope ratio mass spectrometry

IZ – I ore zone (part of Angel ore zone)

MC-ICP-MS - Multi- collector inductively coupled mass spectrometry

MVT – Mississippi-Valley type deposit

PIC – Proven Igneous Complex

Po – Pyrrhotite

Py – Pyrite

Qtz- Quartz

SEDEX – Sedimentary-exhalative deposits

SEM – Scanning electron microprobe

SIMS – Secondary ion mass spectrometry

SLO – South Lakes outcrop

Sph – Sphalerite

Trem – Tremolite

TSR – Thermochemical sulfate reductio

1.0 Introduction

The Black Angel Mine, one of the larger Precambrian Pb-Zn mines in the world, produced 11.2 million tonnes (Mt) of Pb-Zn-Ag ore from 1973-1990. After production ceased, exploration north of the Black Angel Mine resulted in finding the "discovery zone," an anomalous Pb-Zn source, hosted in a carbonate sequence thought to be similar to the Marmorilik Formation (Coppard et al., 1992). This stratigraphic unit was later defined and named the Qaarsukassak Formation (Guarneri et al., 2016). While relatively proximal, the relationship between the two formations with respect to their mineralization and stratigraphy are unclear, since outcrops of the Marmorilik and Qaarsukassak formations are not connected or interbedded. Furthermore, a deposit model for the Black Angel Mine and the Pb-Zn mineralization hosted in the Qaarsukassak Formation is not well-defined. This is partly due to the host rocks being poly-deformed, and metamorphosed at greenschist facies conditions, consequently remobilizing the ore (Pedersen 1980,1981) and effectively erasing most of the primary ore textures. This is problematic as primary ore textures can help identify syngenetic or epigenetic relationships, which are critical in categorizing specific deposit type, such as sedimentary-exhalative deposits (SEDEX) or Mississippi-Valley type (MVT) deposits.

Recent exploration endeavors around the Black Angel Mine combined with motivations from the Greenlandic government to further develop potential mineral resources helped establish the Karrat Zinc project, jointly led by the Geological Survey of Denmark and Greenland (GEUS) and the Ministry of Mineral Resources (MMR). This project encompasses multiple disciplines such as stratigraphy, structural geology, geochronology, detailed mapping, and isotope geology to revise previous work (Henderson and Pulvertaft, 1967) in order to better understand basin development during deposition of the Karrat Group, which can aid in understanding the genesis of the Black Angel deposit and other various mineral potential within the Karrat Group (e.g., Rosa et al., 2017).

The purpose of this study is to understand the origin of the Pb-Zn mineralization in both the Marmorilik and Qaarsukassak formations by defining their isotopic geochemical characteristics and field relationships. This M.Sc. thesis encompasses a combination of

approaches, both field and geochemical: (1) Geologic mapping to generate a 1:10,000 scale map of the Qaarsukassak Formation within the Kangerluarsuk Fjord in its type locality (Figure 1.1); (2) A petrographic analysis on seven different ore bodies from Black Angel as well as outcrop samples from both Black Angel and Qaarsukassak to determine a paragenetic sequence; 3) Sulfur isotope analysis on ore sulfides to determine the main source(s) of sulfur; 4) Pb-Pb isotopic analysis to determine the possible source(s) of Pb; and 5) Re-Os geochronology to constrain the age of the Pb-Zn mineralization.

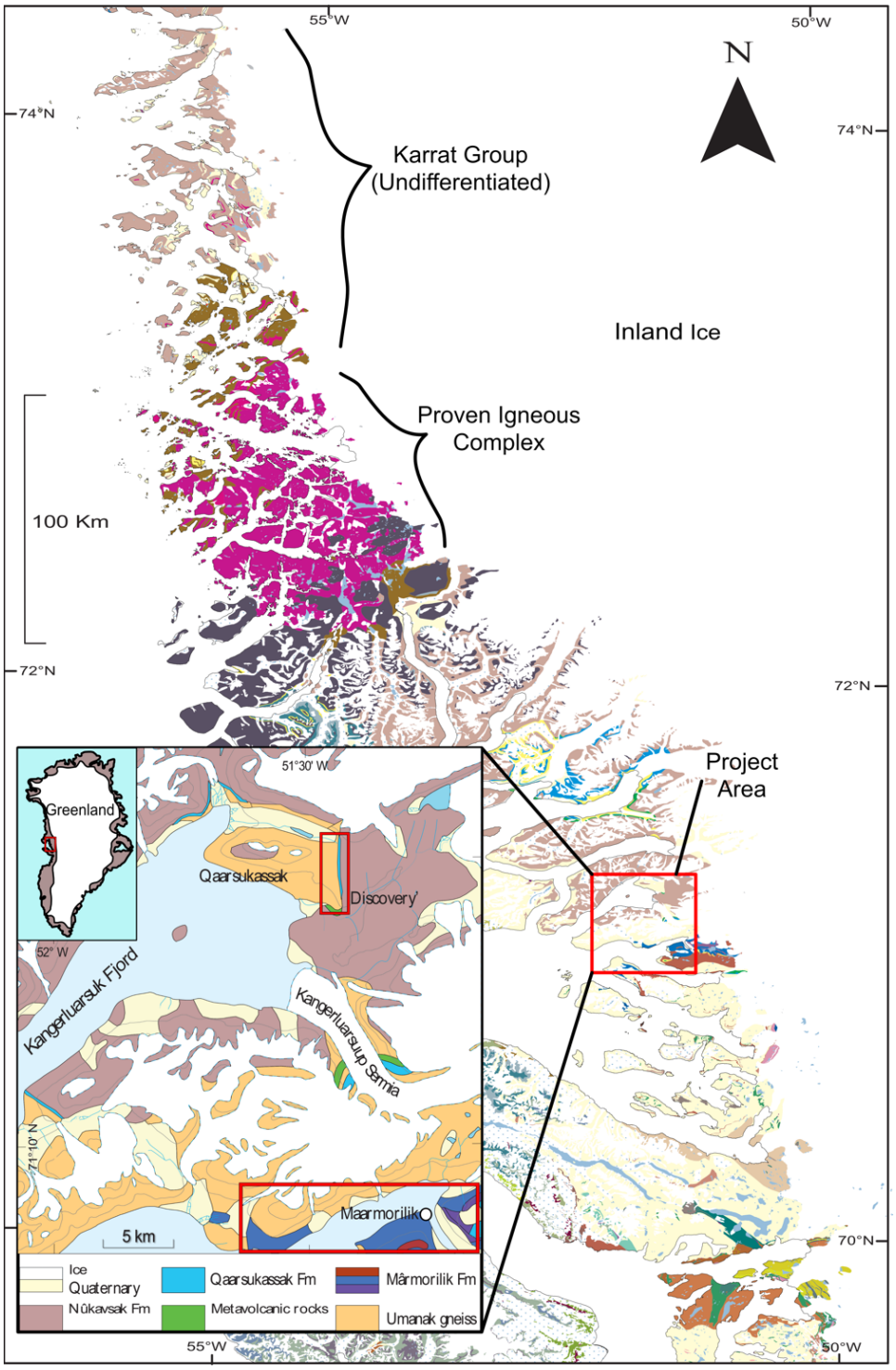

Figure 1.1 Simplified regional geological map of the Karrat Group project area. Highlighted localities include the Qaarsukassak Formation (noted as 'Discovery'), and the Marmorilik Formation, host of the Black Angel Mine (modified from Guarneri et al., 2016).

1.1 Research Objectives and Hypotheses

1) Field Mapping in Greenland

Objectives:

a) Identify structures that could link the structural history of the Marmorilik and Qaarsukassak formations;

b) If the mineralization in both formations have a structural connection, it can be suggested that the two units might host the same mineralization event or at least achieve a relative age constraint for the mineralization.

2) Petrographic analysis

Objectives:

a) Determine a paragenetic sequence based on a sample set comprised of GEUS archive ore sulfides and those collected in the field.

b) Determine if multiple generations of sulfides occurred, indicating the possibility of one or more mineralization events.

3) Sulfur isotope analysis on ore sulfides

Objective: Determine the district's main source of sulfur.

Hypotheses:

1. Assuming the coeval (~1.9 Ga) seawater sulfate value is 21‰ (Farquhar et al., 2010). If the $\delta^{34}S$ data yield values between +7‰ and +21‰ (VCDT), then the sulfur is likely derived from a hydrothermal or abiotic component, which would favor a MVT type model of genesis.

2. If the $\delta^{34}S$ data yield values lower than +7‰ (range of +7 to -20‰), sulfur is likely derived from bacterial sulfate reduction, indicating a synsedimentary origin, and favoring a SEDEX model of genesis.

3. A wide spread of $\delta^{34}S$ values can indicate that the sulfur source is sedimentary or at least not from a magmatic source, the latter of which would be expected to give a narrow range of values around 0‰ (± 4‰).

4) Pb-Pb Isotope analysis on galena

Objective: Determine model ages and whether the Pb in the galena is derived from the same source (co-genetic) for the two formations. Homogenous data within each deposit

would indicate a single source of Pb that favors a SEDEX model. Heterogeneous data would indicate multiple sources of Pb more indicative of a MVT model.

Hypothesis: If the Pb-Pb data from the two formations are similar, the Pb-Zn mineralization was derived from the same source, indicating a co-genetic relationship.

5) Re-Os geochronological dating of pyrite genetically linked to the ore sulfides

Objective: Determine the Pb-Zn mineralization age.

Hypotheses:

1. If the determined age is coeval with its host rock or post-dates its host rock, this would suggest Pb-Zn mineralization is syngenetic or epigenetic, respectively.

2. If pyrite selected for the analysis was crystallized after the main Pb-Zn mineralization or recrystallized during metamorphism, this will provide a minimum age of mineralization or the timing of remobilization, respectively.

1.2 Scope of Research

The goal of this thesis is to better understand the Pb-Zn mineralization in the Karrat Group, and to answer hypotheses related to the source of sulfur and lead, possible stages of fluid mixing (i.e., multiple sources), and ultimately if the mineralization at Black Angel is related to that of the Qaarsukassak Formation. From this, a deposit model for Pb-Zn mineralization for the Karrat Group is developed. This work aims to provide better exploration parameters for future Pb-Zn mineralization exploration in the Karrat Group.

2.0 Literature Review on Sedimentary-Hosted Deposits

Sedimentary-hosted Pb-Zn deposits are a diverse group of ore deposits, which are hosted by an array of siliciclastic and carbonate rocks with no direct association to igneous activity (Leach et al., 2010), with the main economic ore sulfides comprised of sphalerite ((Zn, Fe) S), galena (PbS), ± silver (Ag), and chalcopyrite ($CuFeS_2$). Sedimentary-hosted deposits are one of the world's most important lead and zinc resources, accounting for ~75% of the world's reserves of these commodities (Singer, 1995). There are two main classes of sediment-hosted ore deposits: sedimentary exhalative (SEDEX) and Mississippi Valley type (MVT), but have been further classified into sub-type deposits, including Irish-Type Zn-Pb and Broken-Hill Type (BHT) deposits. Irish-Type deposits fall into a sub category that lies between SEDEX and MVT deposits. BHT deposits fall under a sub-category of SEDEX deposits. This chapter briefly discusses the processes, controls, and characteristics that identify these different types of sedimentary–hosted deposits and identify a possible deposit model consistent with characteristics of the Pb-Zn mineralization in the Karrat Group.

2.1.0 Sedimentary Exhalative Deposits (SEDEX*)*

The term SEDEX was first introduced by Carne and Cathro (1981), describing laminated, exhalative sulfides in fine grained clastic rocks that formed by venting of ore fluids onto the seafloor. The "SEDEX" term has garnered a lot of debate, as noted in a previous study on sediment-hosted deposits from Leach et al. (2005). Leach et al. (2010) argued that the term is unsatisfactory because some deposits traditionally classified as SEDEX, did not form from a sulfide exhalative. The term clastic-dominated (CD) Pb-Zn was proposed instead of SEDEX, as it is a descriptive classification that does not automatically suggest a genetic link to an exhalative process. For simplicity, this thesis will use the term SEDEX.

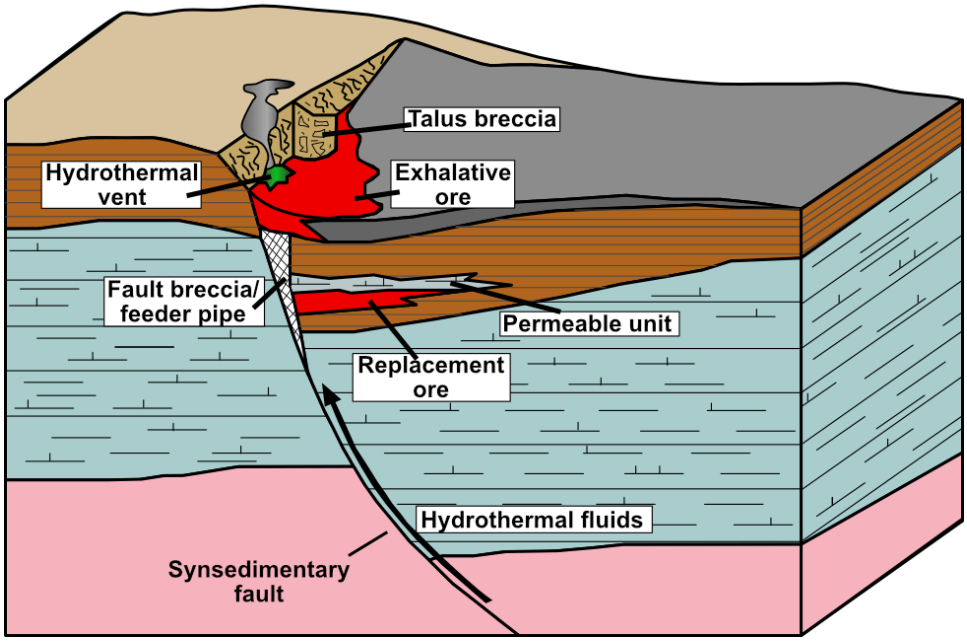

Figure 2.1 Schematic diagram illustrating features in a typical SEDEX deposit (modified from Wilkinson, 2014).

2.1.1 Size and Distribution

SEDEX deposits are an important resource, since these deposits comprise over ~50% of the world's zinc and lead reserves (Goodfellow, 2004). These deposits generally have higher tonnage of ore sulfides compare to MVT deposits (Figure 2.2) that can be as high as up to 35Mt (Leach et al., 2005). These deposits are not distributed evenly throughout the geologic history, clustering mainly in the Paleozoic-Mesozoic and Proterozoic eras (Leach et al., 2005) (Figure 2.2). Absence of these deposits in the rest of the Earth's history could be due to many contributing factors such as restricted sulfate supply, lack of passive margins forming, global atmospheric anoxia conditions, and tectonic regimes (Farquhar et al., 2010).

2.1.2 Settings & Characteristics

SEDEX deposits occur in two broad settings: intracontinental rifts (or failed rifts) and passive continental margins (Wilkinson, 2014). An example for a failed rift system would be the mineralized basins in Northern Australia such as Mt. Isa-McArthur basin system (Large et al.,

2005). These basins can generally be very thick rift packages, dominated in the lower part by oxidized clastic rocks and minor mafic volcanics overlain by dolomites, evaporitic and ferruginous siltstones, and reduced carbonaceous and pyritic shales. Passive continental margins are characterized by basins that are compartmentalized into sub-basins by extensional faults. Basinal sequences comprises of rift- and sag-fill deposits with a basal clastic and/ or volcanic dominated rocks, overlain by host rocks comprised of deeper water reduced siltstones, mudstones, and later carbonates. Examples of these passive margins can be found in North America in the Selwyn Basin (Goodfellow et al., 1993). SEDEX mineralization can be hosted in a variety of different rock types: shale, carbonates, calcareous/organic rich siltstones, and even sandstones.

SEDEX deposits are confined in sub-basins controlled by synsedimentary faults. These fault zones provide the principal conduits for buoyant mineralizing fluids, migrating from greater depths within, or below the host basin in the basement (Figure 2.1). Hydrothermal reservoirs are activated by a tectonic event, triggering major rifts and able to vent oxidized fluids, carrying Fe, Zn, and Pb as chloride complexes and variable SO_4 through leaching from aquifer sediments and volcanic rocks (Goodfellow, 1987). As the fluid reaches to the sub-surface, it is introduced into a cool, H_2S rich environment, producing a redox reaction, thus precipitating the base metal sulfides (Goodfellow, 1987; Goodfellow and Lydon, 2007). SEDEX deposits are classified to have no direct link with igneous activity, however tuffs from distal volcanism and mafic intrusions of similar age to mineralization are known. (Leach et al., 2005).

Ore textures can normally be found as fine grained, layered, and banded with or without coarser grained brecciated, veined, fragmental, or chaotic textures (Leach *et al*., 2005). These textures suggest a syngenetic-syndiagenetic age for the mineralization. Radiometric dating (e.g. Re-Os geochronology) of these deposits also confirms the syngenetic nature of SEDEX Deposits (Taylor et al., 2009; Morelli et al., 2004).

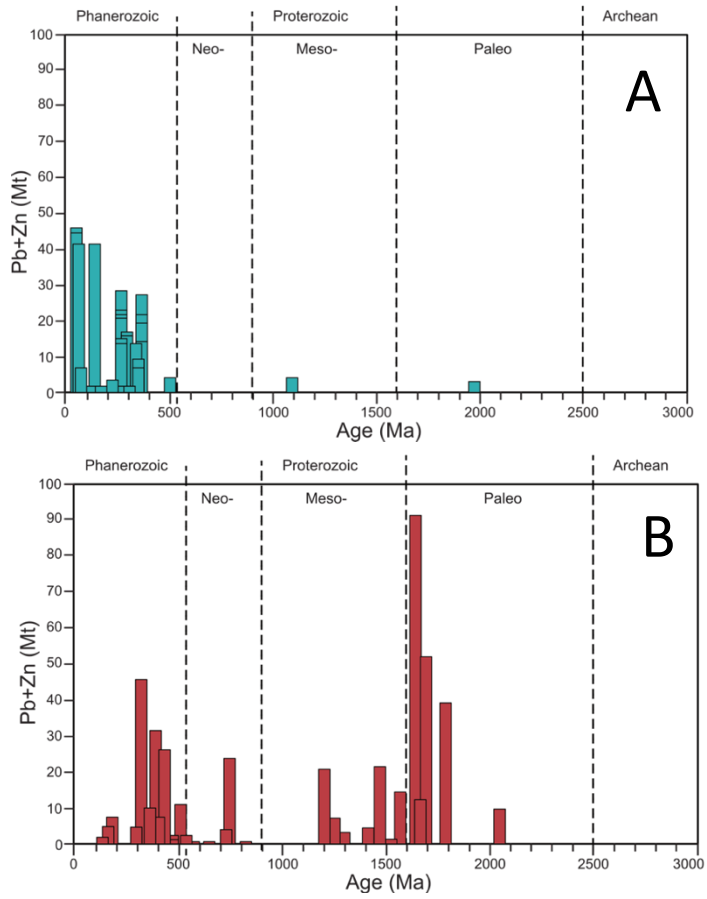

Figure 2.2 Bar diagram showing the secular ages, tonnages and temporal distribution of A) MVT and B) SEDEX deposits worldwide (data from Taylor *et al*., 2009; diagrams after Leach *et al*., 2010).

2.2.0 Mississippi Valley Type Deposits

The Mississippi Valley Type (MVT) deposit name is credited to the fact that several classic districts are located in the drainage basin of the Mississippi River in central United States (Leach et al., 2005). The genesis of MVT deposits convened a lot of debate with multiple interpretations, summarized in Snyder (1967), Ohle (1980), and Leach et al. (2010). MVT deposits are commonly accepted as a dominantly carbonate-hosted deposit with epigenetic origin and usually connected with large scale tectonic events (Leach *et al*., 2001).

2.2.1 Size and Distribution

Leach et al. (2010) estimated that MVT deposits comprises of ~24% of the known global resources of Zn and Pb, as well as ~2.9% of Ag. MVT deposits are characteristically distributed over 100's of km^2 that defines an individual ore district (Leach et al., 2005). These deposits generally have a lower tonnage of ore sulfides when compared to SEDEX deposits, averaging between 5-10 Mt but can be up to over 20 Mt (Figure 2.2). Distribution of MVT deposits can be seen throughout geologic time although they occur dominantly in the Phanerozoic Era.

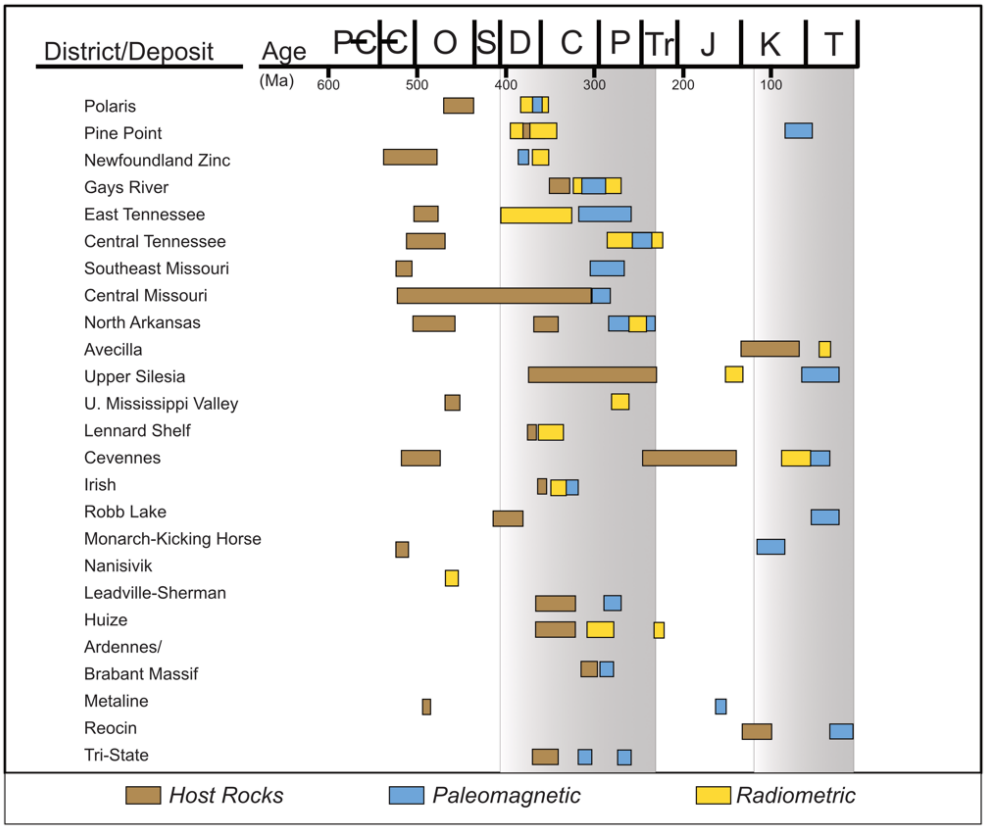

Figure 2.3. Diagram illustrating the distribution of radiometric and paleomagnetic ages of MVT deposits and their host rocks in the Phanerozoic era (after Leach et al., 2010).

The massive presence of MVT deposits in the Phanerozoic has been linked to the development of extensive carbonate platforms and the rise of seawater sulfate (Farquhar, 2010; Kesler and Reich, 2006). Although extensive carbonate platforms were developed in the Paleoproterozoic, Grotzinger (1989) suggested that they are not favorable host rocks because of low permeability linked to early diagenetic dolomitization and silicification, as well as a lack of bioturbation in comparison to Phanerozoic host rocks.

2.2.2 Settings

MVT deposits are typically hosted in platform carbonate sequences in the foreland of orogenic belts. The type of foreland is not considered critical to ore formation, with deposits interpreted to be associated with collisional, Andean, and transpressional orogens (Bradley and Leach, 2003). Bradley and Leach (2003) discuss three stages that are often linked to the origin of mineralization: (1) the development of unconformities and associated karstification due to migration of a forebulge; (2) the formation of extensional and/or wrench faults in the stretched forebulge region; and (3) the proximity to a mountain belt and development of a regional slope toward the foreland (Figure 2.4).

The true mineralization ages of MVT deposits have been widely debated (Leach *et al*., 2001). Radiometric dating (Re-Os, U-Pb, U-Th in calcite, Rb-Sr in sphalerite, K-Ar on feldspar and clay minerals) as well as paleomagnetic dating have provided better age constraints on the timing of mineralization (Leach *et al*., 2001). Characteristic mineralization ages for MVTs can be from 10's to 100's of million years younger than the host rock (diagenetic to epigenetic) (Figure 2.3).

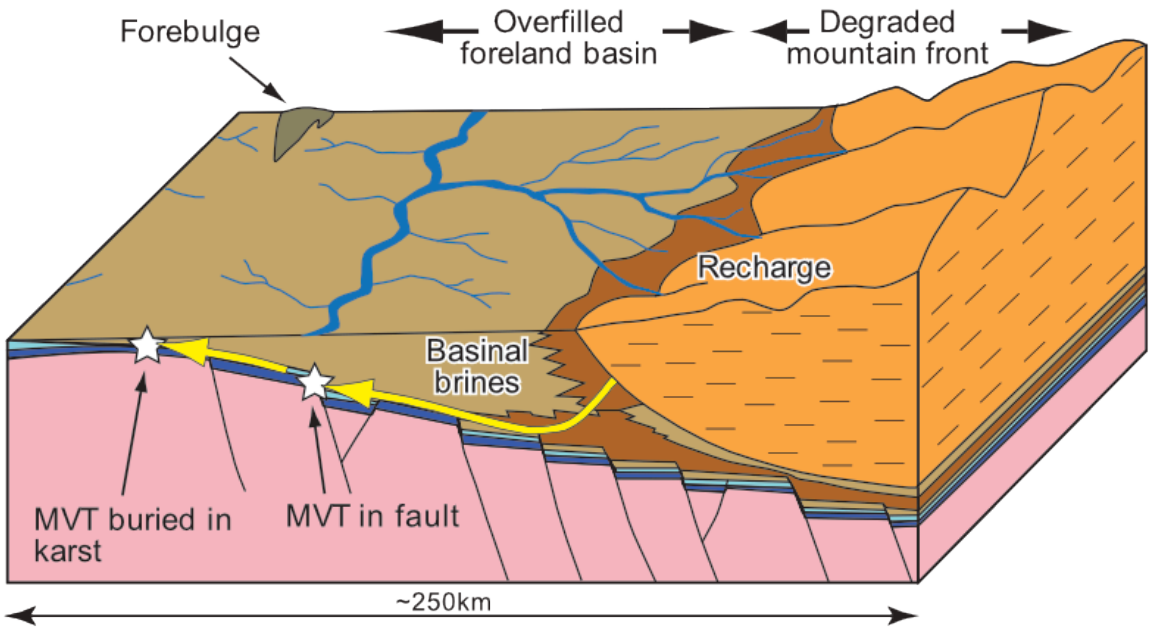

Figure 2.4. Schematic diagram illustrating the post-collisional tectonic stage for MVT ore genesis. Permeable carbonates provide ideal host rocks for mineralization, precipitated from connate brines migrating away from the eroding mountain belt (modified from Wilkinson, 2014).

2.3.0 Secondary Classifications

2.3.1 Irish-Type Zn-Pb deposits

Irish-type deposit name and classification originated in the early 1970's from the Zn-Pb-Ba deposits in the Irish Midlands (Hitzman and Large, 1986). In terms of origin, these deposits have always been controversial. They have been described in the past as exhalative, SEDEX, synsedimentary, syndiagenetic, epigenetic, MVT, and Irish-type deposits which can cause confusion. Deposits that have been classified as an Irish-type deposit include: Recon and Troya (Spain, Morro Agudo (Brazil), and Prairie Creek (Canada). The following will focus on looking at the Irish Midlands ore field for key descriptions and classification of Irish-type ore deposits.

The tectonostratigraphic setting of Irish-type deposits are hosted in carbonate ramps and extensional basins. Host rocks can be non-argillaceous carbonates within a mixed carbonate-siliciclastic succession. These deposits are mostly developed on the margins of km-scale sub-

basins controlled by synsedimentary faults. This paleotopography is still reflected today in the Irish Midlands.

Leach et al. (2005) suggests two features stand out in Irish-type deposits in comparison to MVT deposits: 1) The age of mineralization in Irish-type are syn-genetic to syn-diagenetic relative to the host rocks; and 2) strongly negative $\delta^{34}S$ values, which are distinctly different than typical MVT ores. Leach et al. (2005) suggests that classifying Irish-type as its own deposit classification is a "philosophical debate" in whether it is worth splitting this deposit type from the main MVT deposit classification. Wilkinson (2014) argues Irish-type deserves its own classification and merit. Wilkinson (2014) also describes the many similarities between SEDEX deposits and Irish-type such as forming in intracratonic submarine settings in second or third order basins undergoing active extensional faulting, replacement textures, homogenous Pb isotopes within individual deposits, and an indirect temporal link to igneous activity.

2.3.2 Broken Hill-Type Deposits (BHT)

Broken Hill-type (BHT) deposits are regarded as a category of SEDEX deposits. Some have argued that Broken-Hill-type deposits are sufficiently different compared to other SEDEX deposits and warrant a separate classification (Parr et al., 2004; Large et al., 2005). Large *et al*, (2005) compared each of these deposits and found that BHT deposits contain significantly higher contents of Ag and Pb relative to the SEDEX category. They also found several characteristic features of BHT deposits: 1) Host rocks are amphibolite-granulite facies of Paleo- to Mesoproterozoic clastic sedimentary sequences; 2) A spatial association with amphibolites and felsic gneisses interpreted as probable metavolcanic rocks; 3) Relationships with thin, laterally extensive marker units such as quartz-gahnites and iron formations; 4) No apparent significant association with reduced graphitic or pyritic stratigraphy; 5) Stacked ore lenses modified by structural overprints; 6) a general lack of pyrite within ore lenses; and 7) extreme zonation between Pb-Ag- versus Zn- dominate ore lenses.

The extent of the differences listed reflect metamorphic and structural overprinting and reworking of a SEDEX protolith. Large et al. (1995) argued that the significant difference between SEDEX and BHT deposits relates to the redox difference between ore fluid and sedimentary environments. Leach et al. (2005) model of BHT deposit interpretation is forming with reduced

H_2S bearing metalliferous brines that were exhaled in oxic sedimentary environments. This is supported by the lack of pyritic host sequences, magnetite bearing iron formations, occurrences of well-developed of Mn halos and a restricted range of $\delta^{34}S$ values.

2.4.0 Possible Karrat Group Models

The mineral deposit model for Black Angel Mine and the mineralization hosted in the Qaarsukassak Formation are not well-defined. Rosa et al. (2017) propose a MVT deposit model for the mineralization hosted in Marmorilik and Qaarsukassak formations. This is based on the observation that marble and chert horizons control mineralization in the Marmorilik Formation, hypothesizing silicification of evaporites and the presence of Archean basement rocks. Conversely, Pedersen (1980) located apparent primary banded ore (Figure 2.4) in the center of the Angel ore zone with the ore parallel and rhythmic to layers of enclosed marbles with a sharp and comfortable contact. Relict microstructures were also observed in etched pyrite from the banded ore, including polyframboidal pyrite (or "rogenpyrite"), nuclei of quartz grains in pyrite grains, and skeletal pyrite. Pedersen (1980) suggests that these textures reflect a preserved depositional feature that inclines towards a syngenetic-syndiagenetic deposition model.

The typical characteristics that define SEDEX and MVT such as epigenetic vs. syngenetic mineralization, and ore body textures are difficult to differentiate as age of the Pb-Zn mineralization relative to its host rocks is poorly constrained in the Karrat Group and regional deformation and remobilization events possibly erased most of the primary ore textures. Ore textures would need to be re-examined in the mine (currently inaccessible) through a detailed study on the ore bodies.

Based on the classifications of each deposit type (Table 2.1), using sulfur and lead isotope data could prove to be useful to aid in classifying the Karrat Group mineralization in one of these categories, which will be further discussed in chapter 4.

Table 2.1. Summary and comparison of principal characteristics of SEDEX, MVT, Irish-type, and BHT deposits (modified after Wilkinson, 2014).

Features	***SEDEX (Leach et al., 2005)***	***MVT (Leach et al., 2005)***	***Irish-type (Wilkinson, 2014)***	***BHT (Leach et al., 2005)***
Tectonostratigraphic Setting (at the time of mineralization	Intracontinental or failed rift continental margins	Platform carbonate sequence at flanks of basin or foreland thrusts	Carbonate ramp and extensional basins on extending continental margin	Intracontinental or failed rift continental margins
Host Rocks	Shales, carbonates, calcareous/organic-rich siltstones, less commonly sandstone and conglomerate	Mainly dolostones and limestone rarely sandstone in carbonate sequences	Non-argillaceous carbonates within mixed carbonate-siliciclastic succession	Metashales, sandstones, banded iron formations (BIF), metavolcanics, amphibolites
Structural Controls	Synsedimentary faults controlling sub-basins and associated fractures and breccias	Normal, transtensional, and wrench faults and associated fractures and breccias	Synsedimentary faults controlling sub-basins and associated fractures and breccias	Synsedimentary faults controlling sub-basins and associated fractures and breccias
Principal ore and gangue minerals	Sphalerite, galena, pyrite, pyrrhotite, marcasite, minor sulfosalts, chalcopyrite +calcite, siderite, dolomite, ankerite, and quartz. Barite is common to absent; apatite is sometimes common and fluorite is very rare	Sphalerite, galena, pyrite, marcasite, minor sulfosalts + dolomite, calcite. Barite is minor to absent and fluorite is rare	Sphalerite (Low Fe), galena, pyrite, marcasite, minor sulfosalts, chalcopyrite+ dolomite, calcite, quartz. Barite is common, locally economic. Fluorite is extremely rare	Sphalerite, galena, pyrrhotite, silver +silicates minor to major magnetite and Mn garnet. Generally, lacks pyrite lenses
Texture	Bedding-parallel, fine grained, layered, and banded textures with or without coarser-grained brecciated, veined fragmental, or chaotic textures	Coarsely crystalline to fine grained, massive to disseminated. Replacement and open space filling	Dominated by massive sulfide but highly variable and complex textures. Mostly replacement, common veins and open space filling	Dominantly coarse and remobilized
Lead Isotope signature	Within-deposit homogeneity; relatively unradiogenic crustal Pb	Within deposit heterogeneity; crustally derived,	Within-deposit homogeneity; regionally variable,	Homogenous mantle source; Pb might be mantle derived

		highly radiogenic in the United States and Canada	relatively unradiogenic crustal Pb	
Sulfur Isotope Signature	Predominately positive but can have negative values; reduced seawater sulfate (BSR +/- TSR) in host rock or second fluid	Predominately positive; reduced seawater sulfate (TSR) in host rock or second fluid	Predominately negative; reduced seawater sulfate (BSR) in second fluid	Predominately positive; narrow range (<10permil); hydrothermal source
Ore Fluid	Low to high temperature (70-300°C) infiltrated or connate, variable evaporated seawater	Mostly low temperature (90-150°C) connate bittern brines or evaporate dissolution brines	Low to moderate temperature (70-280°C) infiltrated partially evaporated seawater	Moderately higher temperatures; reduced fluids
Timing of mineralization	Syngenetic and/or early-mid diagenesis in unlithified to lithified sediment	Epigenetic, generally 10's-100's Mya after host rock deposition	Mostly during diagenesis, in partly and wholly lithified sediments. Minor syngenetic component	Syngenetic, though rather difficult to identify due to the high-grade metamorphism
Associated Igneous Activity	No direct association with igneous activity, but tuffs related to synchronous distal volcanism may be present	Not associated with igneous activity	Close spatial and temporal association with volcanic activity in Limerick province	Indirect association with igneous activity
Tectonic or metamorphic overprint	Weakly to intensely deformed and metamorphosed	No examples recognized	Most deposits have some evidence of post ore thrusting and wrench faulting	Strongly metamorphosed (amphibolite-granulite facies)

3.0 Geological Context

3.1 Geological Setting of the Karrat Group

The Paleoproterozoic Karrat Group is part of the larger Rinkian Fold Belt. The Rinkian Fold Belt is part of the Trans-Hudson orogen, creating a link with the Foxe Fold Belt, Canada (St. Onge et al., 2009) (Figure 3.1). Geochronological results of Sanborn-Barrie et al. (2017) suggest a potential link between the Karrat Group with the Piling Group of central Baffin Island**.**

The Karrat Group was initially characterized by fold nappes with sheath-like geometry and flat-lying axial surfaces that affect both Archean basement gneisses and the Proterozoic cover rocks (Grocott and Pulvertaft, 1990). The Karrat Group was interpreted as an epicontinental marginal basin, which formed in response to northward dipping subduction at a convergent margin in the Nagsugtoqidian belt to the south (Grocott and Pulvertaft, 1990). In this model, the Karrat Group was deposited during a rifting event in three hypothetical sub-basins. This was later revised (Grocott and McCaffrey, 2017) using structural restoration techniques and proposed sedimentary basins controlled by NW-SE trending extensional fault system, depositing the siliciclastic and carbonate sequences of the Upper Karrat Group, which were later filled and overtopped by turbidite systems, controlled by a thrust system that covered from west to east.

A restricted passive margin setting was also proposed to characterize the Karrat Group (Thrane et al., 2005). Sanborn-Barrie et al. (2017) suggested that the Karrat Group evolved over time from a restricted shallow marine, passive margin sequence to a foreland basin succession in response to the Thelon orogen, initiating the sedimentation of the upper siliciclastic unit (Nukavsak Formation). This was followed by recumbent folding, regional metamorphism from the collision of the Rae-North Atlantic cratons, or possibly the Rae craton-Assiat microdomain.

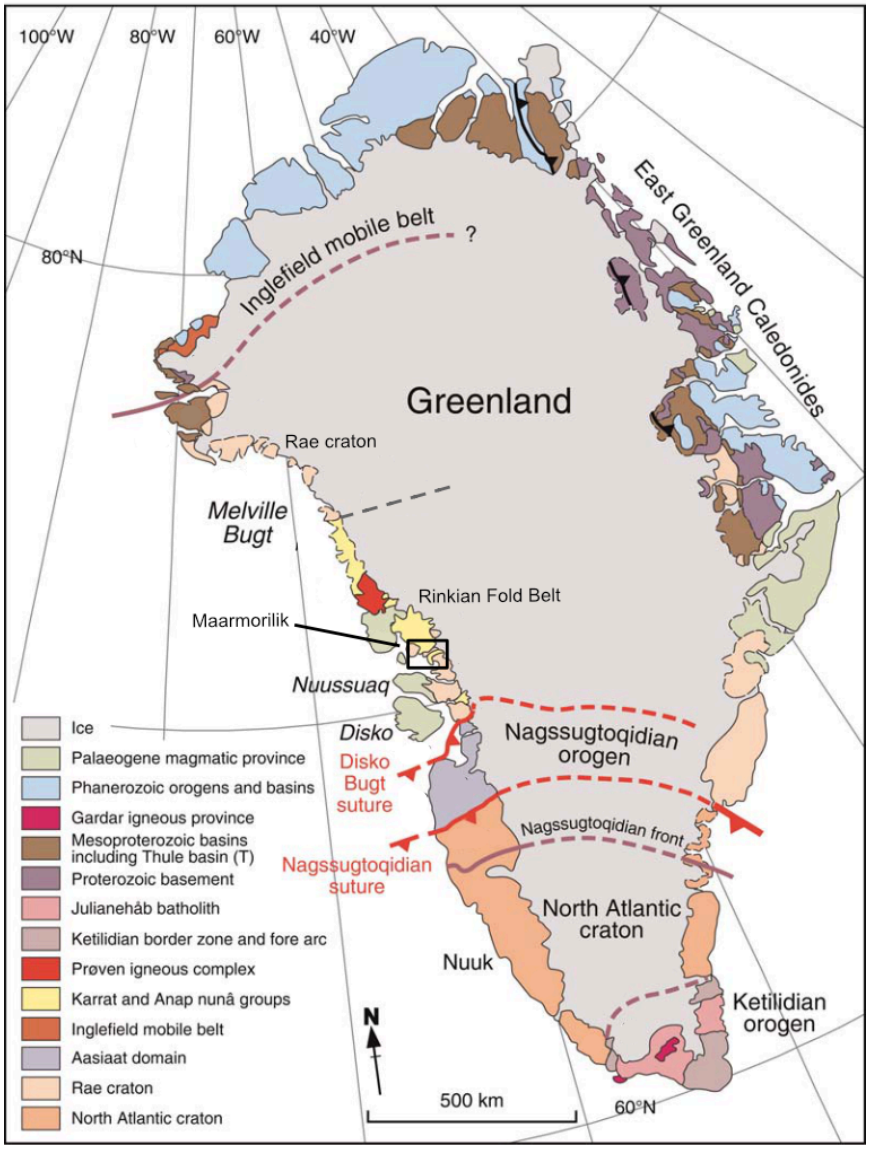

Figure 3.1. Simplified geological map displaying the location of the Rinkian fold belt alongside major tectonostratigraphic assemblages and structures within Greenland (modified from St. Onge et al., 2009).

The Qeqetarssuaq Formation forms the Lower Karrat Group, which lies upon Archean gneisses. The lower Karrat Group experienced amphibolite-facies metamorphism (Thrane et al., 2005), evidence for this includes the presence of hornblende ± diopside assemblages in mafic components of the basement gneiss, and staurolite ± garnet ± siliminanite in pelite of the lower Karrat Group. The Qeqetarssuaq Formation is overlain by the upper formations (the Upper Karrat

Group), and are separated by an angular unconformity (Guarnieri et al., 2016) (Figure 3.2). Units of the Karrat Group and their basement rocks are described below.

3.1.1 Archean basement rocks

The Archean basement on which the Karrat Group is deposited is mostly granodioritic in composition throughout the study area and is mapped as the "Umanak gneiss" (Escher and Pulvertaft, 1995). The Archean basement complex is not well studied overall (Henderson and Pulvertaft, 1967). Unpublished ages from the Umanak gneiss indicate crystallization ages of ~3.0 to 2.7 Ga (Thrane et al., 2003).

3.2.0 Stratigraphy of the Karrat Group

3.2.1 Qeqetarssuaq Formation

The Qeqetarssuaq Formation was formerly described as a ~500m thick unit in contact with the basement, with the lower 300m comprising mainly hornblende schists (Henderson and Pulvertaft, 1987; Grocott and Pulvertaft, 1990). Observations by the Karrat Zinc project team (Rosa et al., 2016) describe the Qeqetarssuaq Formation as a unit dominated by white-green quartzites, garnet schists and semi-pelites, with a minor calcite marble component. The basal component is infolded with Archean basement rocks. The Qeqetarssuaq Formation differs from the other formations in that it is metamorphosed to middle amphibolite facies where the others are not. Additionally, the Qeqetarssuaq Formation is separated from the other formations by an angular unconformity (Rosa et al., 2016; Guarneri et al., 2016).

3.2.2 Marmorilik Formation

The Marmorilik Formation, which hosts the main Pb-Zn mineralization, is dominated by carbonate rocks. It unconformably overlies the basement gneiss with a structural thickness estimated to be up to 1600m (Henderson and Pulvertaft, 1967; Grocott and Pulvertaft, 1990). The formation is interpreted to have been formed in a shallow marine environment (Garde et al*.,* 1978), composed of a basal clastic unit, comprising white to green quartzites that locally host magnetite

(Rosa et al., 2016). This is overlain by dolomitic marbles that give way to calcitic marbles in the upper part of the formation (Garde et al., 1978). A psammite to semi-pelite unit can be found above the calcite marble, which has been interpreted as part of the Nukavsak Formation (Grocott and Pulvertaft, 1990). On-going detrital zircon geochronology at the University of Saskatchewan will help verify this interpretation. The high Pb-Zn mineralization zone is dominantly hosted in the upper calcite marble unit; however, the mineralization can be found in the lower dolomitic marble unit as well in close association with graphitic pelite lenses within these units.

3.2.3 Kangilleq Formation

The Kangilleq Formation is a succession of mafic meta-volcanic rocks attributed to extrusive submarine volcanism that show primary volcanic features such as tuff beds, vesicles, flows, and pillows (Rosa et al., 2016). Previously, meta-volcanic rocks (now known as the Kangilleq Formation) were thought to be part of the Qeqetarssuaq Formation (Kalsbeek et al., 1998; Henderson and Pulvertaft, 1967). Further study revealed differences in metamorphic grade and stratigraphic relationships between the two formations that classified the Kangilleq Formation as its own formation.

3.2.4 Qaarsukassak Formation

The Qaarsukassak Formation was previously suggested to represent a structurally displaced basal component to the Marmorilik Formation (Coppard et al., 1992) given the carbonate lithology and Pb-Zn mineralization similarities. Coppard et al. (1992) describes the Qaarsukassak Formation as a 30 to 66m thick quartzite-metacarbonate succession with a mineralized zone appearing in calcite bearing dolomitic marbles, confined by the basement and Nukavasak Formation. Sulfides included in the mineralized zone are pyrite, pyrrhotite, galena, sphalerite, and sulfosalts. The Qaarsukassak Formation consists of massive to laminated and calcite-cemented quartzites overlain by graphitic quartzites and metamudstones (Guarnieri et al., 2016). This is covered by calcite marble and a thin layer hosting Pb-Zn mineralization. Asymmetrical ripple marks in in fine-grained metasandstone was documented in the lower Qaarsukassak Formation, suggests a fluvial to marginal marine setting for the Qaarsukassak Formation (Rosa et al., 2017).

The thickness estimates from Coppard et al. (1992) represent the structural thickness, whereas the stratigraphic thickness is ~20m (Guarnieri et al., 2016). Variable thickness of the formation along strike suggests that the Qaarsukassak Formation deposition infilled basement paleo-topography (Guarnieri et al., 2016). Observations in the field show that the Qaarsukassak Formation pinches out in the north and south end of the Discovery area (Figure 6.3). It is unclear whether the pinch-outs are sedimentary/erosional or structurally-controlled.

3.2.5 Nukavsak Formation

The Nukavsak Formation is the most widespread of the five formations of the Karrat Group, spanning from Maarmorilik to Pangnertoq (~72ºN) (Figure 1.1) or possibly as far north as Red Head (Henderson and Pulvertaft, 1967). The formation is interpreted as a turbidite flysch sequence, comprised of greywacke, sandstone, and shale with a minimum structural thickness of 5000m (Grocott and Pulvertaft, 1990; Henderson and Pulvertaft, 1967). Recent fieldwork results describe the Nukavsak Formation as fine- to medium-grained calcite-cemented metasandstones and minor metamudstones with dispersed clasts dominantly of metavolcanic origin (Rosa *et a*l., 2016).

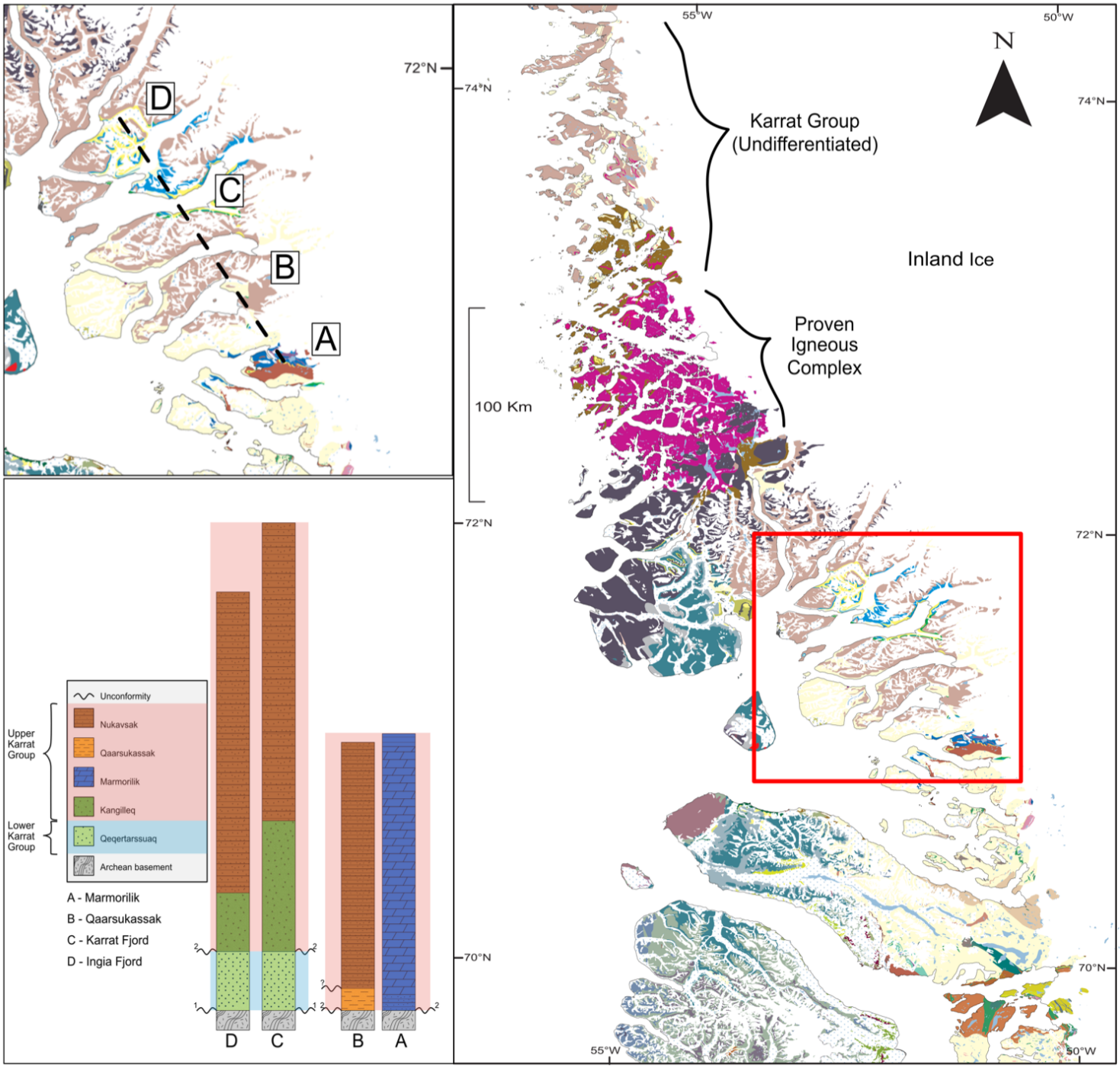

Figure 3.2. Simplified regional geological map of the Karrat Group project area (annotated red square), highlighting the main Karrat Group from Maarmorilik to Ingia Fjord with schematic stratigraphic columns displaying the lateral variation in the stratigraphy, trending northwest (Modified from Rosa *et al*., 2017).

3.3.0 Structural Geology

3.3.1 Regional

Grocott and Pulvertaft (1990) described six stages in the structural and metamorphic development in the Maarmorilik-Pangnertoq domain (Karrat Basin). Based on new structural observations in the field, Rosa et al. (2017) simplified and subdivided the Karrat Basin into four structural domains. The four main deformation stages are: the Qeqetarssuaq Stage (D1), deformation that is observed only in the Qeqetarssuaq Formation and the Umanak Gneiss that predate the unconformity. The other three deformation events, post-dating the unconformity, are the (D2) extensional tectonics and related fold structures, the Kigarsima Stage (D3) featuring SW-NE compression, and the Maarmorilik Stage (D4) featuring NW-SE compression, which followed with extensions around intrusions and distal E-W compression.

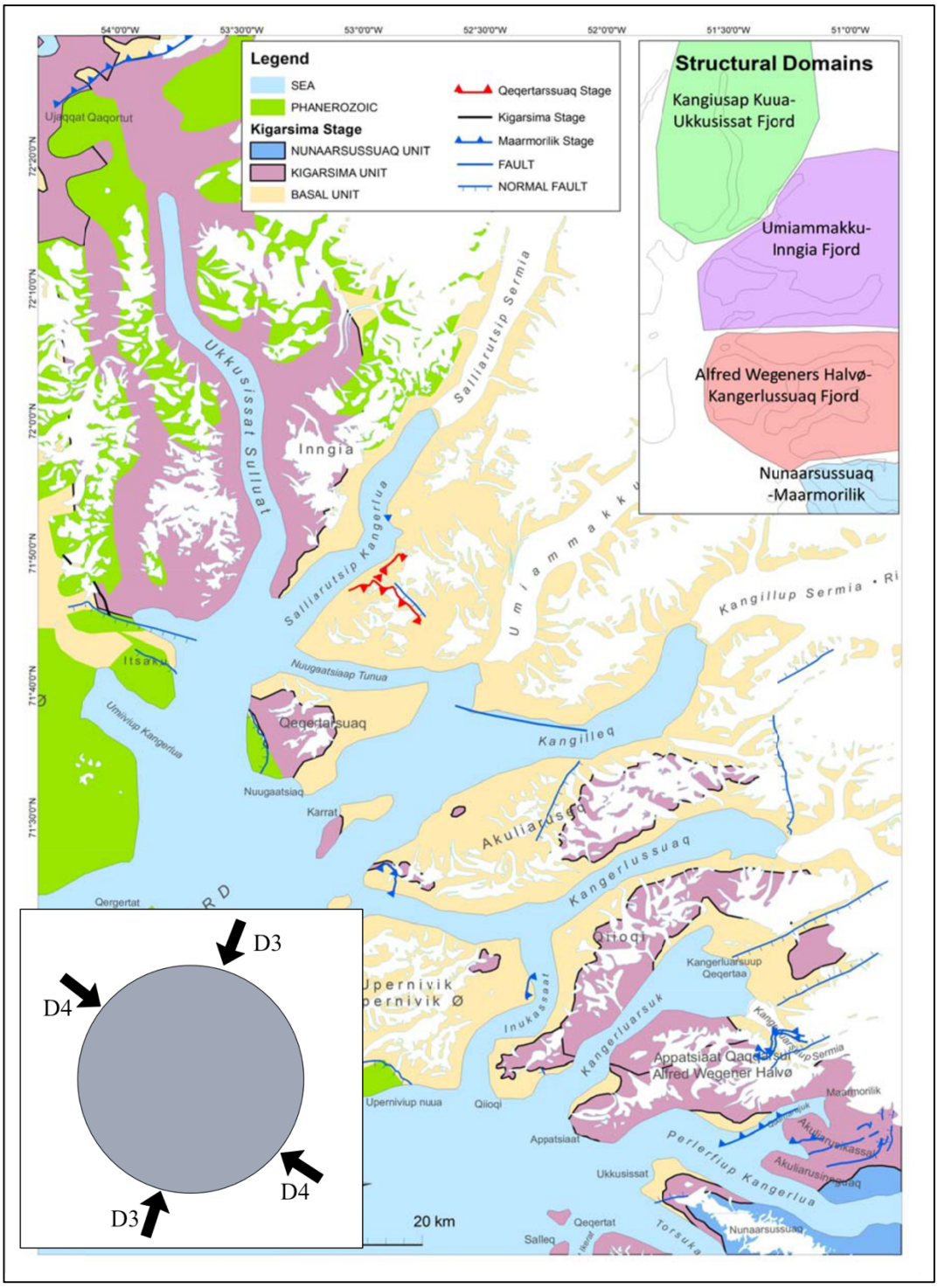

Fig 3.3. Simplified structural map of the Karrat Fjord region (upper right) Additional map to show the structural domains (lower left). Illustration to visualize regional D_3 and D_4 compression stages using an equal area stereonet (modified from Rosa et al., 2016).

3.3.2 Identified Local Structures in Ore Zones

The massive, sub-horizontal Pb-Zn ore in the Black Angel deposit is structurally controlled with ore body structural thicknesses varying between 0.5m to 35m and original thicknesses estimated to be between 0.5m to 8m (Pedersen, 1980). Pedersen (1981) discovered three phases of deformation (Figure 3.4) in the Black Angel mine: D1) recumbent, isoclinal folding, deforming original layered ore. Consequently, mobile elements are then relocated to lower stress areas such as hinge zones, extension fractures and necked zones within the sulfide sheets; D2) low angle thrusts displacing upper parts of the ore zones. Thrust planes are confined to sulfide sheets, producing massive to porphryoclastic ore tectonites, as seen with durchbewegung textures. Milled out fragments of pyrite ore and rounded marble inclusions (originated from carbonate layers in the sulfide sheets) are the indicators of this intense shearing; D3) This open- to tight folding is more noticeable in the northern sections of the mine. This resulted in a widespread differential mobilization of mobile elements in the ore body, producing a coarse grained, mobilized ore tectonite. Areas of high strain and increasing the pore fluid pressure lead to hydraulic fracturing during the later stages of mobilization, resulting in the formation of breccias, joints, and extension fractures (Pedersen, 1980). It should be noted that the D1-D3 events reported by Pederson (1980) do not match the revised regional deformation events of Rosa et al. (2017), since their D1 is not represented at Marmorilik.

Microstructural analysis on the ore zones suggests that the deformation took place at temperatures close to the metamorphic peak, roughly 450-500°C and at estimated pressures of 1-1.5 kb (Pedersen, 1981).

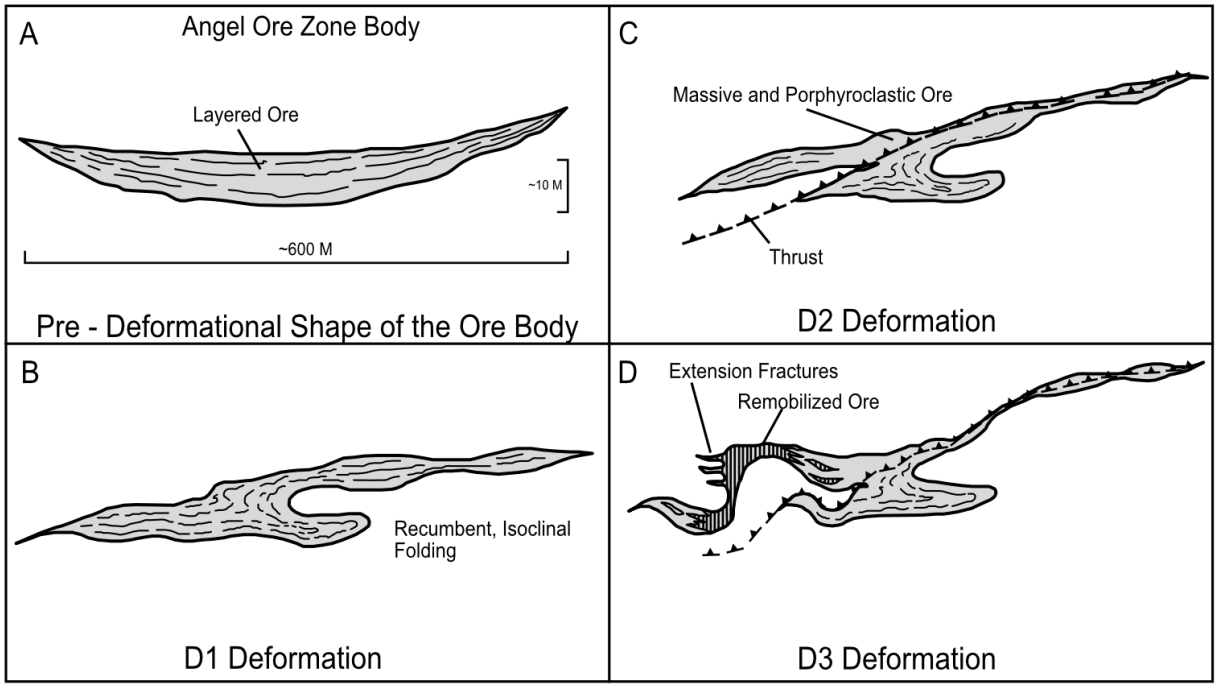

Figure 3.4 Schematic diagram of Angel ore zone body undergoing multiple stages of deformation as described and illustrated in Pedersen, (1981).

3.4 Economic geology: Black Angel Deposit and Qaarsukassak Formation mineralization

Exploration in the Karrat area for Pb-Zn mineralization has been ongoing for decades with the first large discovery in the 1930s. This discovery was due to anomalous sulfide samples in connection with a marble quarry (Thomassen, 2003). The Pb-Zn discovery near Maarmorilik led to production of the Black Angel Mine in 1973 (Coppard et al., 1992). The mine's lifespan lasted for almost 20 years, ending production in 1990. Black Angel deposit is comprised of ten ore bodies, totaling 13.6 M tons with ore grades of 12.3%, 4.0% and 29ppm in Pb, Zn, and Ag, respectively (Thomassen, 2003). During production, a total of 11.2 Mt was mine from the main ore bodies (Thomassen, 1991).

After the mine closure, exploration for other large Pb-Zn localities was conducted throughout the Karrat area with interest near the Black Angel deposit. A discovery was made in the Kangerluarsuk Fjord (Figure 1.1), roughly 40km north of Black Angel by RTZ Mining (Coppard et al, 1992). This Pb-Zn mineralization was hosted in a carbonate-shale rock, between the Archean basement and the Nukavsak Formation and informally called "the Discovery

Formation," now the Qaarsukassak Formation (Guarneri et al., 2016). The Qaarsukassak Formation contains mineralization crops out along the exposed strike with ore grades of 41 wt% and 9.3 wt% of Zn and Pb, respectively (Coppard et al., 1992).

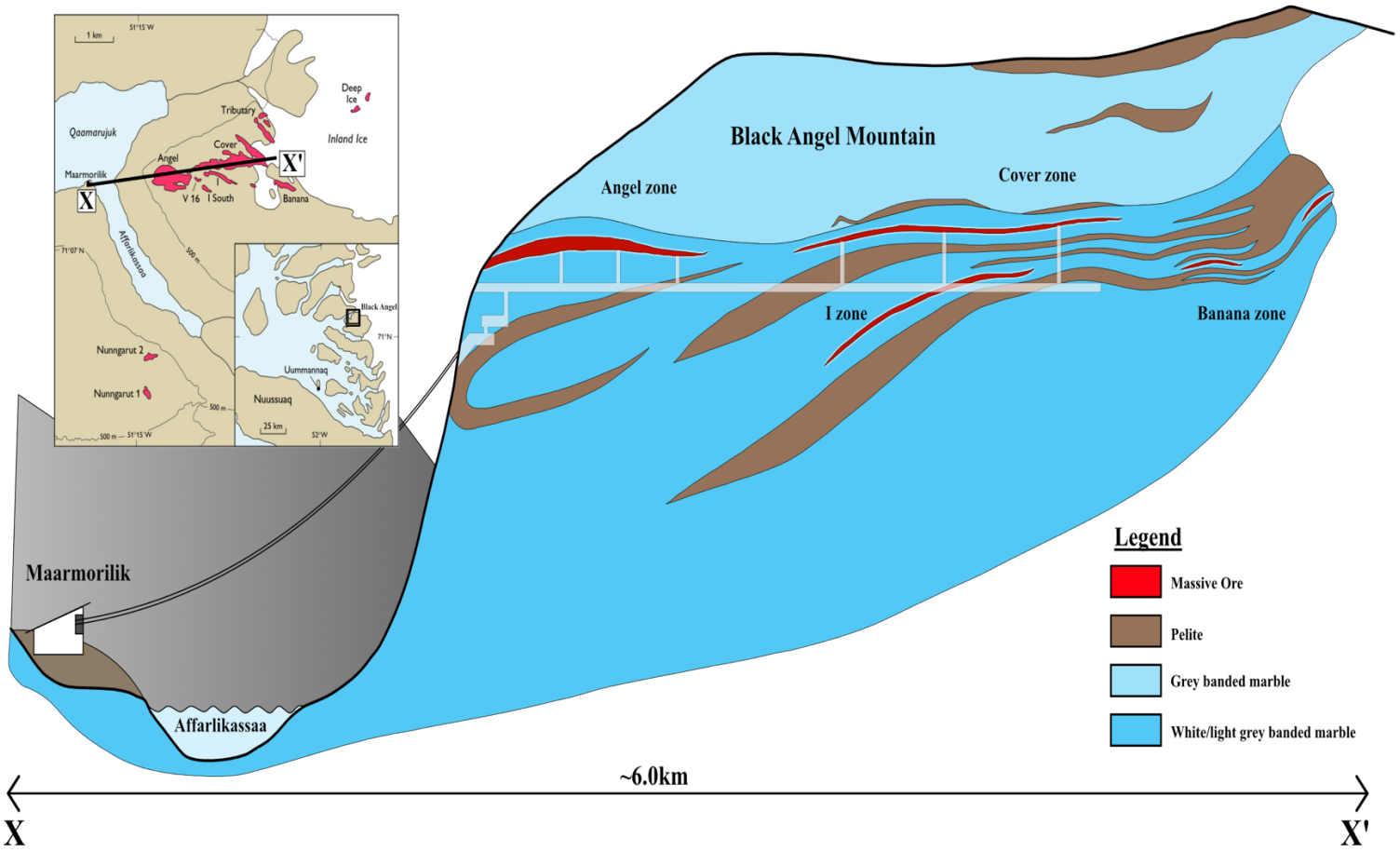

Figure 3.5 A schematic plan and cross-section view of the Black Angel mine, highlighting the main ore bodies identified within the deposit as well as the satellite ore bodies, Nunngarut zone 1 and 2, south of the main deposit. (Modified from Thomassen, 1991,2003)

3.5 Age Constraints of the Karrat Group

The absolute age of the Karrat Group is poorly constrained, though it has been established as Paleoproterozoic (Kalsbeek et al., 1998; Sanborn-Barrie et al., 2017). A Wheeler diagram (Figure 3.6) illustrates the variation of the Karrat Group spatially and in time. Although geochronological studies are ongoing as part of the Karrat Zinc project, available ages were compiled from the literature to understand probable stages in which the Pb-Zn mineralisation was emplaced.

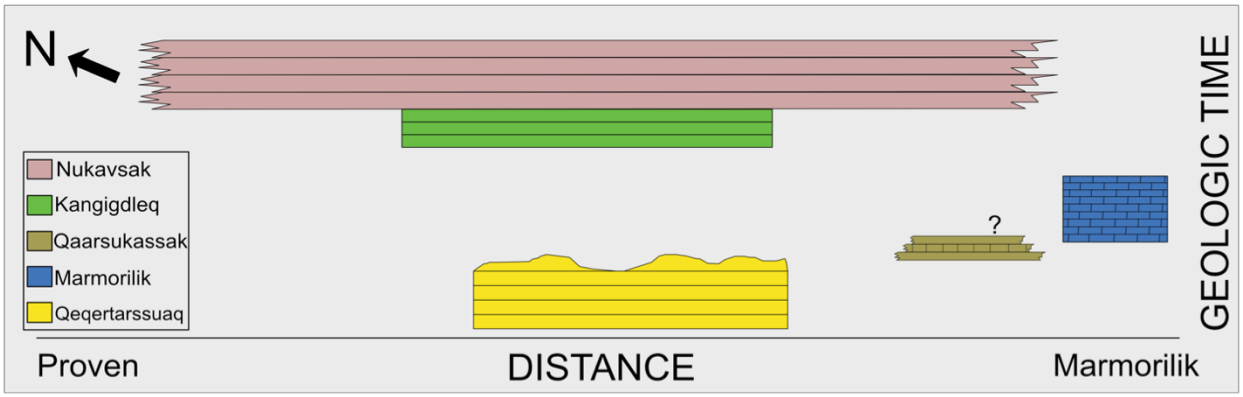

Figure 3.6. A time-stratigraphy diagram displaying spatial and temporal relationships between the five formations within the Karrat Group (modified from Rosa et al., 2016).

The basement has been locally dated at ~3.10-2.98 Ga and ~2.70 Ga using zircon U-Pb analysis (Thrane et al., 2003; Connely et al., 2006, respectively); this confirms an earlier age of 2840 Ma by whole-rock Rb-Sr (Kalsbeek et al., 1981). The youngest detrital zircon U-Pb age in the Qeqertarssuaq Formation is 2029 ±18 Ma (Sanborn Barrie et al., 2017). An age for the metavolcanic Kangilleq Formation has yet to be determined, however, it is conformable with the younger Nukavsak Formation (Rosa et al., 2016), which has youngest detrital zircon U-Pb age ranges of 1.98 to 1.89 Ga (Sanborn Barrie et al., 2017; Kalsbeek et al., 1998). The Prøven Igneous Complex is interpreted to crosscut both the Archean basement and the Nukavsak Formation with a U-Pb age range of ~1900 to 1870 Ma (Sanborn Barrie et al., 2017; Thrane et al., 2005). The D1 deformation stage has only a relative age constraint, existing prior to the deposition of the Upper Karrat Group, subsequently defining an unconformity between the Lower and Upper Karrat groups

(Guarneri et al., 2016). The stages of D2 to D4 have not been dated directly, however metamorphic overprinting on zircon has been dated at ~1840 to 1829 Ma as well as a U-Pb metamorphic age of 1768 ± 8 Ma on titanite (Sanborn-Barrie et al., 2017; Kirkland et al., 2017, respectively). Additionally, an interpreted metamorphic age using Pb-Pb on Marmorilik marble is dated at 1881 ± 20 Ma, though this is inconsistent with recent U-Pb metamorphic zircon rim ages (~1840 Ma).

Prospective Pb-Zn mineralization is found in both the Marmorilik and Qaarsukassak formations. Using the aforementioned age constraints, a diagram can be generated to show the possible age range in which the mineralization could be emplaced (Figure 3.7). The relative age constraint for the Pb-Zn mineralization is between the depositional age of Marmorilik and Qaarsukassak formations and the latest stage of deformation (D4). This is problematic when trying to identify a deposit model for the Pb-Zn mineralization as this age constraint can suggest both a syngenetic and epigenetic style of mineralization. Therefore, dating the mineralization itself appears necessary to determine a more precise age constraint.

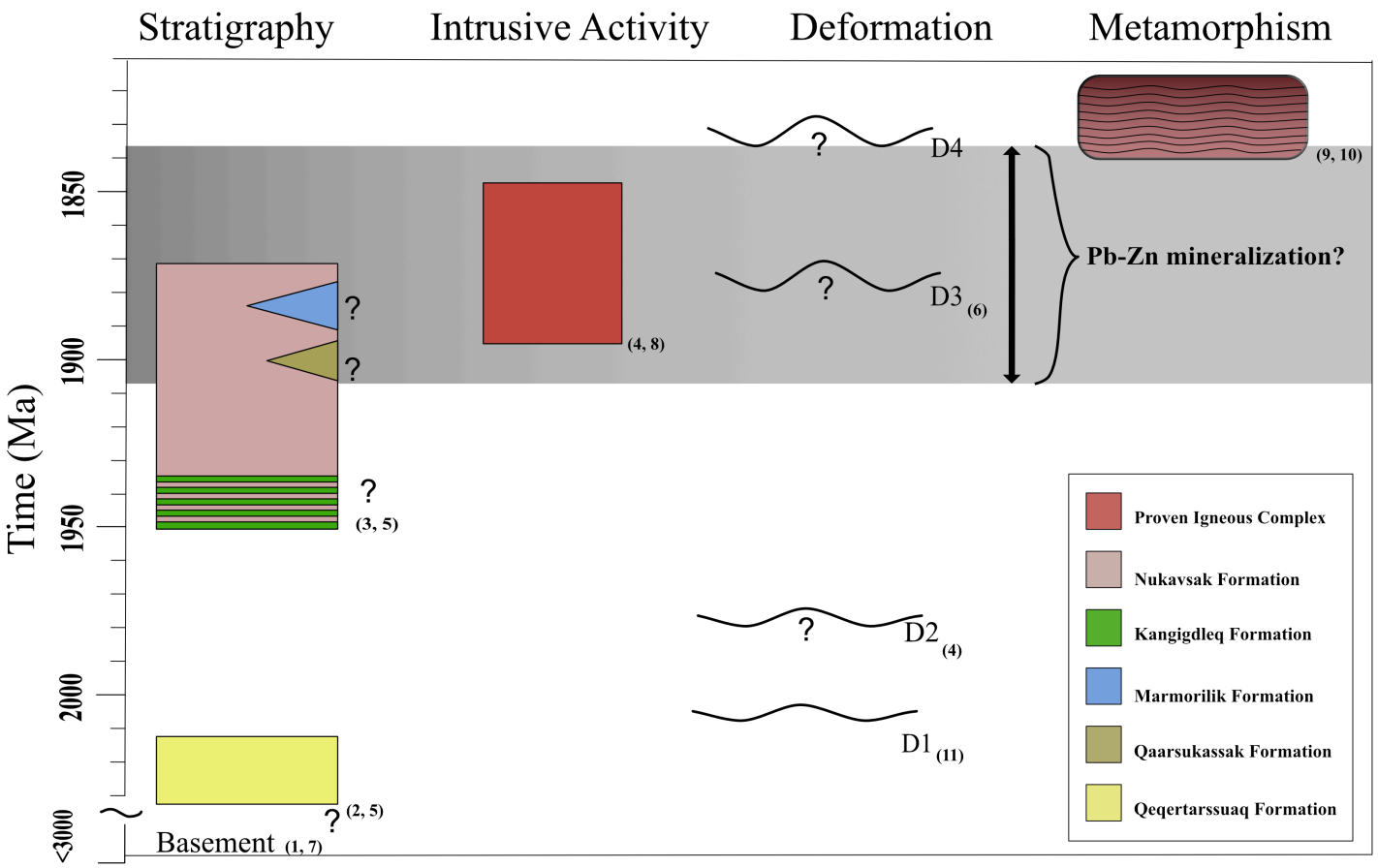

Figure 3.7 Diagram showing a possible time-frame for the Pb-Zn mineralization to occur. Accompanied are the relative and known absolute age constraints within the Karrat Group. References: (1) Connelly et al., 2006 (2) Kalsbeek, F., 1995 (3) Rosa et al., 2016 (4) Sanborn-Barrie et al., 2017 (5) Sanborn-Barrie et al., 2017 (6) Taylor and Kalsbeek, 1990 (7) Thrane et al., 2003 (8) Thrane et al., 2005 (9) Thrane et al., 2005 (10) Van Gool et al., 2002 (11) Guarneri et al., 2016

4.0 Isotopic Systems Applied to Pb-Zn Mineral Deposits

4.1 Sulfur Isotopes

There are four naturally occurring stable isotopes of S: ^{32}S, ^{33}S, ^{34}S, and ^{35}S, with approximate abundances of 95.02%, 0.75%, 4.21%, and 0.02%, respectively (Thode et al., 1953). In sulfide minerals, the most commonly studied sulfur isotope ratio is the two major abundant isotopes: $^{34}S/^{32}S$. There are many significant isotopic variations in $\delta^{34}S$ caused by progressive fractionation which can result from equilibrium or kinetically controlled and physical processes (Seal, 2006). Significant variation also results when the range of values of $\delta^{34}S$ between the initial and final sulfur species is large (Seal, 2006). This process is known as Rayleigh fractionation.

As fractionation processes with sulfur can create small variations within the $^{34}S/^{32}S$ ratios, isotope composition of sulfur is expressed in delta (δ) notation, as parts per thousand variation relative to a standard reference material (Seal, 2006). This is relative to that of a standard (troilite from Canyon Diablo meteorite, which has a $^{34}S/^{32}S$=0.0450045) and is expressed by the equation:

$$\left[\left(\frac{^{34}S}{^{32}S}_{sample} \Big/ \frac{^{34}S}{^{32}S}_{standard}\right) - 1\right] \times 1000 \quad \text{.....(4.1)}$$

4.1.1 Sulfur model

Sulfur in massive sulfide deposits can derive from a variety of sources either by 1) reduction of seawater sulfate by bacterial action or by abiotic means, 2) by mobilization of sulfur contained within igneous material (around 0 ‰), 3) evaporitic sediments (values equal or higher than the coeval seawater sulfate), 4) or a combination of these processes. In addition to the source composition and the process of incorporation, sulfur fractionation is also affected by 1) equilibrium fractionation involving the partitioning of the minor isotope relative to the major as a function primarily of temperature, fS_2, fO_2, pH, salt concentration of fluids (Ohmoto and Rye, 1979), and 2) kinetic fractionation, which is the result of the relatively faster rate of reaction on the lighter

isotope and achieved either by sulfate-reducing bacteria or by inorganic reactions with ferrous minerals or organic-carbon compounds at elevated temperature (Ohmoto and Rye 1979).

4.1.2 Application to the SEDEX Models

SEDEX sulfur isotope values compiled by Leach et al. (2005) show a $\delta^{34}S$ mean value ~15‰ less than the coeval seawater sulfate value throughout geologic time. This parallel relationship suggests that the ultimate source of contributing sulfur would be from marine sulfate either as seawater, pore water, or pre-existing sulfate minerals such as barite. The reduction of sulfate to sulfide would be from the involvement of biogenic sulfate reduction (BSR), thermochemical sulfate reduction (TSR), or both, depending on the temperature and availability of the reductant. Most SEDEX deposits coincide with times when Earth's oceans had an anoxic and H_2S-rich water column (Leach et al., 2010). It is then reasonable to suggest that the sulfur source is predominately from seawater sulfate and sulfide precipitation occurs in these reduced water columns. Wilkinson (2014) shows evidence for a seawater origin with a parallel evolution of the isotopic compositions of ore sulfides and the secular seawater sulfate and sedimentary pyrite curves (Figure 4.1) in the Phanerozoic Era. The Proterozoic marine sulfur isotope record is less well constrained and overlaps values indicating sulfide production by either BSR or TSR, making it difficult to identify the mechanisms. However, the Sullivan and HYC deposit display negative values well below the average sedimentary pyrite curve and thus can suggest that a significant component of the sulfide was from BSR (Wilkinson, 2014).

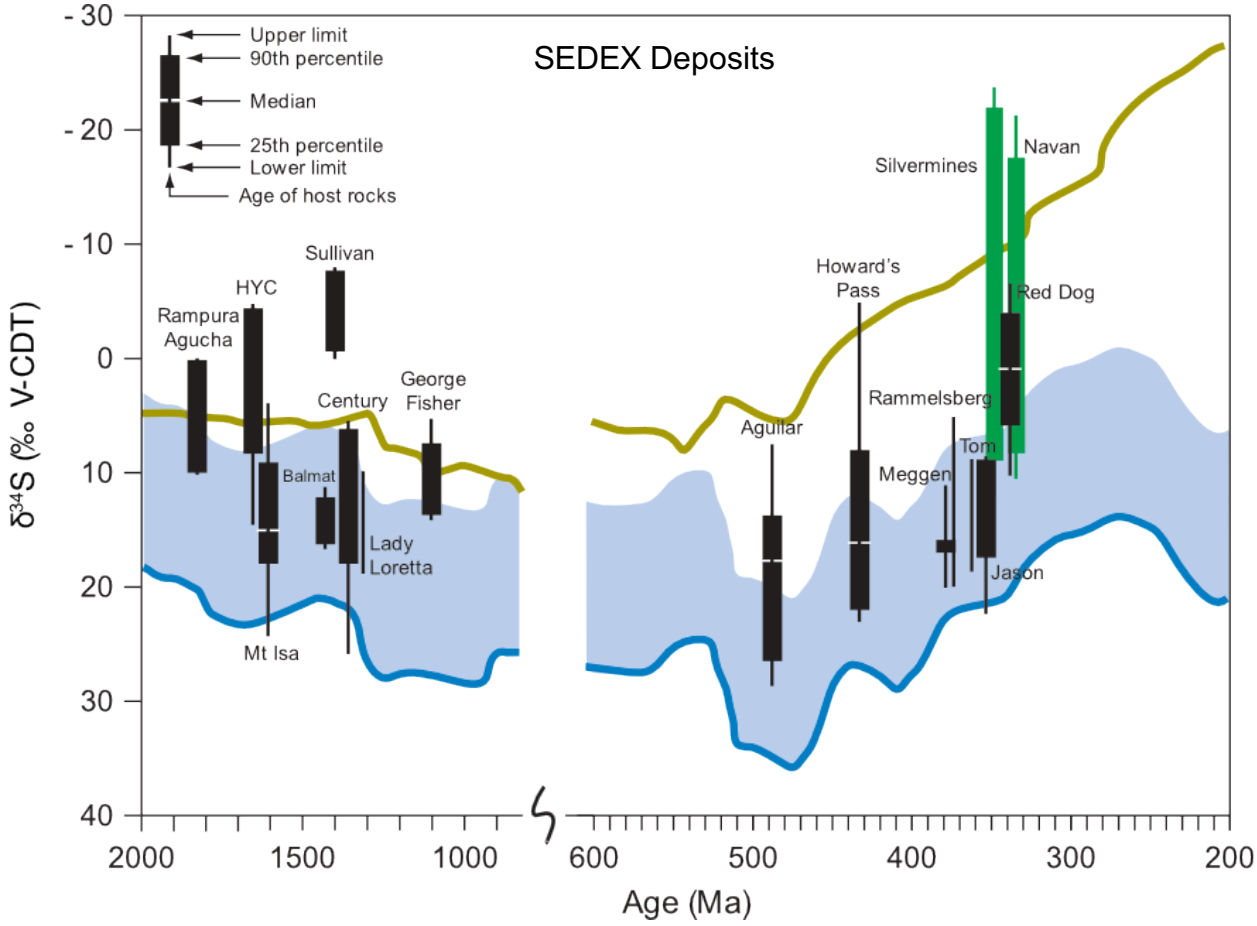

Figure 4.1 Box and whisker diagram of various SEDEX deposits showing the range and median $\delta^{34}S$ values of assorted sulfides (pyrite, sphalerite, galena, chalcopyrite, etc.). Deposits plotted at their approximate host rock age. Sulfide sulfur values compared with the coeval seawater (blue line) and mean sedimentary pyrite composition (brown line) as produced by BSR. Blue shaded field indicates the likely range of sulfide compositions produced via TSR of seawater derived sulfate (Kiyosu and Krouse, 1990). For comparison, Irish-type deposits are displayed, highlighted in green (Wilkinson, 2014).

4.1.3 Application to the MVT Models

Sulfur isotope values collected from MVT deposits show a heavier $\delta^{34}S$ signature, which is consistent with sulfur being derived from a variety of crustal sources (Ohmoto and Rye, 1979; Sangster, 1990). These sources can include sulfate-bearing evaporites, connate seawater, and diagenetic sulfides (Leach and Sangster, 1993). Sangster (1990) also noted that the ultimate source

of sulfur is likely seawater sulfate contained by the sediments in various minerals and/or connate water that was subsequently reduced by one or more processes. Wilkinson (2014) plots sulfide compositions from various deposits (Figure 4.2) with the inferred deposit age, host-rock age, and secular seawater sulfate curve. Figure 4.2 displays MVT deposits with a relatively narrow range of values closer to the coeval seawater sulfate value, suggesting that the sulfides are derived from seawater sulfate dominantly through TSR processes, either directly from brines or from dissolved evaporites that were incorporated in the sedimentary basin at some point between the host rock deposition and mineralization.

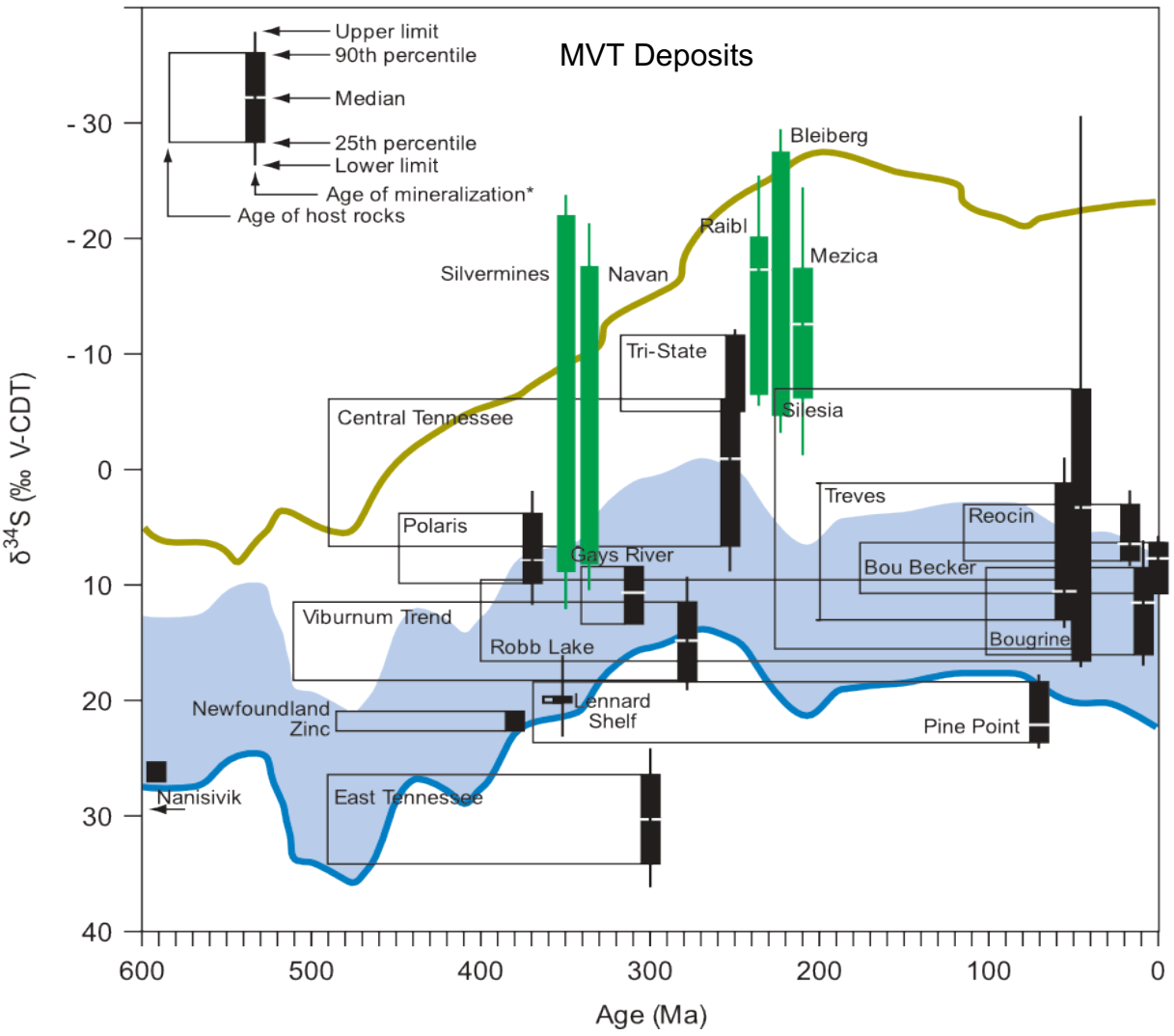

Figure 4.2 Box and whisker diagram of various MVT deposits showing the range and median $\delta^{34}S$ values of assorted sulfides (pyrite, sphalerite, galena, chalcopyrite, etc.). Deposits plotted at their approximate host rock age. Sulfide sulfur values compared with the coeval seawater (blue line) and mean sedimentary pyrite composition (brown line) as produced by BSR. Blue shaded field indicates the likely range of sulfide compositions produced via TSR of seawater derived sulfate (Kiyosu and Krouse, 1990). For comparison, Irish-type deposits are displayed, highlighted in green (Wilkinson, 2014).

4.2 Pb-Pb Isotopes

There are four naturally occurring Pb isotopes: ^{204}Pb, ^{206}Pb, ^{207}Pb, and ^{208}Pb. Of these isotopes, only ^{204}Pb is non-radiogenic, as the latter three isotopes are the product of radioactive decay of ^{238}U, ^{235}U, and ^{232}Th, respectively (Dickin, 2005). Since the Earth formed, the abundances of the three radiogenic isotopes have increased as a result of radioactive decay through time. ^{204}Pb, being non-radiogenic, is often used as a reference isotope.

Model ages can be extracted from galena in sedimentary-hosted deposits which can aid in understanding the genetic time-frame which the Pb-Zn mineralization was precipitated. An early approach to this was the Holmes and Houtermans (1946) model, which measured the age of the Pb source since the formation of the Earth until the crystallization of galena (assuming a closed, single stage Pb system). This method is exemplified in the equation:

$$\left(\frac{^{206}Pb}{^{204}Pb}\right)_t = \left(\frac{^{206}Pb}{^{204}Pb}\right)_T + \frac{^{238}U}{^{204}Pb}\left(e^{\lambda 238T} - e^{\lambda 238t}\right) \quad \text{.....(4.2)}$$

The Stacey-Kramers two stage model (Stacy and Kramers, 1975) for the evolution of crustal Pb is commonly used to date Pb-bearing minerals because it considers observed discrepancies between single stage Pb dates derived from many ore deposits and their ages determined by other dating methods. The model breaks up the evolution of Pb into two stages; an early stage between 4.57 and 3.70 Ga years ago, where a primordial isotope ratio for ^{238}U/^{204}Pb of 7.192 is used, and a more recent stage, where ^{238}U/^{204}Pb ratio of the reservoir was changed by geochemical differentiation to 9.735 and remained constant to present (Faure, 1986). Pb which evolved in such a reservoir and was incorporated into Pb-minerals at some time in the past, must have Pb isotope ratios that lie on the growth curve between 3.7 Ga to the present day. The time of separation from the reservoir can then be calculated from the equation of the isochron:

$$\frac{^{207}Pb/_{^{204}Pb} - 12.998}{^{206}Pb/_{^{204}Pb} - 11.152} = \frac{1}{137.88}\left(\frac{e^{\lambda_2 T} - e^{\lambda_2 t}}{e^{\lambda_1 T} - e^{\lambda_2 t}}\right) \quad \text{.....(4.3)}$$

where 12.998 is the $^{207}Pb/^{204}Pb$ ratio at the start of stage 2, 11.152 is the $^{206}Pb/^{204}Pb$ ratio at the start of stage 2, 1/137.88 is the modern $^{235}U/^{238}U$ ratio, λ_1 is the half-life of ^{238}U, λ_2 is the half-life of ^{235}U, T=3.70 x 10^9 yrs, and t = the age of the mineral (Faure, 1986).

Application of Pb isotopes to mineral exploration relies on interpretations based on very small differences in the relative abundances of the four isotopes of Pb. Pb isotopes have been used for mineral exploration to help find potential targets that are nearby to known economical deposits. An idea that was introduced by Delevaux et al. (1967), suggested that mineral prospects with similar Pb isotopic composition as a producing deposit in a district may be economical in itself. The main hypothesis is that all comparable deposits in a district were derived from the same mineralizing fluids (Gulson and Porritt, 1987). This hypothesis will be applied to the samples analyzed in this study to confirm if the two Pb-Zn bearing formations are co-genetic with respect to their mineralization.

4.2.1 Application to SEDEX Models

Pb isotope data provides a general constraint on the source of metals for SEDEX deposits. An important observation is the degree of intradeposit homogeneity, suggesting one significant source of Pb was transported into the deposit or Pb that is already homogenized by the hydrothermal system feeding the deposit (Wilkinson, 2014).

4.2.2 Application to MVT Models

One notable observation in MVT deposits is the enrichment of radiogenic Pb in galena, compared to SEDEX deposits. This is not always the case in some deposits categorized as MVT deposits, such as Pine Point (Heyl et al., 1974), which has similar Pb isotope signatures to that of a SEDEX deposit. Another important observation is the heterogeneity of Pb isotope composition in many MVT deposits, contrary to that observed in SEDEX deposits. Differing Pb isotope signatures within a basin suggests mixing of different sources, or possibly multiple inputs of metal sources (Wilkinson, 2014).

4.2.3 Pb sources within the Karrat Group

Published Pb-Pb data from the Nagsugtoqidian-Rinkian Orogen (Connelly and Thrane, 2005) provide a framework of Pb-Pb compositions for both Archean and Proterozoic plutonic rocks, either of which could be potential metal sources (Figure 4.3). The Pb-Pb isotopic mean (n=33) for the Marmorilik mineralization is reported in Sangster et al. (2000), but raw data points are not published.

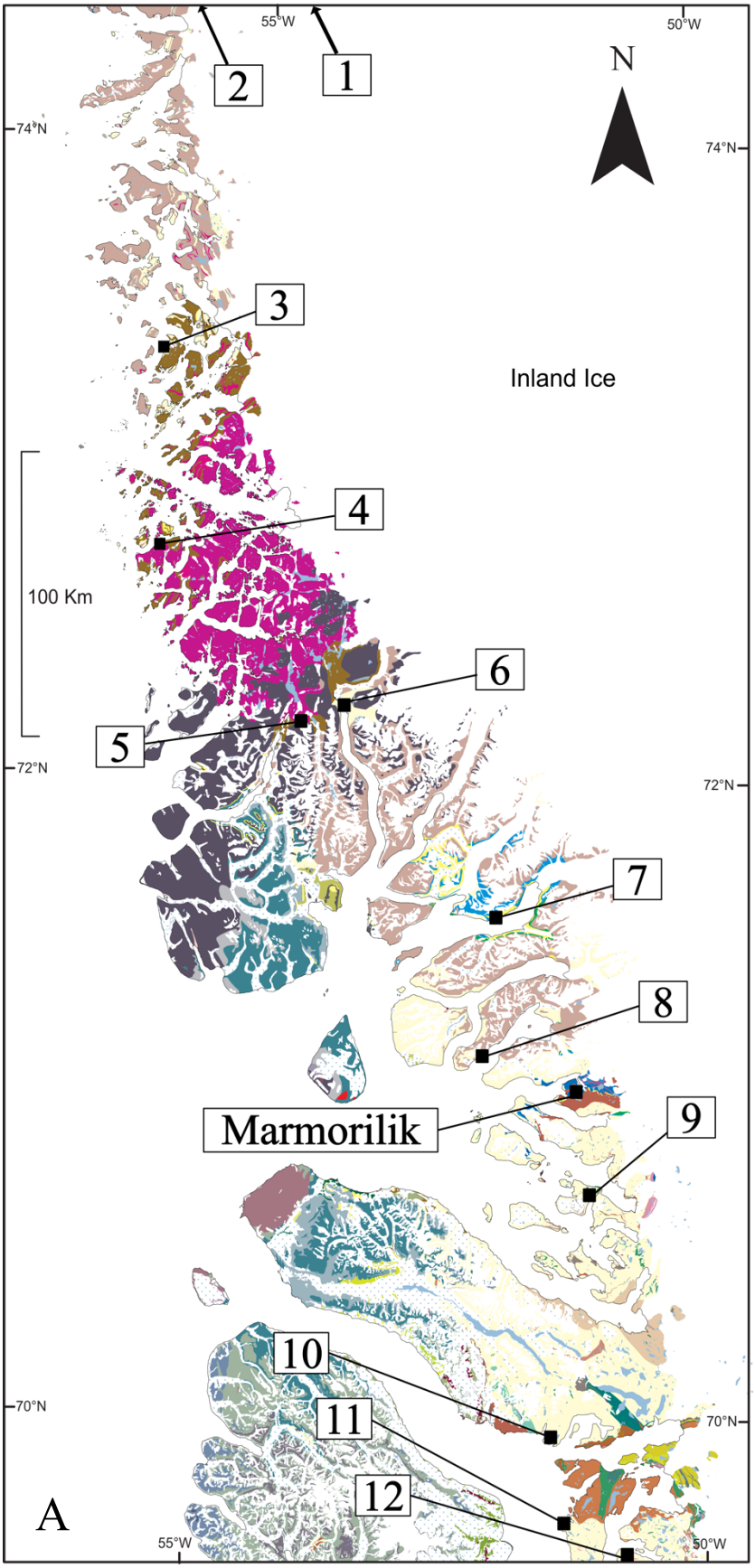
55°W
50°W
N
74°N
74°N
2
1
3
Inland Ice
4
100 Km
6
5
72°N
72°N
7
8
Marmorilik
9
10
11
12
70°N
70°N
A
55°W
50°W

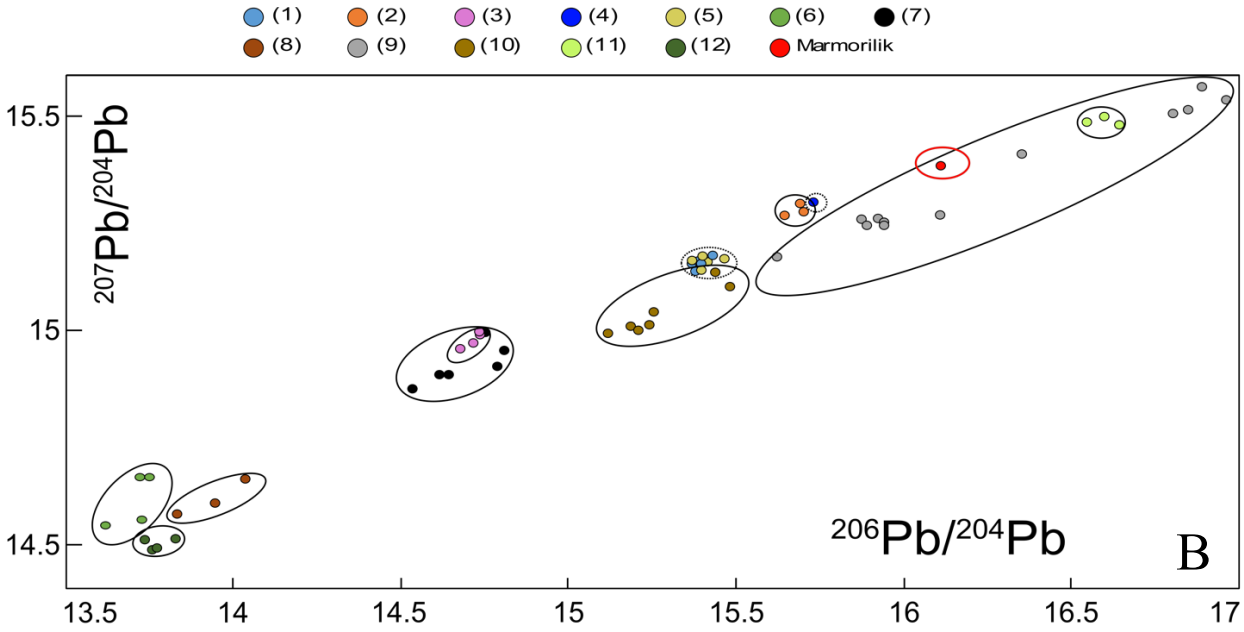

Figure 4.3 A) Accompanied simplified map of the Rinkian Domain, highlighting Pb-Pb sample locations from Thrane and Connelly (2005). B) Pb-Pb data set of the northern data Rinkian Domain. Numbers next to the data points identifies the sample number. Annotated with a red circle is the historical Pb-Pb average of galena from the Marmorilik Formation (Sangster et al., 2000).

4.3 Radiogenic dating using Re-Os geochronology

Rhenium (Re) has two natural occurring isotopes, ^{185}Re and ^{187}Re with abundances of 37.4% and 62.6%, respectively. Osmium (Os) has seven naturally occurring isotopes, two of which (^{187}Os and ^{186}Os) are the decay products of long lived radiogenic isotopes, ^{187}Re and ^{190}Pt, respectively (Dicken, 2005). Of these two decay schemes, Re-Os is used as a geochemical tracer for geochronology. Rhenium 187 radioactively decays to Osmium 187 by beta emission expressed as:

$$^{187}Re \rightarrow {}^{187}Os + \beta^{-} + \nu + Q$$

where β^{-} = negatively charged Beta particle

ν = antineutrino

Q = total decay energy

The Re-Os isochron equation can be viewed as:

$$\left({}^{187}Os/_{188}Os\right)_t = \left({}^{187}Os/_{188}Os\right)_i + \frac{^{187}Re}{^{188}Os}\left(e^{\lambda t} - 1\right) \quad \text{.....(4.4)}$$

Defining the absolute timing of ore deposit formation is important for developing mineral deposit models and mineral exploration programs. Re-Os geochronology has direct application to the timing and duration of hydrothermal ore deposit formation. Most dating methods (Rb-Sr, Sm-Nd, and U-Th-Pb) involve lithophile elements (with exception of Pb) that are not present in sulfide minerals, but Re and Os chalcophile ("sulfur-loving") tendencies are thus relatively stable in sulfide minerals (Dicken, 2005). Re-Os has been successfully employed with molybdenite (Thorne et al., 2013; Li et al., 2016; Kirk et al., 2002), as well as other sulfides such as pyrite, arsenopyrite, and chalcopyrite (Morelli et al., 2004, 2010; Zhimin et al., 2013). This study involves Re-Os geochronology on pyrite associated with ore mineralization. While pyrite has been successful in dating sulfide deposits, there can be drawbacks involved in using this mineral. Some studies (Brenean et al., 2000; Stein et al., 2001) suggest that, in regions unaffected by extensive metamorphic or secondary hydrothermal activity, pyrite can yield reliable ages. Brenan et al. (2000) explains that pyrite can resist diffusion up to 500 °C. However, Mathur et al. (1999) indicated that pyrite may be disturbed by metamorphism and/or metasomatism. This method can also be an issue if overprinting of the fluids occurs as that can disturb the pyrite (or precipitate new pyrite) and record younger ages. This can also be from a result of renewed tectonic activity (Stein et al., 2000).

Re-Os geochronology is an excellent tool for this study as it can help determine the absolute age of the mineralization. As mentioned in chapter 2, there is a differentiation between SEDEX and MVT models based on their mineralization with respect to the host rock age. SEDEX deposit mineralization age is typically similar to the host rock, thus the mineralization is syngenetic/ syn-diagenetic. MVT deposits are epigenetic in nature with mineralization ages ranging from 10's to 100's million yr younger than the host rock.

5.0 Methodology

This M.Sc. study comprises both field and laboratory approaches. Field work was completed in August of 2016, which included collecting sulfide samples from different localities of the Qaarsukassak Formation as well as generating a 1:10,000 scale geological map of the Discovery area (Figure 6.3).

5.1 Field studies

Field work occurred in the last two weeks of the 2016 expedition from August 10th to August 25th. A cargo boat was used as the main base camp with support from a helicopter and a zodiac to allow access into remote and unapproachable localities. A secondary basecamp was established for three days in the Discovery area (Figure 1.1) to generate a 1:10,000 scale map outlining the Qaarsukassak Formation. The rest of the 2 weeks were spent recording field observations within the Qaarsukassak and Marmorilik formations to revise previous mapping in the Discovery area (Coppard et al., 1992), and collect sulfide-bearing samples from the Qaarsukassak Formation for sulfur and lead isotopic analysis to compare with Marmorilik samples that were analyzed.

5.2 Petrography

Samples from Marmorilik include from seven different ore bodies (one sample per locality) and a sample from the South Lakes mineralized outcrop (Figure 2.5). Ore samples are from GEUS's archives and the South Lakes sample was collected during the 2015 expedition. Another three sulfide samples from the Qaarsukassak Formation were collected in the 2016 expedition. A total of 11 samples were selected for reflected/refracted light petrography. Samples were cut and prepared at the University of Saskatchewan's thin sectional laboratory. Transmitted light thin sections were cut to the standard thickness of 0.03mm and polished thin sections were cut to 0.05mm. Polished and regular thin sections were then analyzed using microscopes at the University of Saskatchewan Geological Sciences department.

5.3 Sulfur Analyses

5.3.1 Conventional isotope ratio mass spectrometry (IRMS)

Samples from the Black Angel Mine were cut in half and polished on the cut surface. Observing the polished surfaces, fourteen large pyrite grains were selected for an initial sulfur isotope analysis. The samples were obtained by drilling the exposed pyrite grains into a very fine powder with a diamond tipped micro-drill. The largest pyrite grains were selected to minimize possible contamination from the surrounding sulfide minerals, such as sphalerite and galena. Sulfur analyses were carried out by M. Yun at the University of Manitoba on a Thermo Delta V Plus using protocol procedures described in Hu et al. (2003).

Calibration was performed by analyzing two international Ag_2S standards at the beginning, middle, and the end of each run. One internal sulfide standard was analyzed with the pyrite samples to monitor the quality of analysis performance. The result of the internal standard analysis for this analysis was +3.6 ±0.2‰ (n=11). Analysis for one sample lasts ~45 min.

All sulfur isotope data are presented in the δ-notation relative to the appropriate standard. Sulfur isotopic composition is reported relative to the standard, Vienna Canyon Diablo Troilite (VCDT) in units of per mil (‰) (which has a $^{34}S/^{32}S$=0.0450045).

5.3.2 Scanning Electron Microscope (SEM)- Backscatter Electron Detector (BSE)

Eight polished thin sections were selected to further analyze to validate certain sulfide minerals, as well as, to generate "maps" for SIMS analysis. Analysis was conducted on the scanning electron microscope at the University of Saskatchewan. Polished thin sections were then coated with a thin conductive coating of carbon for preparation prior to scanning. The scanning electron microscope was adjusted to maximize the compositional differences between various sulfides.

5.3.3 In-Situ Secondary Ion Mass Spectrometry (SIMS)

In preparation for Secondary Ion Mass Spectrometry (SIMS) analysis, polished thin sections were cleaned and polished to remove the carbon coating, used for SEM. Each polished thin section was subsequently cleaned by immersing the thin sections in an ultrasonic cleaner, first using diluted dish soap, then tap water, purified water, and finally ethanol. The polished thin sections were then coated with a thin layer of gold to provide a conductive surface.

Sulfur isotope compositions of pyrite, pyrrhotite, and sphalerite were determined using the CAMECA 7f ion microprobe at the University of Manitoba. A ~2 nA primary beam of Cs^+ was accelerated at 10kV and focused to a 20 μm spot using a 100 μm aperture in the primary column. An offset of 300-volts was used to eliminate molecular ion interferences. Ions were detected with an ETP 133H electron multiplier coupled with an ion-counting system using an overall dead time of 22 ns. An electron gun was used for analyzing sphalerite grains for charge compensation. Two isotopes of sulfur, $^{34}S^-$ and $^{32}S^-$, were detected by switching the magnetic field. Analyses comprised 50 cycles and lasts ~7 minutes.

The standards used in this study were Anderson pyrrhotite (1.4‰) from Anderson Lake mine, Manitoba, as well as, Balmat sphalerite (14.3‰) and pyrite (15.1‰) from Balmat, New York (Crowe and Vaughan, 1996)

5.4 Pb-Pb Analysis

5.4.1 Multi- Collector Inductively Coupled Mass Spectrometry (MC-ICP-MS)

Four selected samples were analyzed by B. Eglington for Pb isotopic analysis at the University of Saskatchewan (Table 6.3 and 9.3). Three samples contained coarse-grained galena, from which galena grains were hand-picked; while the fourth, a gossan hand sample, was interpreted to have fine-grained galena, therefore was drilled into a fine powder. In preparation for analysis, the samples underwent dissolution and mineral separation using protocol procedures from Neuerburg (1975) and Ho et al., (1994).

Samples were measured by static multi-collection on a Thermo Electron Neptune MC-ICP-MS at the Saskatchewan Isotope Laboratory. Analysis used internal standard NIST-981.

5.5 Re-Os Analysis

A total of 10 samples of pyrite bearing rock were analyzed by R. Creaser at the University of Alberta. Pyrite mineral separate was prepared for each sample by metal-free crushing and grinding, followed by gravity and magnetic methods in heavy liquids. Then, one Re-Os analysis was performed by accurately weighing the sample and transferring it to a thick-walled, borosilicate glass Carius tube. An accurately weighed amount of a mixed $^{185}Re + ^{190}Os$ spike was added to the sample and dissolved at 220° C for 48 hours, followed by chemical separation and purification of Os and Re using procedures described in detail by Morelli et al. (2010) and references therein. Total procedure blanks were measured to be less than 1 picogram Re and 0.3 picogram Os (<0.01 picograms ^{187}Os). Decay constant used for ^{187}Re is that Smoliar *et al*. (1996) of $\lambda = 1.666e^{-11}$yr, a value which is cross-calibrated to the U-Pb system (^{238}U and ^{235}U) to better than ~0/3% (Selby et. al., 2007).

6.0 Results

6.1 Structural field data/ Geological Map of the Qaarsukassak Formation

Field work included collecting sulfide-bearing samples from different localities of the Qaarsukassak Formation (Table 9.1-9.5), as well as generating a new field map of the Discovery area in the Kangerdluarssuk Fjord, which has most continuous exposure of the Qaarsukassak Formation.

A 1:10,000 scale map was generated of the Qaarsukassak Formation in the Discovery area at the head of the Kangerluarsuk Fjord (Figure 6.1). The produced map highlights the extent of the exposed Qaarsukassak Formation as well as known sulfide occurrences. The width of the formation is marginally exaggerated due to large areas of scree in the area covering the basement and Qaarsukassak contact. Furthermore, exposures of the Qaarsukassak Formation are limited due to lack of preservation either by erosion, faulting, and degree of alteration/deformation upon the host rock. Fold limbs and hinges were difficult to define due to limited outcrop exposure. Observed folds ranged from open to isoclinal (Figure 6.2). Measurements on fold limbs were made throughout the Qaarsukassak Formation. Measurements (Figure 6.3) indicate a trend towards ~135°-155° (using Bingham analysis), consistent with the trend of the D3 compressional event, which is roughly NW-SE. Sulfide occurrences appear to be concentrated within some of these folds, which is similar to that recorded in the Marmorilik deformation on mineralization (Pedersen, 1980,1981). This deformation supports constraining the age of mineralization of both formations prior to the D3 deformation event.

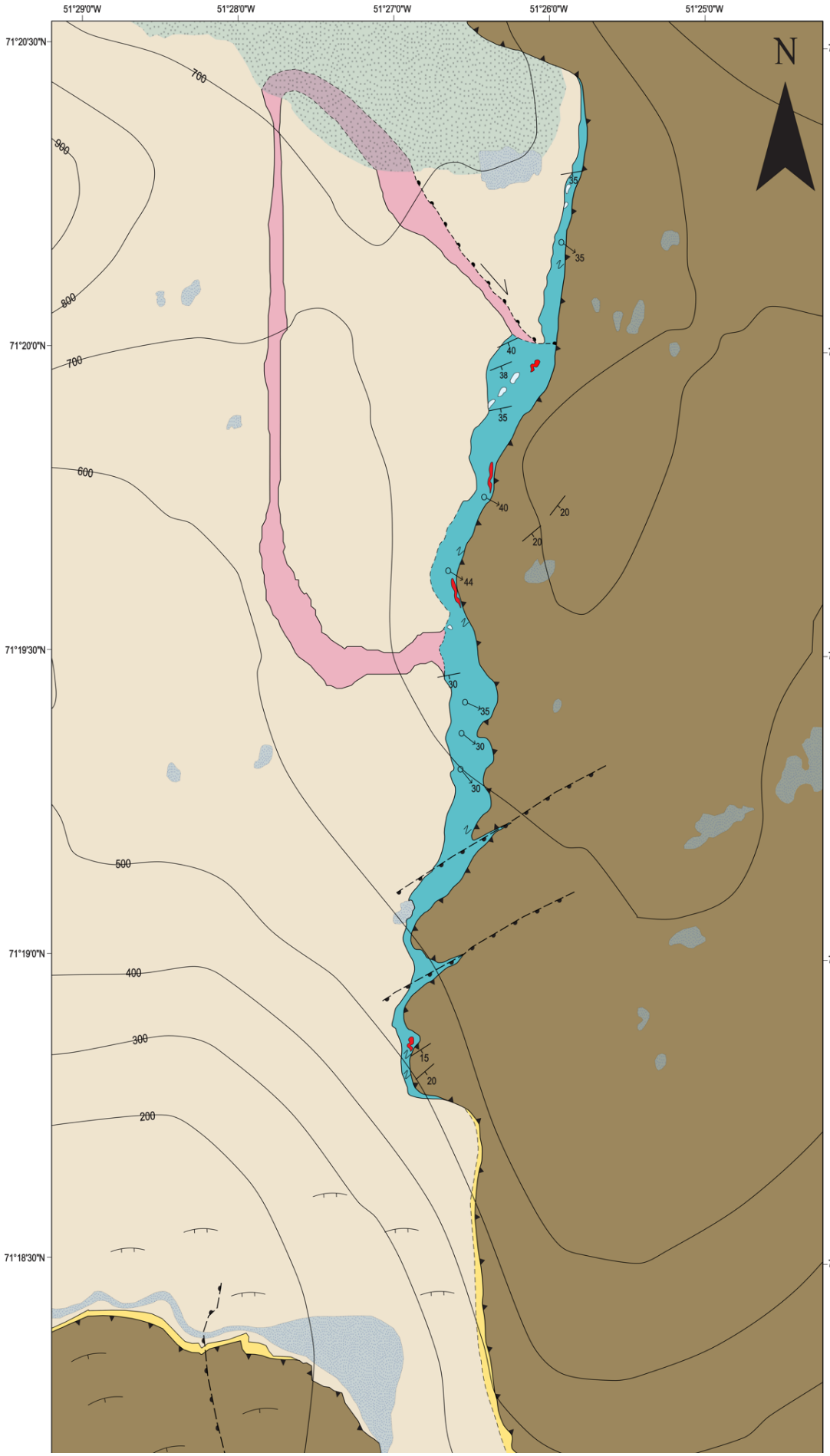

Geological Map of the "*Discovery Area*" Within Kangerdluarssuk Fjord, Greenland

Scale 1:10,000

0 500 Meters

0 0.1 0.2 0.3 Miles

Contour Interval = 100m

Legend

Quaternary

- Moraine
- Rivers/Lakes

Paleoproterozoic

- Nukavsak Formation
- Quartz Veins
- Qaarsukassak Formation
- Qeqetarssuaq Formation

Archean

- Dolerite Dyke
- Umanak Gneiss

- Contact, confirmed
- Contact, inferred
- Strike and dip of lithological layering
- 1°-20° Strike and dip from aerial photos
- 20°-55° Strike and dip from aerial photos
- Tight folds
- Fold axis with dip direction
- Normal Fault
- Thrust Contact
- Sulfide occurences

Figure 6.1 Geological map generated (1: 10,000 scale) of the Discovery area, outlining the exposed Qaarsukassak Formation (bright blue) and exposed outcrop with notable sulfide occurrences (red).

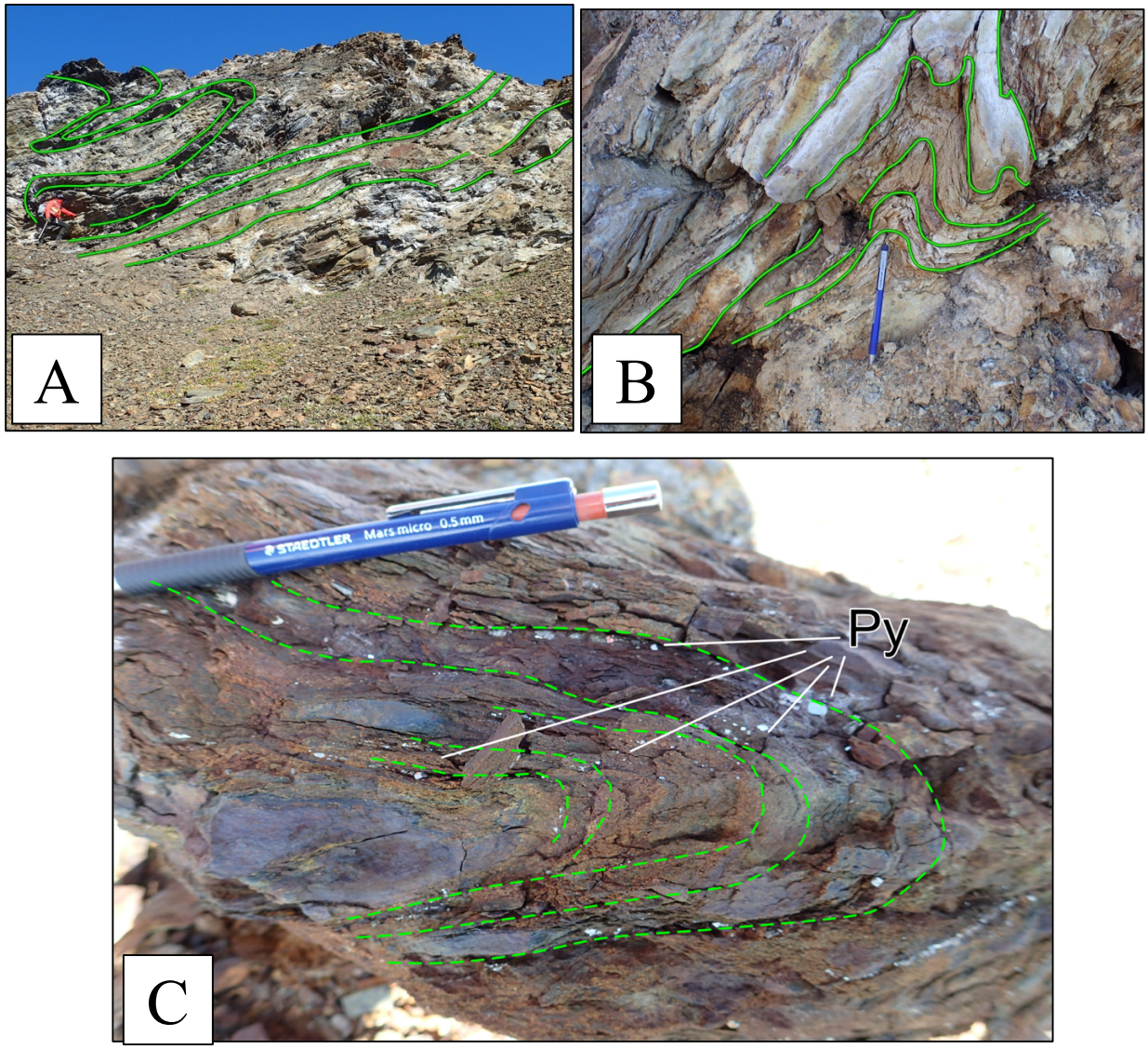

Figure 6.2 A) Outcrop scale examples of folding in the Qaarsukassak Formation. Green annotated lines to highlight the limbs of the folds. A) Example of a moderately plunging (~40º), reclined fold; B) Smaller scale of a tight fold; C) Hand sample of a tight fold with recrystallized, euhedral pyrite grains remobilized along the fold planes.

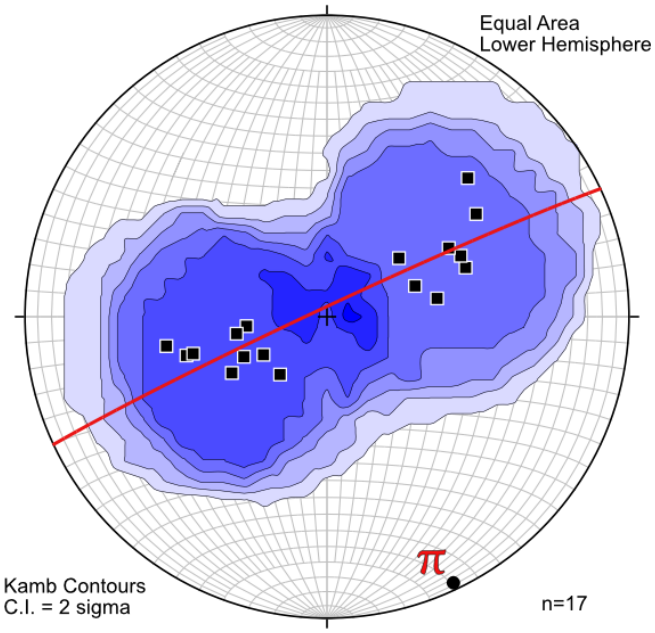

Figure 6.3 Stereographic plots measured fold limbs in the Qaarsukassak Formation in Discovery area. Figure generated on *Stereonet 9* (Cardozo, N. and Almendinger, R.W., 2013)

6.2 Petrographic Results

Petrographic samples include archive samples provided by GEUS and samples collected during the 2016 and 2017 field seasons (Table 9.5). Archive ore samples are derived from seven different ore bodies: Angel Zone, Cover Zone, Banana Zone, Tributary Zone, Deep Ice Zone, and Nunngarut 1/2 Zone (Figure 9.2). Samples were labelled as "buckshot ore" which can be classified as porphyroclastic ore, based on Pedersen's (1980) "ore tectonite facies classifications" within the Black Angel deposit. Other samples include a grab sample from "South Lakes" outcrop and massive sulfide grab samples from carbonate-shale localities, interpreted as the Qaarsukassak Formation (Figure 9.3). Samples are mainly composed of pyrite, sphalerite, galena ± chalcopyrite, pyrrhotite, and graphite. Gangue minerals include: dolomite, chlorite, tremolite, hematite, biotite and quartz.

6.2.1 Pyrite

Pyrite grains in Marmorilik samples exhibit variability in size (fine to coarse grained), shape (euhedral to anhedral), and textures such as replacement, annealing, cataclastic/fracturing, and durchbewegung. Numerous pyrite grains appear to have inclusions containing a mixture of minerals including sphalerite, galena, quartz, and carbonate. Reflected light and back-scatter imaging show small fractures leading towards the outer rim, indicating that the inclusions were likely replacement textures and leads to questioning other pyrite grains found with mineral "inclusions" with no apparent fractures **(**Figure 6.4 b, c, e**)**. Typical annealing textures (equant grains with 120º interfacial angles), cataclastic textures (brittle deformation and fracturing), and durchbewegung (well-rounded grains) are also found on various pyrite grains (Figure 6.4 f), supporting that deformation, metamorphism, remobilization, and recrystallizing did occur within this deposit (Craig and Vokes, 1993; Vokes, (1969)). Two generations of pyrite have been observed in Banana Ore Zone (367918). First generation by pyrites are characterized by being fairly-round (anhedral to subhedral) and coarse grained followed by a second pyrite phase described as finer to medium grained and euhedral in shape or in small, round blebs along sphalerite fractures (Figure 6.8 c, d).

Pyrite observed in Qaarsukassak Formation is either massive or medium grained, recrystallized (euhedral) along fold planes within the formation (Figure 6.2c). Massive pyrite in hand sample appeared to have no other minerals, however, sphalerite and pyrrhotite are identified using BSE imaging, cross-cutting the massive pyrite in a small veinlet (Figure 6.4 d).

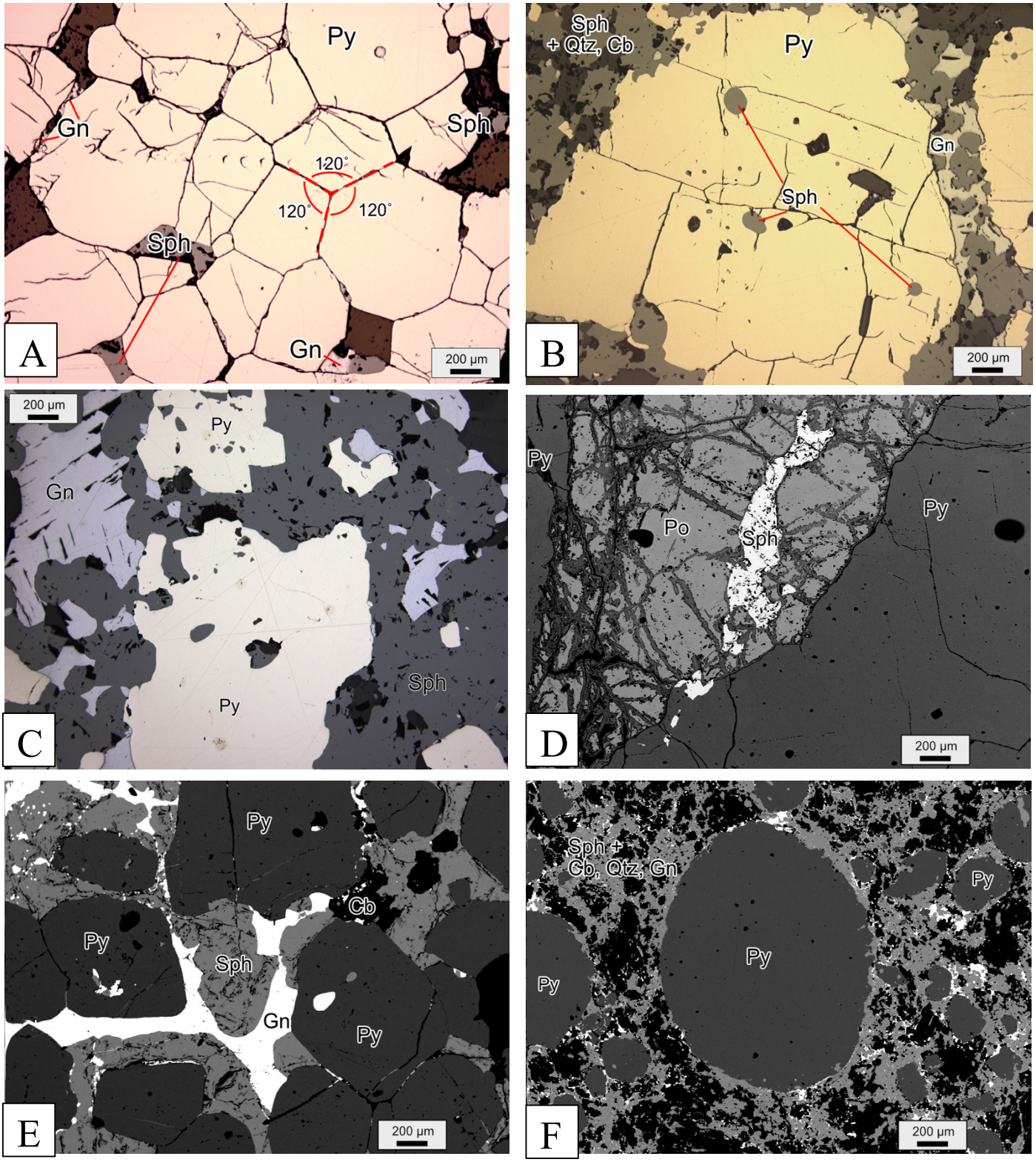
A
Py
Gn
Sph
120°
120°
120°
Sph
Gn
200 µm
B
Sph
+ Qtz, Cb
Py
Gn
Sph
200 µm
C
200 µm
Py
Gn
Sph
Py
D
Py
Po
Sph
Py
200 µm
E
Py
Cb
Py
Sph
Gn
Py
200 µm
F
Sph +
Cb, Qtz, Gn
Py
Py
Py
200 µm

Figure 6.4. Photomicrographs of pyrite in reflected light (RL) and in Back-scatter imaging (BSE): A) (367924) Massive pyrite showing annealing textures with annotated 120° angle between the 3 large grains (RL). Sphalerite and galena interstitially infilling any fractures or openings between the pyrite grains (RL).; B) (367918) Large, brittle pyrite grain with sphalerite replacing the pyrite along the outer rim of the pyrite grain. Sphalerite "inclusions" likely replacing the pyrite along fractures sets. (RL); C) (367918) Pyrite grains with sphalerite inclusions with no apparent fractures along surface. (RL); D) (572201) pyrrhotite and sphalerite cross-cutting massive pyrite. (BSE); E) (569813) Annealing pyrite grains that are also fractured with sphalerite and galena infilling those fractures (BSE).; F) (367931) Sub-rounded pyrite grains displaying durchbewegung texture. Disseminated galena (white), sphalerite (pale grey), and quartz/carbonate are in the matrix of this porphyroclastic sample (BSE).

6.2.2 Pyrrhotite

Pyrrhotite was only found in Qaarsukassak samples in this study. Though it was not found in Black Angel samples in this study, it occurs as an accessory mineral in the Black Angel deposit (Thomassen, 2003). Observed pyrrhotite in Qaarsukassak samples is fine-grained in host rock or massive euhedral- to subhedral grains and is observed to be cross-cut by sphalerite (Figure 6.5 a). Many pyrrhotite grains exhibit alteration halos, with evident changes from the core to the outer rim of the grain (Figure 6.5 b). A possible explanation is that the alteration halo could likely be related to the emplacement of the sphalerite or simply surface weathering.

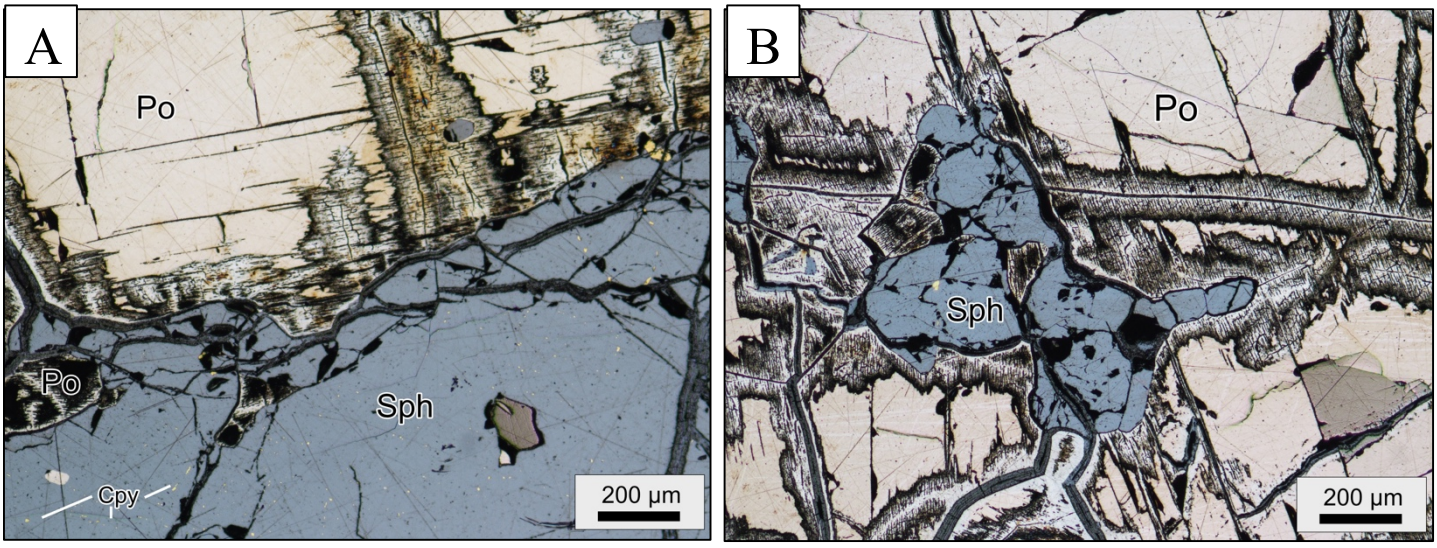

Figure 6.5. Photomicrographs of pyrrhotite in reflected light (RL). A) (572204) Large pyrrhotite grain with sphalerite infilling in fractures and replacing pyrrhotite. Minor chalcopyrite found in fractures of sphalerite (RL).; B) Sphalerite replacing pyrrhotite. Pyrrhotite exhibiting alteration rims around the grain and along fractures (RL).

6.2.3 Sphalerite

The matrix in the majority of samples is dominated by sphalerite. Grain size ranged from very fine (disseminated)- to medium-grained, varying from sample to sample. Sphalerite's internal reflection can vary from a pale yellow/green to a deep red, likely due to a lack or enrichment in Fe-content, respectively (Figure 6.6). Sphalerite exhibits lamellar twinning, which corroborates the deformation that occurred in this deposit. Sphalerite is shown replacing pyrite and can occur as possible inclusions in pyrite, but this is uncertain as possible inclusions are likely syn/post-deformation with fractures connecting from the source of the inclusion to the outside rim of the pyrite grains (Figure 6.4 b, c, e).

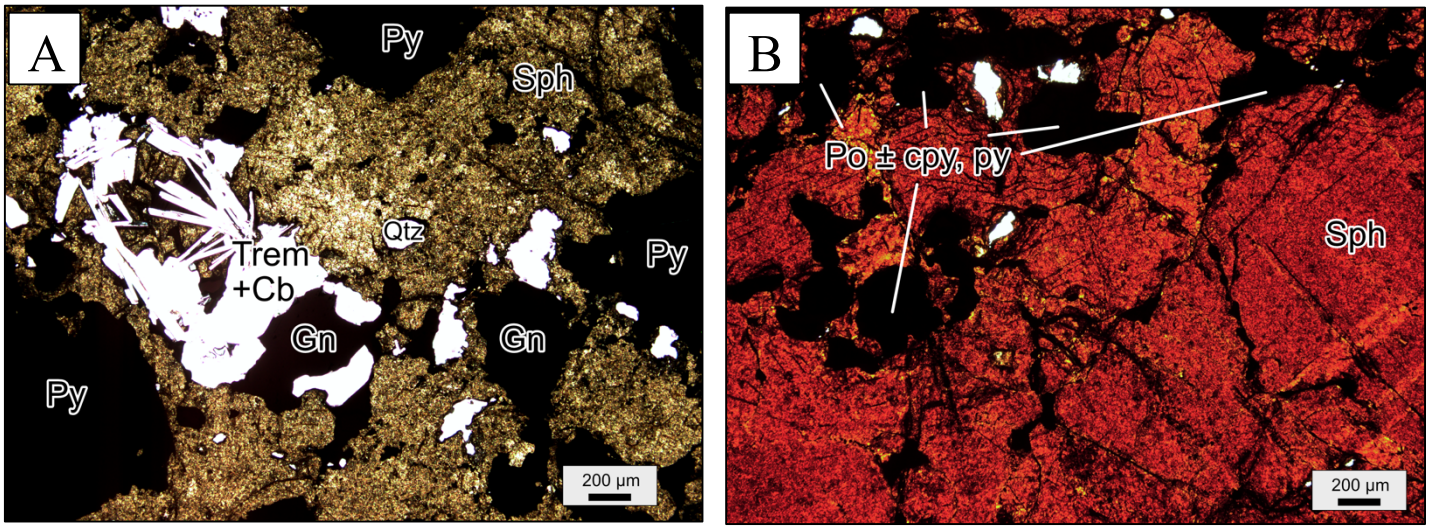

Figure 6.6. Photomicrographs of sphalerite in plane polarized view (PPL). Massive sphalerite varying in internal reflections from pale yellow (A – 367921) to a deep red (B – 572204)). Secondary minerals include: Pyrite (Py), Pyrrhotite (Po), Chalcopyrite (cpy), Galena (Gn), Quartz (Qtz), Tremolite (Trem), and Carbonate (Cb).

6.2.4 Galena

Galena is observed in every Black Angel sample and absent from Qaarsukassak samples. Euhedral cubic shapes, which are typical for galena, are absent in all samples and instead, found either disseminated around pyrite, interstitially or replacing pyrite and sphalerite, as it is likely one of the last minerals to precipitate, infilling any available open spaces in the ore (Figure 6.7). Bends and kinks can also be found in the cleavage of the galena, indicating that it is deformed. Galena is also found in association with chalcopyrite.

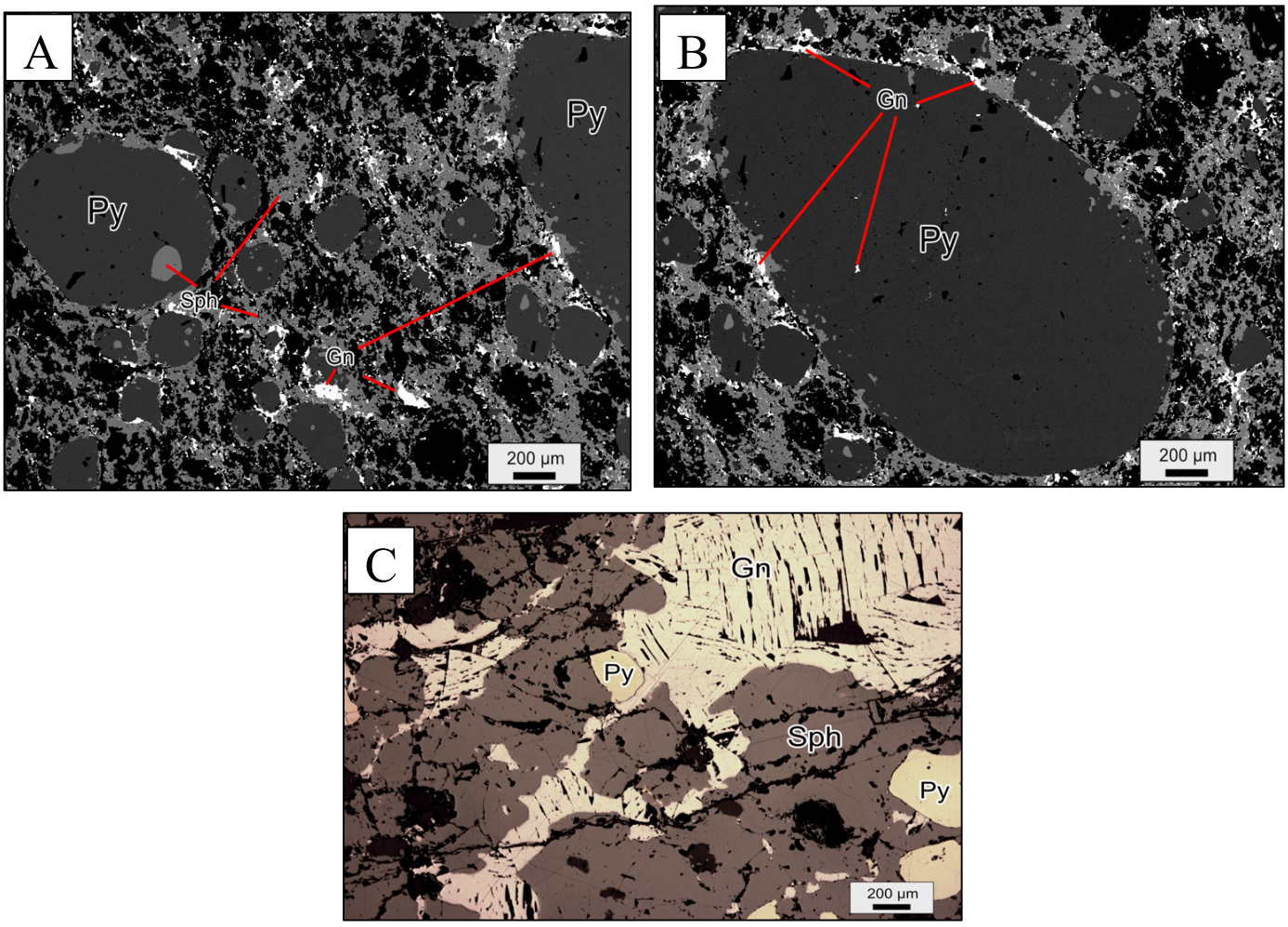

Figure 6.7 Photomicrographs of galena in both reflected light (RL) and back-scatter imaging (BSE): A+B) (367931) Well-rounded pyrite grains with disseminated sphalerite and galena with possible inclusions (BSE).; C) (569813) Deformed galena showing bends and kinks in the cleavage as well as replacing the sphalerite (RL).

6.2.5 Chalcopyrite

Though chalcopyrite is not abundant in the samples in this study, minor chalcopyrite is observed. Chalcopyrite is associated with galena and sphalerite based on the observed polished thin sections. It is found interstitially, precipitating after galena. Chalcopyrite is also found as small blebs in linear orientations, precipitating along fractures and cracks within sphalerite grains,

suggesting a late stage precipitation. This has been interpreted as a "chalcopyrite disease", related to solid-state diffusion reactions and occurring at elevated temperatures (Barton and Bethke, 1987; Blesgen et al., 2004).

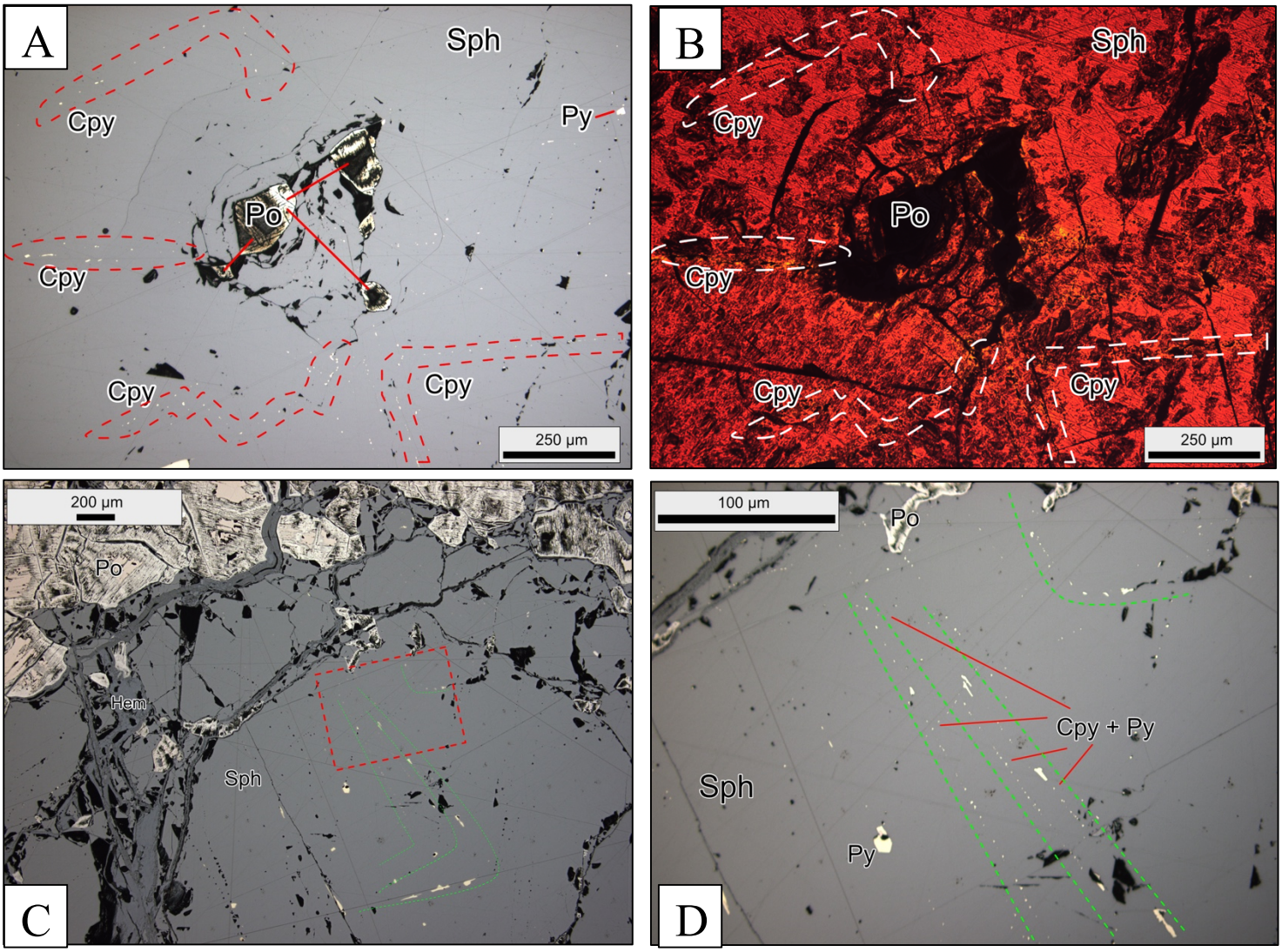

Figure 6.8 Photomicrographs of chalcopyrite using plane polarized view (PPL) and reflected light (RL): A) (572204) Massive sphalerite surrounding pyrrhotite with chalcopyrite along fractures (RL).; B) Complementary photo of (A) to identify fracture sets under transmitted light (PPL); C) (572204) Massive sphalerite with chalcopyrite and pyrite along fractures (annotated in green). Annotated red square represents photo (D) (RL); D) Zoomed in (10x) of photo (C), highlighting the linear trend where chalcopyrite and pyrite are precipitating (RL).

6.2.6 Graphite

Graphite was not found in any of the archive ore samples but was found in the collected South lakes sample (569813), as well as in Qaarsukassak samples (Table 9.5). It is found mostly very fine grained in the host rock and associated with pyrite (Figure 6.9). A later, deformed stage of graphite was found in a Qaarsukassak sample, however, it unclear if this graphite is a second phase of mineral growth or remobilized graphite.

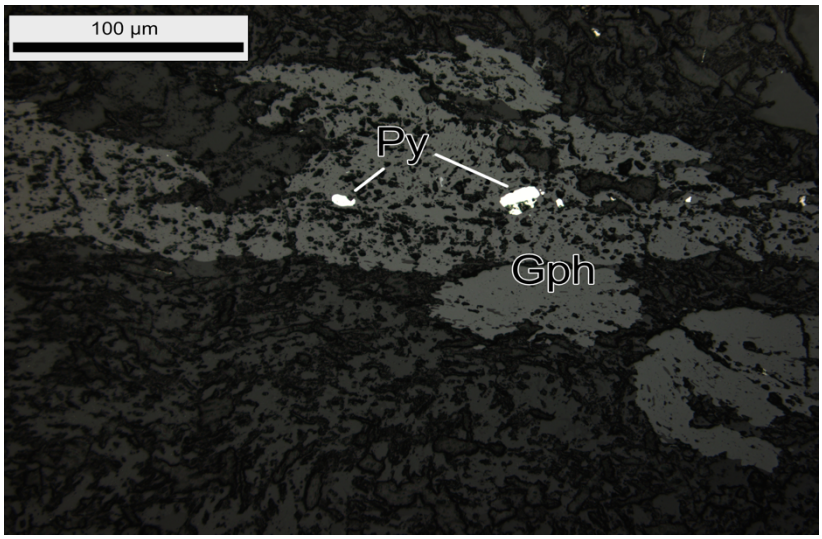

Figure 6.9 Photomicrographs of graphite using reflected light (RL). (572205) Small amounts of pyrite in primary graphite.

6.2.7 Hematite

Hematite is present in the massive sphalerite samples from Qaarsukassak (Table 9.5). This is likely a weathering alteration of the samples as they are near surface grab samples (Figure 6.8 c).

6.2.8 Paragenetic sequence

Based on the petrographic observations, a paragenetic sequence on the porphyroclastic ore mineralization for Black Angel as well as the mineralization in the Qaarsukassak Formation was developed (Figure 6.10).

The Black Angel host rock is dominated by dolomite with minor quartz, graphite, and tremolite. Other localities also include a graphitic, semi-pelitic composition. The large porphyroclastic pyrite can be found fractured, deformed, and annealed depending on the sample (i.e. locality of ore body). These varying deformed pyrite grains are interpreted to be the same phase of pyrite, however undergone various degrees of deformation, varying from ore body to ore body. These large, deformed pyrite grains are interpreted to be first crystallized, subsequently with sphalerite and galena crystallizing, replacing pyrite and host rock, however, it is unclear if the pyrite and ore minerals are coeval or if multiple stages of ore mineralization occurred given the extensive deformation in the ore zone. Numerous pyrite grains contain "inclusions" which include sphalerite and galena, however with numerous fractures in the pyrite grain leading to these "inclusions" deems it unlikely. Various samples show galena as well as chalcopyrite crystallizing after sphalerite, infilling voids as well as replacing the sphalerite. Chalcopyrite and a smaller, secondary pyrite phase can be found along sphalerite fractures as well as replacing galena, placing the crystallization chalcopyrite and second pyrite phase after the main Pb-Zn mineralization.

Two massive-sulfide samples containing sphalerite are found in the Qaarsukassak Formation (572201, 572204). The ore mineralization shows disseminated pyrite associated with graphite within the host rock. It appears to be following the foliation of the host rock. Massive pyrite is observed with pyrrhotite and sphalerite crystalized within small fractures. Massive pyrrhotite is also observed with sphalerite crosscutting it. Minor blebs of chalcopyrite and pyrite can be found along fractures of the sphalerite, pacing the crystallization after the sphalerite. Galena was not present in any samples from the Qaarsukassak Formation. Hematite was also found cross-cutting the sphalerite and is interpreted to be a result of surface weathering. A possible later stage graphite was observed in a gossan area interpreted to be part of the Qaarsukassak Formation, however, it is unclear whether the graphite is the first graphite observed but remobilized or a new hydrothermal graphite.

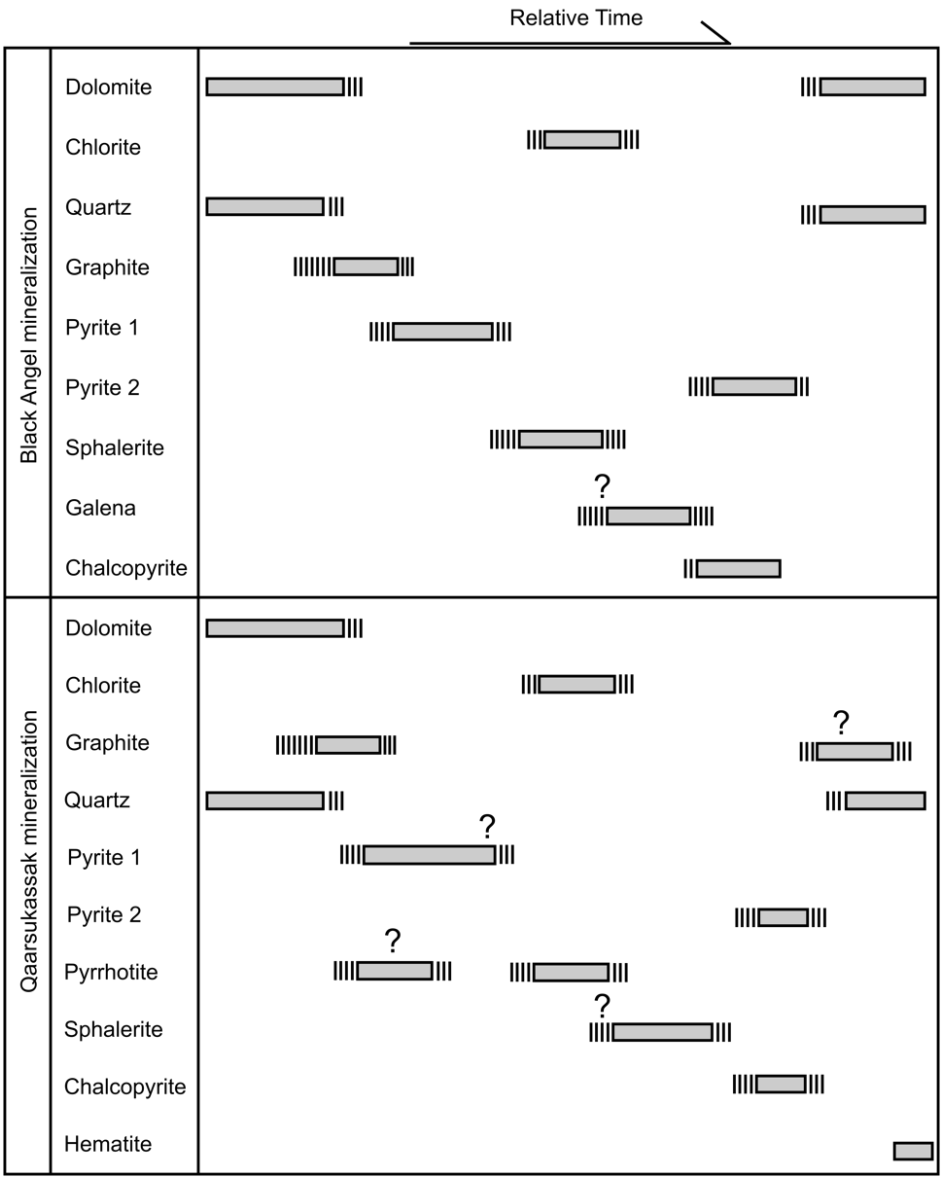

Figure 6.10. Paragenetic sequence for general ore mineralization in both, the Marmorilik and Qaarsukassak formations.

6.3 Sulfur Isotopic Compositions

6.3.1 Isotope-Ratio Mass Spectrometry (IRMS) Analysis

Using conventional IRMS (Thermo Delta V), sulfur isotopic measurements from the Black Angel mine were carried out on pyrite for preliminary $\delta^{34}S$ analysis. The sulfur isotope compositions are reported in Table 6.1 and presented on Figure 6.11, highlighting the ore bodies and the $\delta^{34}S$ values that are found in orebody. The 14 analyses of pyrite produced a range from +0.2 ‰ to +7.2‰ (±0.2‰) (VCDT). The $\delta^{34}S$ values within each ore zone showed little variability.

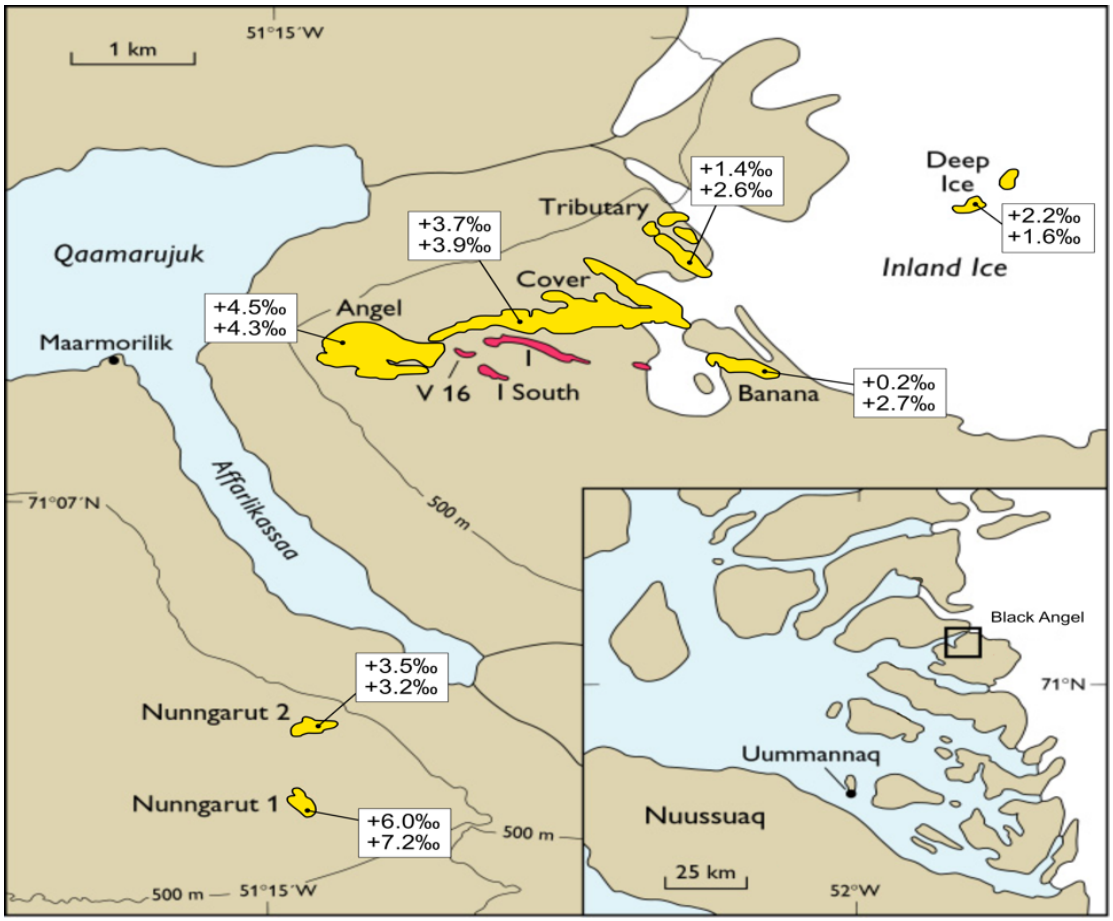

Figure 6.11 Map outlining the ore zones at Black Angel Mine highlighting the ore zones that were analyzed via IRMS from porphyroclastic pyrite grains (yellow). Pyrite $\delta^{34}S$ sulfur values displayed next to the ore where it was analyzed.

Table 6.1 Sulfur isotopic data for pyrite in the Black Angel Mine (Marmorilik Formation). [1]Localities: NZ1-Nunngarut Zone 1, NZ2 – Nunngarut Zone 2, AZ – Angel Zone, CZ – Cover Zone, BZ – Banana Zone, TZ – Tributary Zone, DIZ – Deep Ice Zone. Localities are described in Table 9.1

Lab ID	Sample ID	Sulfide Mineral	Location[1]	$\delta^{34}S$ (‰, VCDT)	Analytical error (‰)
EA(S)-16-0097	T1	Pyrite	NZ1	6.0	0.2
EA(S)-16-0098	T2	Pyrite	NZ1	7.2	0.2
EA(S)-16-0099	T3	Pyrite	AZ	4.5	0.2
EA(S)-16-0100	T4	Pyrite	AZ	4.3	0.2
EA(S)-16-0101	T5	Pyrite	CZ	3.7	0.2
EA(S)-16-0102	T6	Pyrite	CZ	3.9	0.2
EA(S)-16-0103	T7	Pyrite	BZ	0.2	0.2
EA(S)-16-0104	T8	Pyrite	BZ	2.7	0.2
EA(S)-16-0107	T9	Pyrite	TZ	1.4	0.2
EA(S)-16-0108	T10	Pyrite	TZ	2.6	0.2
EA(S)-16-0109	T11	Pyrite	NZ2	3.5	0.2
EA(S)-16-0110	T12	Pyrite	NZ2	3.4	0.2
EA(S)-16-0111	T13	Pyrite	DIZ	2.2	0.2
EA(S)-16-0112	T14	Pyrite	DIZ	1.6	0.2

6.3.2 Secondary-ion mass spectrometry (SIMS) Analysis

In-situ sulfur isotope measurements were carried out on pyrite, sphalerite, pyrrhotite (py, sph, and po, respectively) in polished thin sections. These data are presented in Table 6.2 and as histograms in Figure 6.12. Three areas were analyzed from Black Angel: the Angel zone (367904) and Nuggrarut 2 zone (367931) orebodies, as well as, a Pb-Zn exposed outcrop at South Lakes (569813). The other three samples were grab samples of Qaarsukassak mineralization (572201, 572204-3, and 572204-4). The 11 analyses of pyrite, pyrrhotite, and sphalerite (py, po, and sph, respectively) in 572201 range from 0.2‰ to 4.1‰, with a median of +1.9‰. Sulfur isotope compositions of po are slightly higher than that of py and sph in this sample (Figure 6.12). The 11 analyses of py and po in 572204-3 range from 4.2‰ to 6.0‰, with a median of +5.2‰. Sulfur isotope composition in the sphalerite showed no variation, changing less than the standard deviation (i.e., 0.3‰). The range in po and sph samples in 572204-4 is 3.1‰ to 6.5‰, and median of +5.2‰. The 19 analyses on py and sph in 569813 range from 0.7‰ to 6.9‰, the median +3.0‰. While this sample produced the largest sulfur isotope composition range, the range between minerals showed a smaller range of 1.5‰ and 3.9‰ for pyrite and sphalerite, respectively. The isotopic compositions on py and sph in 367931 showed a similar range as 569813 (1.6‰ to 6.2‰). The isotope compositions of py and sph in 367904 yielded a range of 0.9‰ to 6.1‰, with a median of +3.8‰. Sphalerite grains showed more variation than the previous ore zones mentioned (up to +5‰). Overall, the 94 S isotope analyses have a variation from 0.2‰ to 6.9‰ and a median of +4.1‰.

Isotopic composition of pyrite grains in the analyzed samples tend to have a lighter composition than the main Pb-Zn sulfides suggesting that the pyrite formed at a different time than the main ore sulfides, supported by petrographic observations.

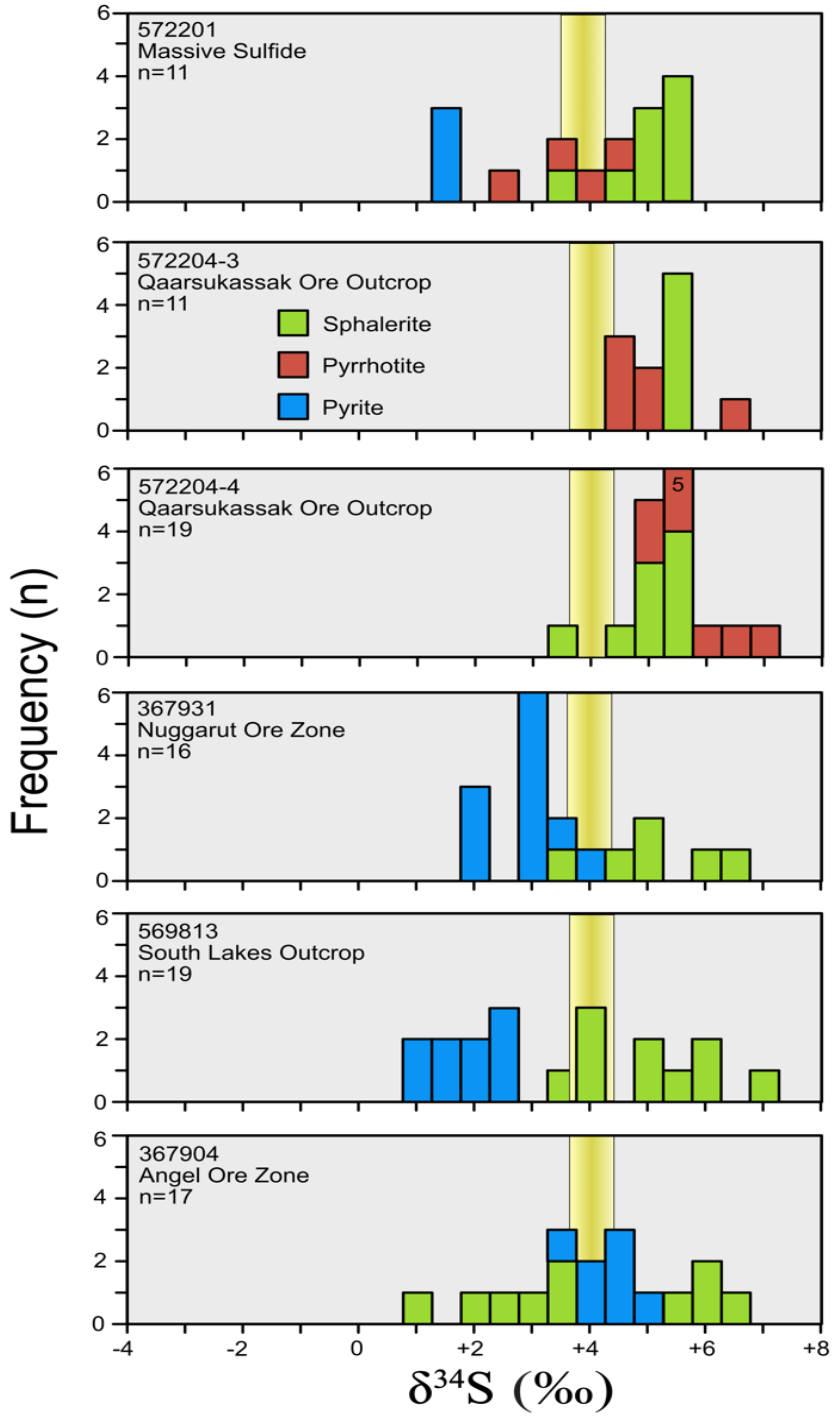

Figure 6.12 Stacked histograms of (py, po, or sph) $\delta^{34}S$ values obtained via SIMS. Yellow bar represents the median value (4.1‰ ± 0.3‰) from the entire dataset. (Green-sphalerite; Red-Pyrrhotite; Blue-Pyrite)

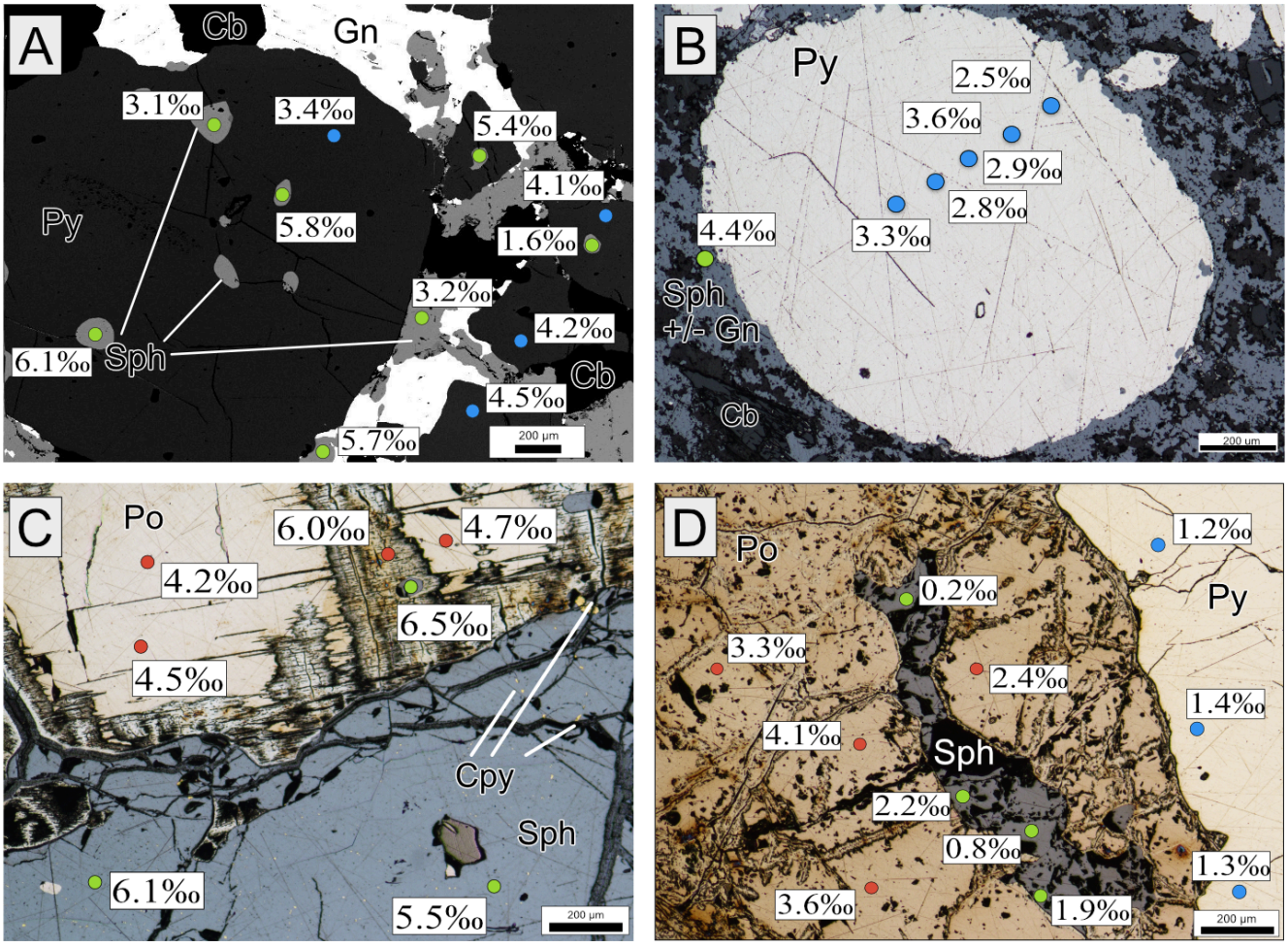

Figure 6.13 Photomicrographs of various ore zones from Marmorilik (A+B) and Qaarsukassak (C+D) Formation in both reflected light and in back-scatter imaging. Annotations are $\delta^{34}S$ values of sulfide minerals including: Sphalerite (Sph- green spots), Pyrite (Py- blue spots), and Pyrrhotite (Po- red spots).

Table 6.2 In situ $\delta^{34}S$ isotope data for sulfide minerals (py, po, sph) in Marmorilik and Qaarsukassak Formation by SIMS analysis. [1]Sample localities for Marmorilik samples can refer to Table 6.1. Localities not already mentioned: QO- Qaarsukassak outcrop; DISC- 'Discovery proper' ore outcrop; SLO- South Lakes Outcrop (Table 9.2).

Sample ID	Sulfide Mineral	Location[1]	Spot #	$\delta^{34}S$ (‰, VCDT)	Analytical error (‰)	Spot-to-Spot on standard (‰)
572201	Pyrite	QO	1	1.3	0.3	0.3
572201	Pyrite	QO	2	1.4	0.3	0.3
572201	Pyrite	QO	3	1.2	0.3	0.3
572201	Pyrrhotite	QO	1	3.6	0.3	0.3
572201	Pyrrhotite	QO	2	2.4	0.3	0.3
572201	Pyrrhotite	QO	3	3.3	0.3	0.3
572201	Pyrrhotite	QO	4	4.1	0.3	0.3
572201	Sphalerite	QO	1	0.8	0.3	0.5
572201	Sphalerite	QO	2	1.9	0.3	0.5
572201	Sphalerite	QO	3	2.2	0.3	0.5
572201	Sphalerite	QO	4	0.2	0.3	0.5
572204-3	Pyrrhotite	DISC	5	5.0	0.3	0.4
572204-3	Pyrrhotite	DISC	2	4.2	0.3	0.4
572204-3	Pyrrhotite	DISC	3	4.5	0.3	0.4
572204-3	Pyrrhotite	DISC	4	4.7	0.3	0.4
572204-3	Pyrrhotite	DISC	5	6.0	0.3	0.4
572204-3	Pyrrhotite	DISC	6	4.4	0.3	0.4
572204-3	Sphalerite	DISC	1	5.2	0.3	0.3
572204-3	Sphalerite	DISC	2	5.3	0.3	0.3
572204-3	Sphalerite	DISC	3	5.3	0.3	0.3
572204-3	Sphalerite	DISC	4	5.4	0.3	0.3
572204-3	Sphalerite	DISC	5	5.5	0.3	0.3
572204-4	Pyrrhotite	DISC	1	5.2	0.3	0.4
572204-4	Pyrrhotite	DISC	2	4.7	0.3	0.4

572204-4	Pyrrhotite	DISC	3	5.4	0.3	0.4
572204-4	Pyrrhotite	DISC	4	6.2	0.3	0.4
572204-4	Pyrrhotite	DISC	5	5.2	0.3	0.4
572204-4	Pyrrhotite	DISC	6	5.2	0.3	0.4
572204-4	Pyrrhotite	DISC	7	5.6	0.3	0.4
572204-4	Pyrrhotite	DISC	8	4.8	0.3	0.4
572204-4	Pyrrhotite	DISC	9	5.2	0.3	0.4
572204-4	Pyrrhotite	DISC	10	6.5	0.3	0.4
572204-4	Sphalerite	DISC	1	4.5	0.3	0.3
572204-4	Sphalerite	DISC	2	5.2	0.3	0.3
572204-4	Sphalerite	DISC	3	4.7	0.3	0.3
572204-4	Sphalerite	DISC	4	3.1	0.3	0.3
572204-4	Sphalerite	DISC	5	4.8	0.3	0.3
572204-4	Sphalerite	DISC	6	5.4	0.3	0.3
572204-4	Sphalerite	DISC	7	5.1	0.3	0.3
572204-4	Sphalerite	DISC	8	4.7	0.3	0.3
572204-4	Sphalerite	DISC	9	5.2	0.3	0.3
367931	Pyrite	NZ1	1	3.3	0.3	0.2
367931	Pyrite	NZ1	2	2.8	0.3	0.2
367931	Pyrite	NZ1	3	2.9	0.3	0.2
367931	Pyrite	NZ1	4	3.6	0.3	0.2
367931	Pyrite	NZ1	5	2.5	0.3	0.2
367931	Pyrite	NZ1	6	2.8	0.3	0.2
367931	Pyrite	NZ1	7	1.9	0.3	0.2
367931	Pyrite	NZ1	8	1.6	0.3	0.2
367931	Pyrite	NZ1	9	1.8	0.3	0.2
367931	Pyrite	NZ1	10	2.5	0.3	0.2
367931	Pyrite	NZ1	11	2.9	0.3	0.2
367931	Sphalerite	NZ1	1	4.6	0.3	0.3
367931	Sphalerite	NZ1	2	3.5	0.3	0.3
367931	Sphalerite	NZ1	3	6.2	0.3	0.3

367931	Sphalerite	NZ1	4	5.8	0.3	0.3
367931	Sphalerite	NZ1	5	4.8	0.3	0.3
367931	Sphalerite	NZ1	6	4.4	0.3	0.3
569813	Pyrite	SLO	1	1.0	0.3	0.3
569813	Pyrite	SLO	2	0.9	0.3	0.3
569813	Pyrite	SLO	3	2.0	0.3	0.3
569813	Pyrite	SLO	4	1.8	0.3	0.3
569813	Pyrite	SLO	5	2.2	0.3	0.3
569813	Pyrite	SLO	6	1.8	0.3	0.3
569813	Pyrite	SLO	7	1.1	0.3	0.3
569813	Pyrite	SLO	8	0.7	0.3	0.3
569813	Pyrite	SLO	9	2.3	0.3	0.3
569813	Sphalerite	SLO	1	4.8	0.3	0.5
569813	Sphalerite	SLO	2	3.0	0.3	0.5
569813	Sphalerite	SLO	3	3.9	0.3	0.5
569813	Sphalerite	SLO	4	5.8	0.3	0.5
569813	Sphalerite	SLO	5	5.7	0.3	0.5
569813	Sphalerite	SLO	6	5.5	0.3	0.5
569813	Sphalerite	SLO	7	6.9	0.3	0.5
569813	Sphalerite	SLO	8	4.6	0.3	0.5
569813	Sphalerite	SLO	9	3.9	0.3	0.5
569813	Sphalerite	SLO	10	3.7	0.3	0.5
367904	Pyrite	AZ	1	3.4	0.3	0.2
367904	Pyrite	AZ	2	4.5	0.3	0.2
367904	Pyrite	AZ	3	4.2	0.3	0.2
367904	Pyrite	AZ	4	4.1	0.3	0.2
367904	Pyrite	AZ	5	3.8	0.3	0.2
367904	Pyrite	AZ	6	4.7	0.3	0.2
367904	Pyrite	AZ	7	3.6	0.3	0.2
367904	Sphalerite	AZ	1	3.1	0.3	0.5
367904	Sphalerite	AZ	2	6.1	0.3	0.5

367904	Sphalerite	AZ	3	1.6	0.3	0.5
367904	Sphalerite	AZ	4	3.2	0.3	0.5
367904	Sphalerite	AZ	5	5.8	0.3	0.5
367904	Sphalerite	AZ	6	5.7	0.3	0.5
367904	Sphalerite	AZ	7	5.4	0.3	0.5
367904	Sphalerite	AZ	8	2.8	0.3	0.5
367904	Sphalerite	AZ	9	0.9	0.3	0.5
367904	Sphalerite	AZ	10	2.1	0.3	0.5

6.4 Pb-Pb isotopic compositions

The Pb isotopic compositions of the sulfides from the Black Angel Pb-Zn deposit and Qaarsukassak Formation are listed in Table 6.3 and shown in Figure 6.14. The sulfide samples have $^{206}Pb/^{204}Pb$ ratios ranging from 16.091 to 16.305, $^{207}Pb/^{204}Pb$ ratios ranging from 15.378 to 15.445 and $^{208}Pb/^{204}Pb$ ratios ranging from 36.282 to 36.550. Seven internal NIST 981 standards produced a standard deviation of 0.001 (0.003%) for all Pb ratios.

Galena samples from various ore zones in the Black Angel (AZ, DIZ, and IZ) have a relatively homogenous cluster next to the historical Pb-Pb mean (n=33) for Black Angel, reported in Sangster et al. (2000) from previous unpublished work. Sample "KS" is slightly elevated in respect to its $^{206}Pb/^{204}Pb$ and $^{207}Pb/^{204}Pb$ ratio when compared the rest of the samples. Beam intensity during mass spectrometric analysis of sample "KS" indicates a much lower Pb content than in the other samples, indicating that no galena is present.

Table 6.3 Pb-Pb isotopic data for galena in the Black Angel Pb-Zn Deposit and Qaarsukassak mineralization, Greenland. [1]Samples localities are referenced in appendix (Table 9.4): AZ-Angel Zone, DIZ- Deep Ice Zone, KS- Kangerluarssup Sermia, IZ- I Zone, BA- Black Angel sample average from Sangster et al., (2000).[2] Error noted in 2 sigma external uncertainties. Localities described in Table 10.3

Sample Name[1]	Identity	$^{206}Pb/^{204}Pb$	Error[2] (%)	$^{207}Pb/^{204}Pb$	Error[2] (%)	$^{208}Pb/^{204}Pb$	Error[2] (%)	$^{207}Pb/^{206}Pb$	Error[2] (%)	$^{208}Pb/^{206}Pb$	Error[2] (%)
AZ	Galena	16.091	0.003	15.378	0.003	36.282	0.003	0.9556	0.001	2.25477	0.001
DIZ	Galena	16.102	0.003	15.385	0.003	36.318	0.003	0.9555	0.001	2.25542	0.001
IZ	Galena	16.096	0.003	15.379	0.003	36.297	0.003	0.9554	0.001	2.25491	0.001
KS	Gossan	16.305	0.003	15.445	0.003	36.550	0.003	0.9473	0.001	2.24163	0.001
BA	Galena	16.109	0.042	15.388	0.018	36.302	0.046	0.9552	0.001	2.2536	0.007

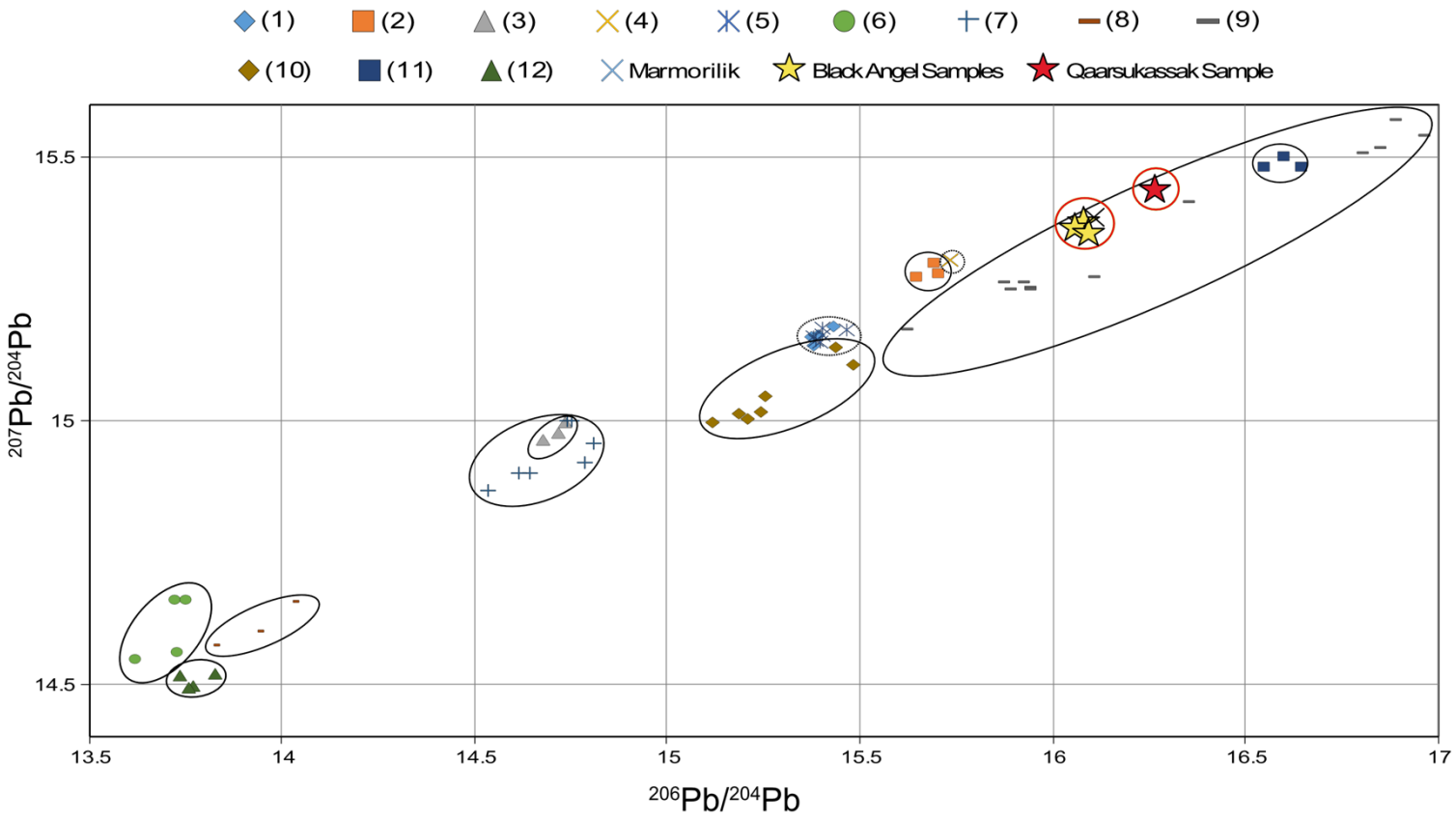

Figure 6.14. Pb-Pb isotopic data from the Rinkian Domain (Figure 4.3a) with new data, highlighted with red circles. Yellow stars- Galena samples derived from Marmorilik Formation; Red star- Gossan sample derived from Qaarsukassak outcrop.

6.5 Re-Os isotopic compositions

In total, seven Re-Os isotope analyses were obtained from three of the 12 sulfide samples. The three samples were from 569806 (ore outcrop from 'Discovery proper'), 367920 and 367918 (Banana Ore Zone). Most of the sulfide samples were not suitable for analyses due to non-sufficient Re content (569813, 568702, 367904, 367921, 367924, 367929, and 367931). Three samples showed suitable Re content, though were not able to be analyzed due to: 1) very low Re-Os ratio (~60) and non-radiogenic Os, likely to derive a very imprecise age; 2) repeated analysis for Re content not corroborating with the initially collected high Re and; 3) interior of the rock completely weathered, thus pyrite recovery was too small to be used.

The total Re and Os abundances of the pyrite samples range from 2.718- to 7.054 ppb (parts per billion) and 93.2 to 302 ppt (parts per trillion), respectively (Table 6.4). The 7 Re-Os analyses of pyrite show a large range of Re/Os ratios between 60.40 and 1132, with radiogenic $^{187}Os/^{188}Os$ ratios up to 37.19 (Table 6.4). A range of model ages for individual grains yielded between 2332 ± 22 Ma and 1891 ± 15 Ma. The regression of all the Re-Os data using *Isoplot V 4*.0 (Ludwig, 2003) yields a Model 3 Re-Os age of 1910 ± 89 Ma, with an initial $^{187}Os/^{188}Os$ of 1.1 ± 1.3 (2σ, Mean Squared Weighted Deviates [MSWD] = 30) (Figure 7.8). The former age is anchored by the sample from Qaarsukassak (569806) with low Re/Os ratio. Using only samples from the Banana Ore zone, (367918 and 367920), a Model 3 Re-Os isochron age is derived at 1570 ± 170 Ma, with an initial $^{187}Os/^{188}Os$ of 6.9 ± 3.0 (2σ, Mean Squared Weighted Deviates [MSWD] = 3.3).

Table 6.4 Re-Os isotopic data for pyrite in the Marmorilik and Qaarsukassak formations.

[1]Last letter of each sample number denotes a repeat analysis of the same mineral separate; [2]Uncertainty reported as ± standard error (2SE); [3]Model ages assumes an initial chondrite Os value of 0.5 (Walker and Morgan, 1989). Localities described in Table 10.4.

Sample[1]	Re (ppb)	±[2]	Os (ppt)	±[2]	$^{187}Re/^{188}Os$	±[2]	$^{187}Os/^{188}Os$	±[2]	Model Age[3] (Ma)	±[2]
569806-A	3.798	0.015	409.0	1.1	60.40	0.36	2.834	0.021	2275	19
569806-B	2.718	0.011	302.0	1.0	58.63	0.39	2.822	0.025	2332	22
367918-A	3.535	0.016	95.0	2.4	883	19	30.23	0.68	1987	17
367918-B	3.707	0.014	99.7	2.5	896	19	30.79	0.70	1996	21
367918-C	3.505	0.013	93.2	2.2	920	20	31.40	0.66	1982	9
367920-A	7.054	0.026	175.2	2.3	1132	12	37.19	0.44	1915	13
367920-B	6.999	0.026	172.3	2.5	1123	13	36.46	0.49	1891	15

7.0 Discussion

7.1 Possible fluid source(s) for the Pb-Zn mineralization in the Karrat Group

7.1.1 Modeling sulfur data

The Marmorilik and Qaarsukassak $\delta^{34}S$ sulfur data show a narrow range between +0.2‰ and +7.2‰ (Figure 6.12). One might speculate that the $\delta^{34}S$ values from the pyrite, sphalerite, and pyrrhotite might have been isotopically homogenized due to regional metamorphism, consequently reducing the isotopic variations (Schwarcz and Burnie, 1973). This type of homogenization has been recorded in other sedimentary-hosted deposits such as the Balmat-Edwards Zn-Pb district in northwestern New York (Whelan et al., 1984) with $\delta^{34}S$ values analyzed from this deposit showing a narrow range from +12.7‰ to +14.7‰. If the $\delta^{34}S$ sulfur values in the Karrat Group are homogenized due to metamorphism, then interpretations with respect to mineralization presented in this thesis would be invalid. This section discusses the possibility of isotopic equilibration.

In the mid-Proterozoic Balmat-Edwards Zn-Pb deposit, Whelan et al. (1984) suggest that isotopic equilibrium took place during recrystallization of sulfides with peak metamorphic conditions recorded at an upper amphibolite facies of ~6.5kb and ~625°C, erasing many primary petrographic and chemical characteristics of the ore and their host rocks. However, homogenization via regional metamorphism is not as straightforward as other massive sulfide deposits, which have preserved sulfur isotope values that have not been equilibrated by metamorphism such as the Aggneys-Gamsberg deposit in South Africa with peak metamorphic conditions of ~670°C and 5kb (Von Gehelen et al., 1983) or sulfide deposits in the Norwegian Caledonides (Cook and Hoefs, 1997) that show up to upper amphibolite facies conditions (Corfu et al., 2014). Sulfur isotopic analyses conducted in these deposits were targeted in their sample localities to avoid any possible homogenized values. This was achievable by selecting less deformed localities within the deposit, conjecturing that homogenization did not affect the sulfur isotopic composition of sulfides at a regional scale, but rather at a local scale (Cook and Hoefs, 1997).

Zheng (1990) discusses the behavior of sulfur isotopes during regional metamorphism. He examines the mechanisms of kinetic and thermodynamic fractionation between sulfur-bearing minerals under metamorphic conditions and homogenization as well. Zheng (1990) explains that the sulfur isotopic distributions in all metamorphic rocks are most influenced by their original isotopic signatures thus large scale pre-metamorphic sulfur variations are generally preserved in a deposit scale. However, caution is needed in interpreting the sulfur isotopic signatures in metamorphosed ores as there are many factors which can influence sulfur isotope abundances and the collected data could be explained in more than one way.

Evaluating one of the samples from the Nuggarut ore zone (367931), sub-rounded porphryoclastic pyrites interpreted as derchwerbegung texture (Pedersen, 1980) were present. These large, sub-rounded grains provide a test for metamorphism/ deformation, as they appear to not have been recrystallized and formed prior to the deformation/remobilization event. This was conducted by analyzing multiple spots (spot size 20μm) on a single grain from the center to the outer rim. The sulfur isotope compositions on the pyrite grain (Figure 7.1) show a narrow range between 2.5‰ and 3.6‰ (±0.3‰) with no apparent trends or heterogeneity which suggests that the deformation/metamorphism was not strong or long-lasting enough to change the values within the pyrite. Recrystallized pyrite grains from the other ore bodies displayed similar values as the large rounded pyrite grain, suggesting that the $\delta^{34}S$ values within the pyrite grains are likely the original value.

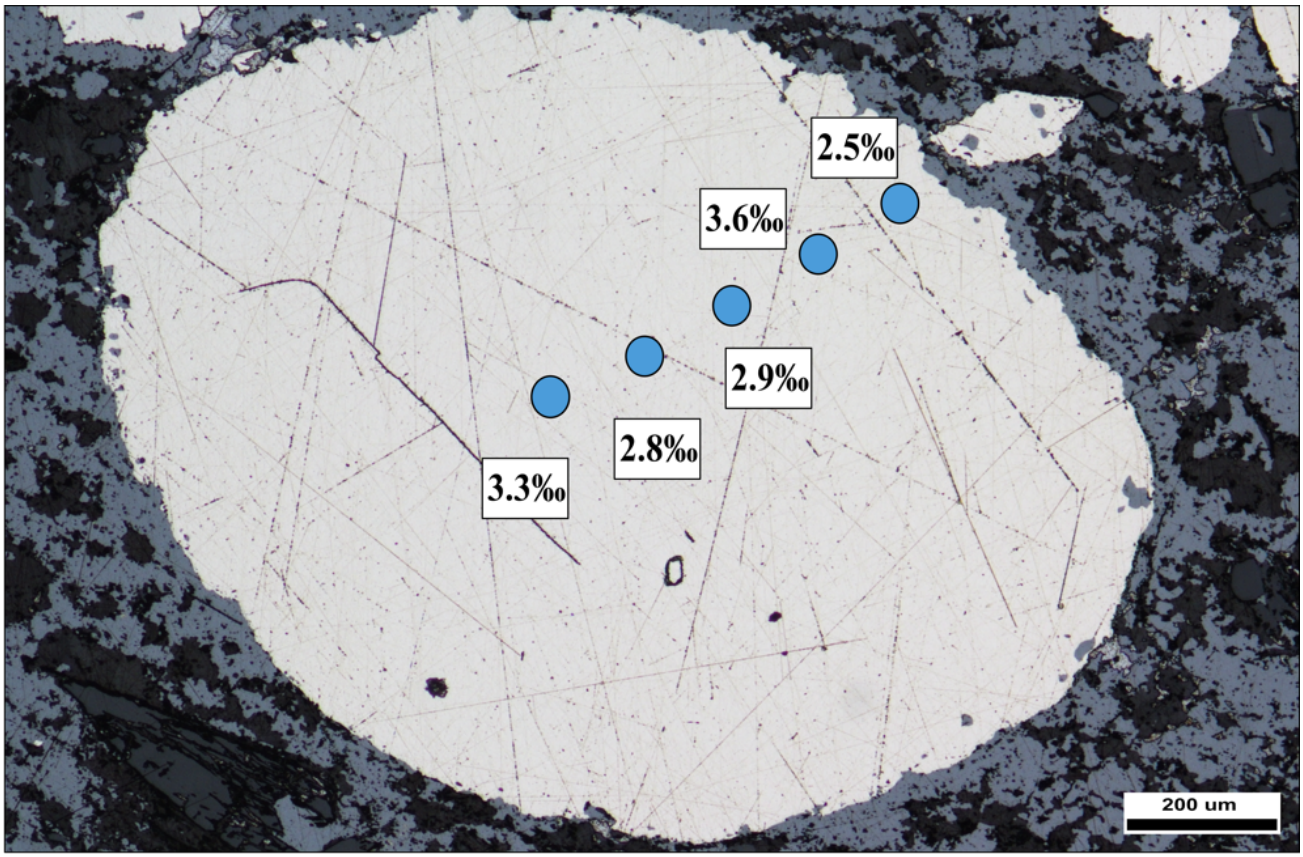

Figure 7.1 Reflected light (RL) image of sub-rounded pyrite grain from Nuggarut ore zone (367931) displaying relatively homogenous $\delta^{34}S$ values (VCDT) across the grain.

7.1.2 Controls and Source of Sulfur

Major sources of sulfur in sedimentary-hosted deposits are derived from: 1) seawater sulfate reduced by either bacterial sulfate reduction or moderately higher temperature thermochemical sulfate reduction; 2) mantle derived or mobilization of sulfur within a basaltic material; 3) an evaporitic source ($\delta^{34}S$ values greater than coeval seawater sulfate); or 4) a combination from any of these processes. While the source of sulfur is a large contributor to the $\delta^{34}S$ values observed, there are many factors that affect the sulfur isotope signature of hydrothermal sulfide minerals such as equilibrium fractionation which includes: temperature, pH, and fO_2 of the fluid (Sakai, 1968; Ohmoto, 1972). Kinetic fractionation is another factor in the

$\delta^{34}S$ values in which how open or closed the system is with respect to H_2S or SO_4 and can affect the distribution of $\delta^{34}S$ values. This section investigates the likelihood of each possible source of sulfur for the Karrat mineralization, which can indicate a possible genetic model for the mineralization. However, the coeval seawater sulfate has yet to be determined for the Black Angel deposit/Qaarsukassak mineralization. The secular variation curve presented by Farquhar et al. (2010), $\delta^{34}S$ value of seawater during the late Paleoproterozoic is around 21‰ and will be assumed for the purposes of this discussion.

Bacterial sulfate reduction (BSR) is a process with anaerobic bacteria oxidizing organic matter and utilizing sulfate as an electron acceptor (Berner, 1989). BSR causes large fractionation between H_2S and SO_4 at low temperatures, typically no greater than ~80°C (Ohmoto, 1986). As the ^{32}S is favoured over the ^{34}S via BSR, $\delta^{34}S$ values can be quite negative, fractionating as large as 40‰ lighter than the coeval seawater sulfate, and can show a gradation towards heavier $\delta^{34}S$ values in closed systems, known as Rayleigh fractionation (Ohmoto, 1986). However, $\delta^{34}S$ values within this study do not show a large fractionation; the maximum fractionation in this study is ~20‰ from the assumed coeval seawater sulfate value of 21‰. With the presence of rogenpyrite in the Angel Ore Zone (Pedersen, 1980), contribution from BSR was likely involved in this system. A plausible explanation to link BSR and a lack of negative $\delta^{34}S$ values could be from either from a combination of high rates of bacterial sulfate reduction or sulfides formed syn-diagenetically in euxinic sediments in a restricted sub-basin, consequently limiting the supply of sulfate replenishment (Lyons et al., 2006). Limiting the supply of sulfate can shift the range of $\delta^{34}S$ values more positive. BSR limited to sulfate may be a possible mechanism as previous papers hypothesize sub-basins within the Karrat, specifically, Maarmorilik and Qaarsukassak hosted within a sub-basin/ paleo-topography (Rosa et al., 2016 and references therein; Guarneri et al., 2016).

Thermochemical sulfate reduction (TSR) processes occur at higher temperatures (~150°C -250°C) and can fractionate $\delta^{34}S$ values up to 15‰ from the coeval seawater sulfate (Machel et al., 1995). A figure can be produced using the calculations provided by Kiyosu and Krouse (1990) to display the likely range of $\delta^{34}S$ values that can be produced via TSR in sediment-hosted deposits throughout geologic time (Figure 7.3). With an assumed value of 21‰ for the coeval seawater sulfate (~1.9 Ga), fractionation via TSR can range from 21‰ to 7‰, assuming a closed system to both SO_4^{-2} and H_2S. With the $\delta^{34}S$ values ranging from 0.2‰ to 7.2‰ (±0.3‰), it can be suggested

that TSR could be involved in the reduction of sulfate but unlikely to be the dominant process involved. If the source of sulfur were to be derived from an evaporitic source, the initial $\delta^{34}S$ value of SO_4 would be greater than the coeval seawater sulfate value (> 21‰). Using the range to which TSR can fractionate (up to 15‰), this will derive heavier $\delta^{34}S$ values, which are not found in this study, therefore evaporites are an unlikely source of sulfur for the mineralization (Figure 7.2).

Sulfur of magmatic origin has a narrow composition close to that of meteorites, with a $\delta^{34}S$ value of 0‰ (±3‰) (Seal, 2006). Initially, this was a probable explanation for the Marmorilik/Qaarsukassak values since many carbonate replacement or manto-type deposits exhibit a similar range of $\delta^{34}S$ values. However, no direct field evidence of intrusive activity has been found in either the Marmorilik Formation or the Qaarsukassak Formation (Rosa et al., 2017), likely eliminating a magmatic origin as an option for sulfur source.

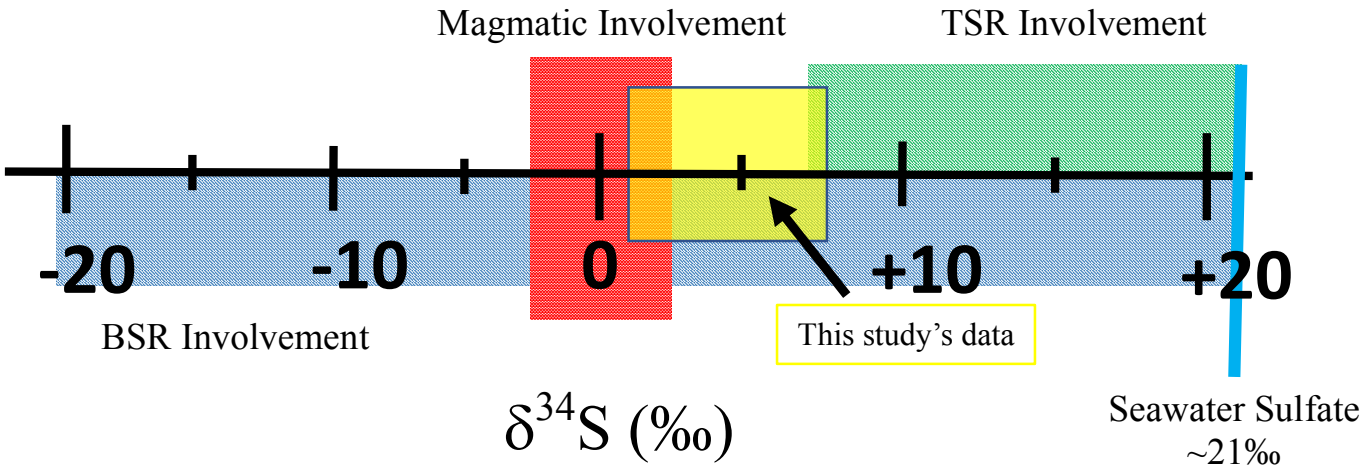

Figure 7.2 Schematic diagram comparing sulfur isotopic analysis in this study (highlighted in yellow) with various possible fractionation processes including: magmatic involvement (red), thermochemical sulfate reduction (TSR) (green), and bacterial sulfate reduction (BSR) (blue). Blue line represents the coeval seawater sulfate value at ~1.9 Ga.

7.1.3 Comparing with other known deposits

Using data from figures in Chapter 4 (Figure 4.1, 4.2), a figure can be generated to compare the sulfur data collected in this study and other known sedimentary hosted deposits (Figure 7.3). This illustration shows both BSR and TSR involvement within most SEDEX type deposits in contrast to MVT deposits, which displays a dominant TSR involvement. The anomalously negative $\delta^{34}S$ values are separated from the MVT and SEDEX deposits and classified as Irish-Type deposits (highlighted in green on Figure 7.4). The $\delta^{34}S$ values in the Marmorilik and Qaarsukassak formations appear to lie in the BSR and TSR ranges, suggesting multiple processes could have affected this deposit. This observation is analogous to other Proterozoic SEDEX deposits (Figure 7.4) such as the Rampura-Agucha deposit, George Fisher, and HYC.

7.1.4 Geothermometry

Geothermometry can be a beneficial tool in understanding the temperatures at which the ore sulfide precipitated under equilibrium conditions by measuring the difference in their $\delta^{34}S$ values (Ohmoto and Rye 1976). This type of analysis is based on three assumptions: 1) minerals are formed contemporaneously and in equilibrium with one another at a single temperature; 2) re-equilibration or alteration of one or both minerals must not have occurred; and lastly, 3) the temperature dependence of the fractionation factors must be known. When analyzing co-existing adjacent sulfides in a single sample, the sulfides did not have the correct order of enrichment of $\delta^{34}S$ values under equilibrium conditions (Kajiwara and Krouse 1971; Ohmoto and Rye 1979): pyrite > pyrrhotite = sphalerite > chalcopyrite > galena. The pyrite grains were lower in $\delta^{34}S$ enrichment compared to the adjacent sphalerite and pyrrhotite grains and therefore are likely in disequilibrium. Consequently, measuring fractionations between sulfides could not be attained for geothermometry analyses. This analysis would have helped clarify equilibrium temperatures thus identifying sulfate reduction/source mechanisms (e.g., BSR temperature limit under 80°C). Providing better constraints to identify the likelihood of each mechanism would be ideal for any future sulfide $\delta^{34}S$ analyses on this deposit.

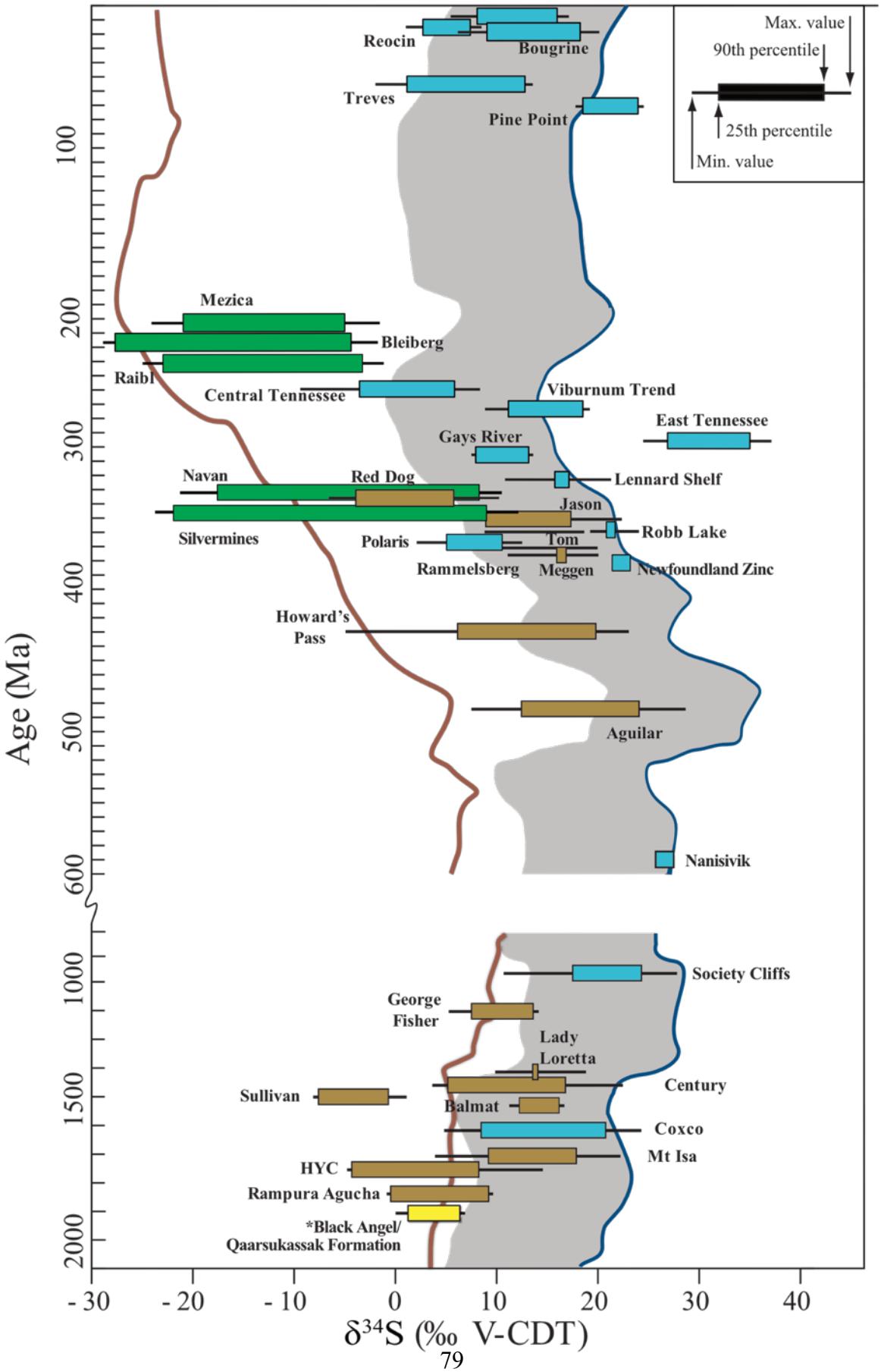
Max. value
90th percentile
25th percentile
Min. value
Reocin
Bougrine
Treves
Pine Point
Mezica
Bleiberg
Raibl
Central Tennessee
Viburnum Trend
East Tennessee
Gays River
Navan
Red Dog
Lennard Shelf
Jason
Silvermines
Polaris
Tom
Robb Lake
Rammelsberg
Meggen
Newfoundland Zinc
Howard's Pass
Aguilar
Nanisivik
Society Cliffs
George Fisher
Lady Loretta
Century
Sullivan
Balmat
Coxco
Mt Isa
HYC
Rampura Agucha
*Black Angel/ Qaarsukassak Formation
Age (Ma)
100
200
300
400
500
600
1000
1500
2000
- 30
- 20
- 10
0
10
20
30
40
δ34S (‰ V-CDT)

Figure 7.3 Boxplot diagram illustrating the range of $\delta^{34}S$ values (x-axis) from this study (yellow bar) compared to a selection of sedimentary-hosted deposit throughout geologic time (y-axis) including: SEDEX (brown), MVT (light blue), and Irish type deposits (green). Deposits are plotted at their approximate mineralization age. Sulfide mineral sulfur isotope values are compared with the coeval seawater sulfate (navy blue line) and mean sedimentary pyrite composition (red line) as produced by BSR. Gray shaded field indicates the likely range of sulfide compositions produced via TSR of seawater derived sulfate (Kiyosu and Krouse, 1990). Figure modified after Wilkinson, 2014.

7.1.2 Modeling available Pb data

7.1.2.1 Model Age and the Likely Source(s) of Pb

A regression age for the Pb-Pb analysis derived an age of 3529 ± 270 Ma (Figure 7.4). However, the gossan sample (KS-572207) anchors that regression line. Using only the galena samples from the Marmorilik Formation derives a regression age of 4744 ± 6100 Ma. Both of these ages are too old to provide a geologically meaningful age as one age is older than the age of the Earth. Therefore, the Pb-Pb analysis for this study did not provide a model age for the mineralization rather, a homogenized signal likely representing a mixing line.

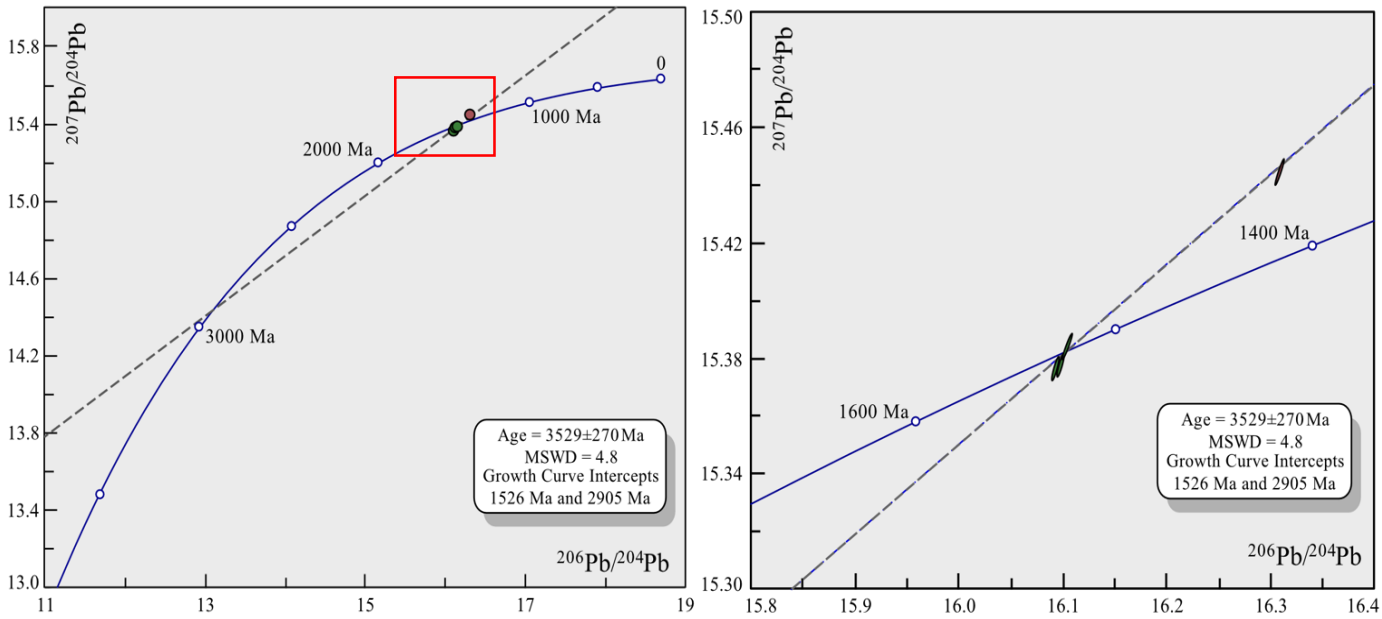

Figure 7.4 (Left) $^{207}Pb/^{204}Pb$ vs. $^{206}Pb/^{204}Pb$ diagram calculated, using Isoplot/Ex (Ludwig, 2003) showing the analyzed samples within this study; (Right) Zoomed in $^{207}Pb/^{204}Pb$ vs. $^{206}Pb/^{204}Pb$ diagram. Evolution curves for crustal Pb after Stacy and Kramers, 1975. Error ellipses (2σ) are smaller than the sample symbols. Green circles = Marmorilik Formation galena; Purple circle = Qaarsukassak Formation gossan.

The Pb-Pb isotopic composition of the interpreted Qaarsukassak Formation gossan has a different isotopic signature than the three galena samples from the Marmorilik Formation (Figure 7.4). Based on the hypothesis in Chapter 1, this would suggest that the mineralization in the Qaarsukassak Formation is different than the Marmorilik Formation. However, the gossanous sample showed a much lower Pb content compared to the galena samples when analyzed on the MC-ICP-MS, suggesting that galena is not likely present in the sample. Consequently, the question for the coeval mineralization between the Marmorilik Formation and Qaarsukassak Formation cannot be answered with Pb isotope data in this study.

The Pb isotopic compositions of galena from the three different ore zones in the Marmorilik Formation form a homogenous cluster, consistent with the average Pb composition (n=33) recorded in Sangster et al. (2000) (Figure 6.14). The Pb isotopic compositions for the Marmorilik Formation also plot along the terrestrial Pb growth curve (Stacy and Kramers, 1975), suggesting a crustal component for the Pb source. The homogenous signature in the Marmorilik Formation

suggests that the Pb-Zn orebodies were formed by the same or a similar process and that the ore components were mainly derived from the same single source or, alternatively, formed from fluids in which Pb derived from different metal sources has been well homogenized.

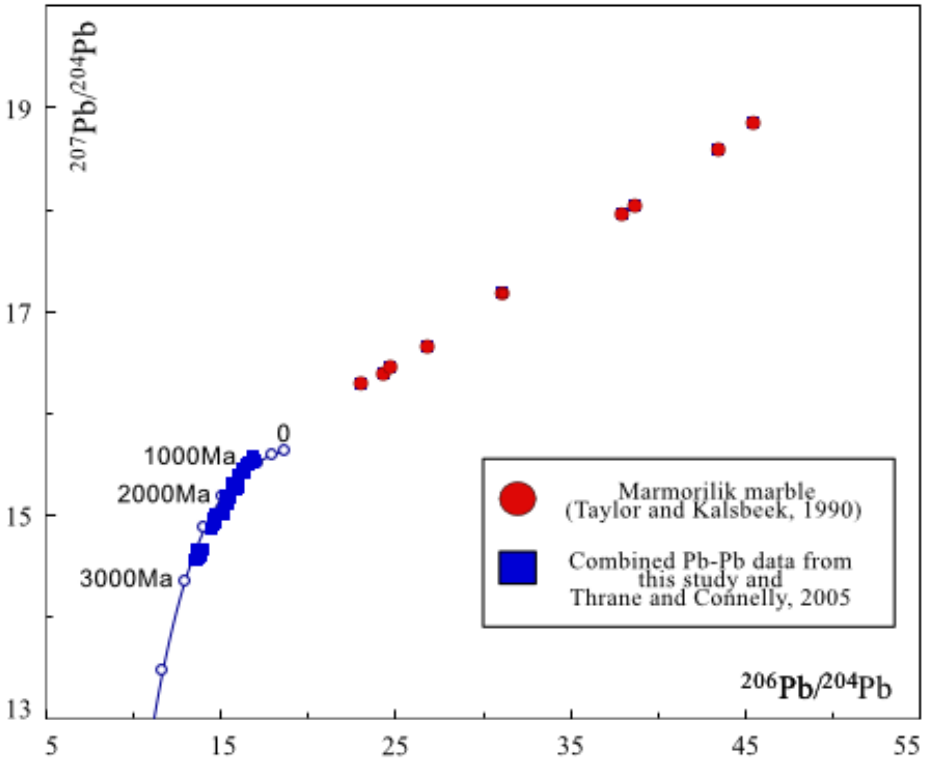

Figure 7.5 Pb isotopic compositions from various sources, including: marble from Marmorilik Formation (Taylor and Kalsbeek, 1990) (red circles) as well as, regional basement rocks (Thrane and Connelly, 2005) and galena from this study (blue squares). Evolution curve for crustal Pb after Stacy and Kramers (1975).

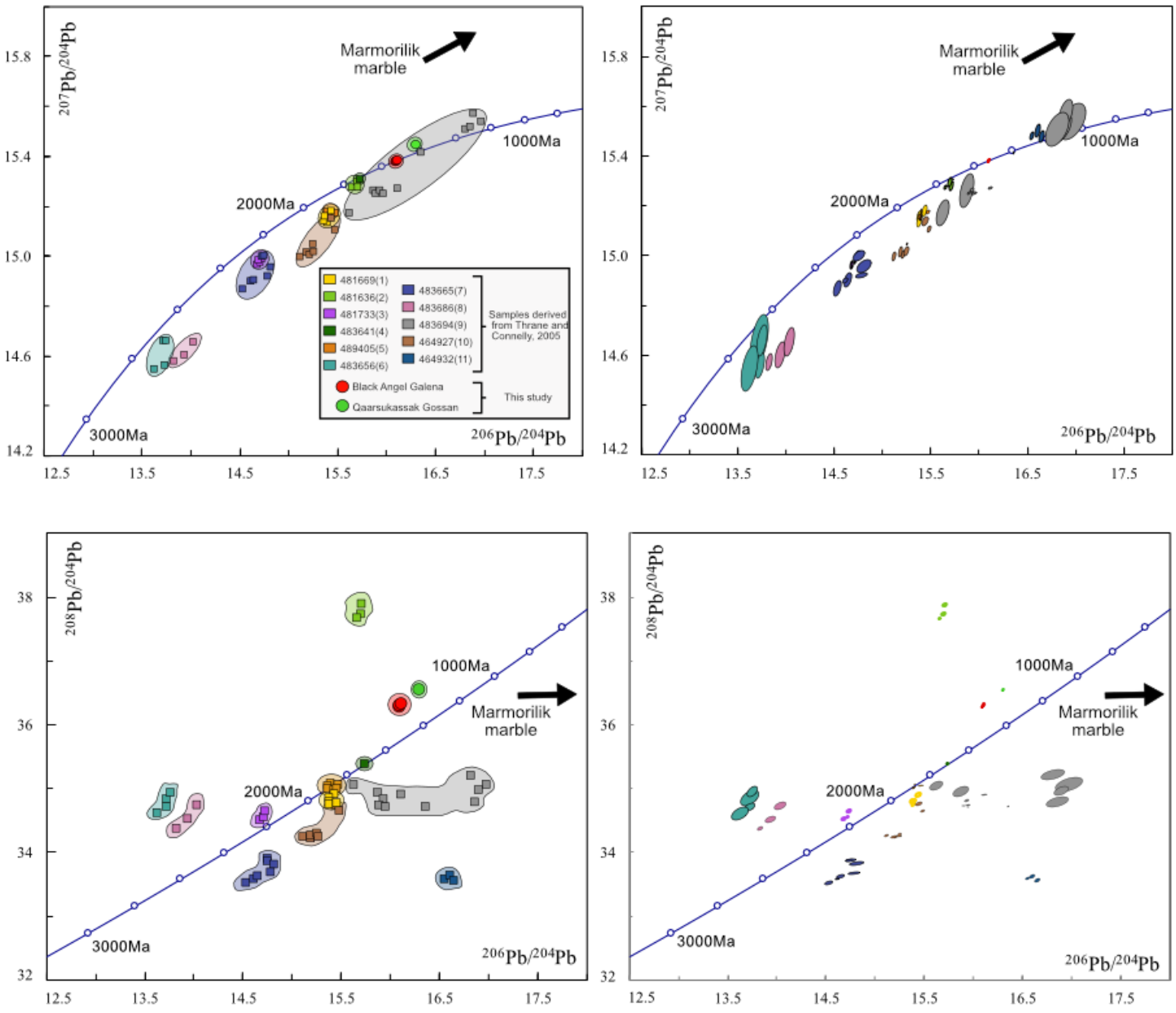

Figure 7.6 Plots of $^{207}Pb/^{204}Pb$ vs. $^{206}Pb/^{204}Pb$ and $^{208}Pb/^{204}Pb$ vs. $^{206}Pb/^{204}Pb$ for carbonate-hosted Pb-Zn occurrences in the Karrat Group, calculated using Isoplot/Ex (Ludwig, 2003). Square samples represent various basement Pb isotopic compositions (Thrane and Connelly, 2005), circle dots represent this study's samples and the Marmorilik marble samples (Taylor and Kalsbeek, 1990) are out of view in the direction of the arrow. Evolution curve from crustal Pb after Stacy and Kramers (1975). Legend: Numbers in parentheses refer to the map localities shown in Figure 4.3b. Error ellipses are 2σ.

An ore body with homogenous Pb isotopic composition could be formed from a single and homogenous source rock. Alternatively, it is difficult to evaluate the number of sources involved in an ore body that has undergone a homogenization event. Using available Pb isotopic data from the literature (Thrane and Connelly, 2005; Taylor and Kalsbeek, 1900), however, can aid in defining potential source rocks for the Pb in the Marmorilik galena prior to the homogenization (Figure 7.7).

The Marmorilik marble from Taylor and Kalsbeek (1990) generates a relatively correlated regression (MSWD = 2.0), deriving an age of 1881 ± 20 Ma (Figure 7.7). This study will assume the regression line formed from the Marmorilik marble represents a depositional age rather than a metamorphic age. Values from the Marmorilik marble show similar U/Pb ratios as other pristine carbonates from both marine and lacustrine settings (Rasbury et al., 2009), making it a reasonable assumption that the Marmorilik carbonate was original and not a later fluid flow event. Additionally, recent detrital zircon ages constraining the minimum age of the Marmorilik Formation to 1869 ± 14 Ma (M. McConnell, pers. comm.) argues against the previous interpretation that this represents a metamorphic age (further discussion in Chapter 7.3.3).

The regression line defined by the galena represents a mixing line at the time of homogenization (~1.83 Ga). This line does not match the heterogeneous data from the local basement, however it does intersect some of the values from local basement (Figure 7.7), creating a possible end member of the mixing line. Using the regression line from the Marmorilik carbonates, an intersection can be found crossing the mixing line from the galena samples (Figure 7.7). Assuming the carbonate Pb was derived from continental weathering (e.g., from local basement), this intersection could represent an average initial isotopic ratio for the marble that was derived from local basement (Jahn and Cuvellier, 1994; Ovchinnikova et al., 1995). This assumed isotopic ratio could then represent another end member of the local basement, suggesting that the local basement could be a likely source for the Pb in the mineralization at Black Angel Mine.

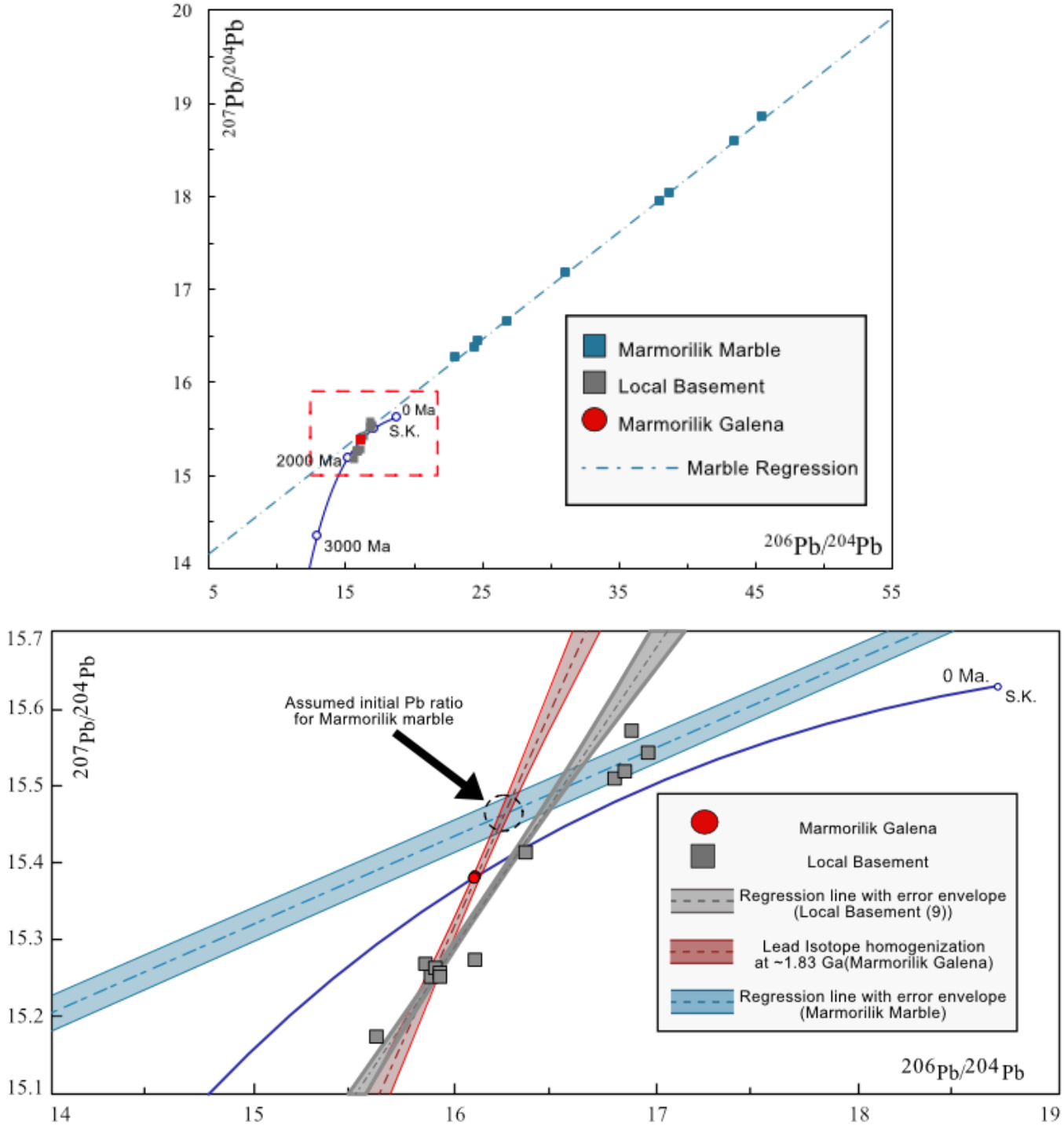

Figure 7.7 Comparative $^{207}Pb/^{204}Pb$ vs. $^{206}Pb/^{204}Pb$ diagrams, showing Pb isotopic compositions of galena from the Marmorilik Formation analyzed in this study, as well as local marble and basement samples from Taylor and Kalsbeek (1990) and Thrane and Connelly (2005), respectively. (Above) Zoomed-out look with annotated red square represent the second image; (Bottom) closer look at the intersection of each regression.

Evolution curve for crustal Pb after Stacy and Kramers (1975, "S.K."). Diagrams calculated using Isoplot/Ex (Ludwig, 2003) and Geodate software (Eglington and Harmer).

7.1.3 Implications on Re-Os geochronology

7.1.3.1 Re-Os abundances and initial Os isotope compositions

There is a difference in Re and Os isotopic abundances between the Qaarsukassak sample (569806) and the Banana ore zone samples (367918 and 367920) (Table 6.4). $^{187}Re/^{188}Os$ and $^{187}Os/^{188}Os$ ratios in Qaarsukassak sample are incredibly low (~58-60 and 2.822-2.834, respectively) compared to the Banana Ore zone samples (~880-1130 and 30.23-37.19, respectively). An explanation is needed for the large difference in the Re and Os systematics in the pyrites between the Marmorilik and Qaarsukassak Formation. Assuming the mineralization between the Marmorilik and Qaarsukassak is coeval, it is not uncommon for variable Re and Os abundances within a single sulfide deposit. A good analogy would be the Red Dog deposit with variable Re and Os abundances between the massive sulfide ore and vein ore (Morelli et al., 2004) or multiple sites of remobilized stratiform mineralization within the Howards Pass District, Yukon/Northwest Territories (Kelly et al., 2017). Based on the petrography and remobilized nature of the Black Angel deposit (Chapter 6), the radiogenic Re and Os values that the Banana Ore Zone exhibits could also suggest a disturbed Os isotopic signal.

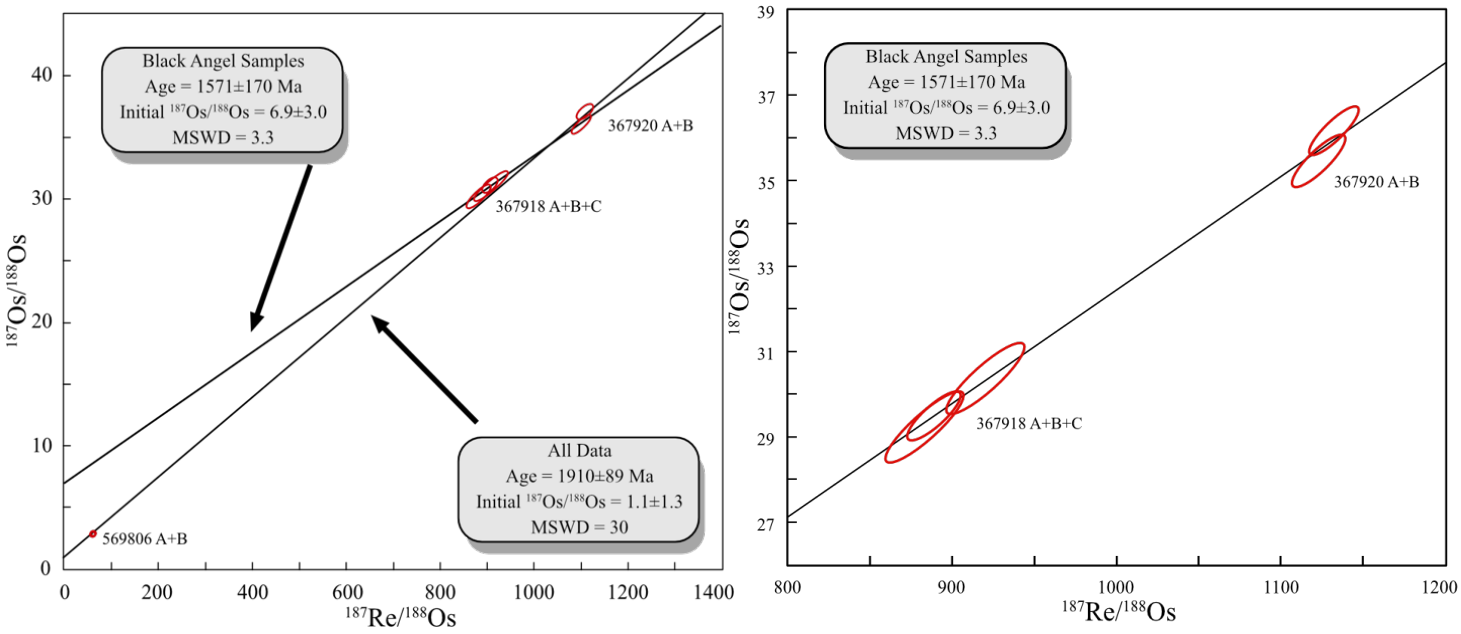

Figure 7.8. Re-Os isochron diagram showing data for ore pyrite samples (3 samples, 7 analyses), calculated by the use of Isoplot/Ex (Ludwig, 2003). (Left) Two regression ages using (a) both Qaarsukassak and Marmorilik samples and (b) using only samples from Marmorilik. (Right) Regression age using only samples from the Marmorilik Formation.

7.1.3.2 Age of Pb-Zn mineralization

Assuming coeval mineralization between the Qaarsukassak and Marmorilik mineralization, this study derived an indicated age of 1910 ± 89 Ma (MSWD = 30) (Figure 7.8). Unfortunately, this age heavily relies on the Qaarsukassak sample (569806), which anchors the regression line. Additionally, a younger indicated age of 1570 ± 170 Ma (MSWD = 3.3) can be derived using only the samples from the Marmorilik Formation (367918, 367920) (Figure 7.8), however, this age is incredibly imprecise and is implausible based on the previous age constraints for the Pb-Zn mineralization. It is questionable to suggest that the younger isochron age using only Marmorilik samples (1570 ± 170 Ma) represents a remobilized age with an MSWD = 3.3, however, based on textural observations, model ages and Os values it is probable that the ore in the Banana Zone has been disturbed with respect the Re-Os system. Ages derived from the isochrons are beyond analytical uncertainty (MSWD = 3.3-30) and should be interpreted with caution. However, using the initial $^{187}Os/^{188}Os$ calculated from the pyrite Re-Os isochron regression lines (1.1 ± 1.3),

the model ages can be corrected. This can be achieved using the Re-Os isochron equation, shown in Chapter 4.3. The calculated model ages with this initial $^{187}Os/^{188}Os$ ratio derives an average age of 1919 ± 44 Ma, thus giving a maximum age constraint for the Pb-Zn mineralization for the Marmorilik and Qaarsukassak formations.

8.0 Conclusions

8.1 Conclusions for the Marmorilik and Qaarsukassak mineralization

8.1.1 Field/ Petrographic conclusions

Structural measurements were made on fold limbs throughout the Qaarsukassak Formation. Measurements indicate a trend towards ~135°-155° (Figure 6.1), consistent to the trend of the D3 compressional event, which is roughly NW-SE. Remobilized massive sulfide minerals appear to be concentrated within these folds, which is similar to the deformation recorded in the Marmorilik mineralization (Pedersen, 1980,1981). This observation suggests that the Qaarsukassak mineralization is comparable to the Marmorilik mineralization in that they are both structurally controlled by the same deformation event. The significance of this is either that the two units could have coeval mineralization events or at least constrains the mineralization in both formations to have occurred prior to the D3 deformation event.

Petrographic observations suggest a sulfide remobilization phase occurred after the Pb-Zn mineralization, in both the Marmorilik and Qaarsukassak Formation. Evidence for remobilization includes: deformed textures on sphalerite and galena, cross-cutting relationships and the presence of porphyroclastic and derchwerbegung textures on pyrite grains in many of the ore zones. However, it is unclear if there was a second mineralization phase (apart from recrystallized remobilized sulfides like sphalerite, galena and chalcopyrite) prior to or during deformation, though two pyrite phases were identified in this study.

Based on Pedersen's (1981) study on the Black Angel mineralization, the Pb-Zn mineralization was interpreted initially to be a widespread, layered sulfide ore body. Evidence for this includes distinct pyrite rich layers and bands with sphalerite and galena in the thicker, less deformed parts of the ore body (observed by Pedersen and not confirmed in this study). This banding parallels the layering of intercalated graphite-bearing dolomite laminae and enclosed marble. Additionally, a rhythmic or alternating pattern between sulfide and carbonate layers has been reported in some parts of the mine. Other evidence includes interpreted rogenpyrite in the banded ore, suggesting a syn-sedimentary/diagenetic origin. Later events subsequently deformed, and remobilized the layered ore, consequently creating multiple ore regions such as: massive ore, porphryoclastic ore, and remobilized ore (Figure 3.4), with a gradational relationship between each region.

Archive samples from the Black Angel Mine used in this study were documented as being from the "porphryoclastic ore" zone. This limits the paragenetic sequence interpretation of the Black Angel Mine as the samples show obvious evidence of remobilization and deformation, which likely erased primary textures. However, based on the interpreted gradational relationship between each ore region and the layered ore in the thicker lesser deformed ore regions (Pedersen, 1980), an assumption could be made that the deformed porphryoclastic pyrite grains are either prior or coeval to the main Pb-Zn mineralization.

Horn et al. (in press) discuss hydrothermal breccia in some areas at Black Angel, suggesting MVT style textures and syn-to-post tectonic mineralization after the D3 deformation event. One needs to be cautious with this interpretation, since banded ore and rogenpyrite suggests a syn- to diagenetic origin (Pedersen, 1980) that could favor a SEDEX type model for this deposit, placing the timing of mineralization prior to deformation. Pedersen (1980) also noted that hydrothermal fracturing likely occurred during the remobilization/deformation of the ore as illustrated in in the Angel Ore Zone body in Figure 2.4. Unfortunately, petrography conducted in this study did not identify any textures supporting a second ore mineralization event during deformation other than the precipitated sulfides during remobilization and two generations of pyrite. Based on petrographic observations alone, it is unclear what type of deposit model best fits the Pb-Zn mineralization in the Marmorilik and Qaarsukassak formations.

8.1.2 Stable isotopic conclusions

The $\delta^{34}S$ data collected in the Marmorilik and Qaarsukassak formations display a narrow range between +0.2‰ and +7.2‰ (Figure 7.2). Large, non-recrystallized pyrite did not show any lateral variation within the grain (Figure 7.1). The $\delta^{34}S$ data suggest that the sulfur source for the mineralization is likely derived from seawater sulfate. This interpretation is reinforced with the evolution of the isotopic composition of deposit sulfides and the secular seawater sulfate curve throughout geological time (Figure 7.4). The range of $\delta^{34}S$ data suggests the sulfide minerals were produced dominantly through bacterial sulfate reduction with a mixture of thermochemical sulfate reduction. Rosa et al. (2017) suggested evaporites as a possible source of sulfur, which is common in MVT deposits. Evaporites as a source of sulfur to the Black Angel deposit is unlikely as sulfur derived from evaporites would yield heavier values than the $\delta^{34}S$ sulfur data in this study.

Additionally, comparing the data with other known sedimentary-hosted deposits, the data in this study is analogous to other SEDEX deposits (Figure 7.4).

New Pb-Pb data show a homogenous signature between samples of the Marmorilik Formation. The regression from this data did not yield a meaningful geological age, rather, it is assumed the regression line represents a mixing line. By comparison with Pb isotopic data in the literature (Thrane and Connelly, 2005; Taylor and Kalsbeek, 1990), the Pb-Pb data suggest that local basement is a probable source for the Pb in the mineralization. A homogenous signature could suggest either a single source or a homogenized source that contains multiple Pb sources, transported in a hydrothermal fluid. Therefore, it is difficult to evaluate the number of potential sources involved in an ore body that exhibits a relatively homogenous Pb isotope signature.

The Pb-Pb isotopic composition of a gossan interpreted to belong to the Qaarsukassak Formation is slightly more radiogenic than the three galena samples from the Marmorilik Formation. Based on the hypothesis in Chapter 1, this would suggest that the mineralization in the Qaarsukassak Formation is different than the Marmorilik Formation. However, the gossan sample did not yield a high Pb content like the galena samples when analyzed on the MC-ICP-MS, inferring no galena was present in the sample analyzed. It cannot be determined from the Pb-Pb isotopes whether or not mineralization in the two formations was coeval, however, the data in this study suggest that the sources of Pb could be different. Further work, such as finding a better sample with confirmed galena, would be needed to determine if the source(s) of Pb for both formations are co-genetic.

8.1.3 Implications on age constraints on the Pb-Zn mineralization

The depositional age of units of the Karrat Group are not well constrained (Chapter 2). A whole-rock Pb-Pb age on marble (1881± 20 Ma) from the Marmorilik Formation (Taylor and Kalsbeek, 1990) was previously interpreted to represent regional metamorphism, but conflicts with a preliminary youngest detrital zircon age (1869 ± 14 Ma) from the upper Marmorilik Formation (M. McConnell, pers. comm). This suggests the Pb-Pb age on the marble might be closer to a depositional age than a metamorphic age. Therefore, it seems reasonable to assume an age of ~1.88 to 1.87 Ga for the host rock of the Pb-Zn mineralization in the Marmorilik Formation. The two ages obtained from the Re-Os isochron are imprecise due to analytical uncertainty, but the oldest

concordant model age constrains the maximum age of the Pb-Zn mineralization to 1919 ± 44 Ma. This maximum age constraint is similar to the depositional age of the Marmorilik Formation. Based on field and petrographic observations, the mineralization crystallized prior to deformation and was subsequently remobilized and folded, trending along the D3 deformation. The D3 deformation is assumed to be coeval with peak metamorphism, dated at ~1830-1760 Ma (Sanborn-Barrie et al., 2017; Kirkland et al., 2017). This suggests that the minimum age for the Pb-Zn mineralization is prior to the deformation/metamorphic event ~1830 Ma.

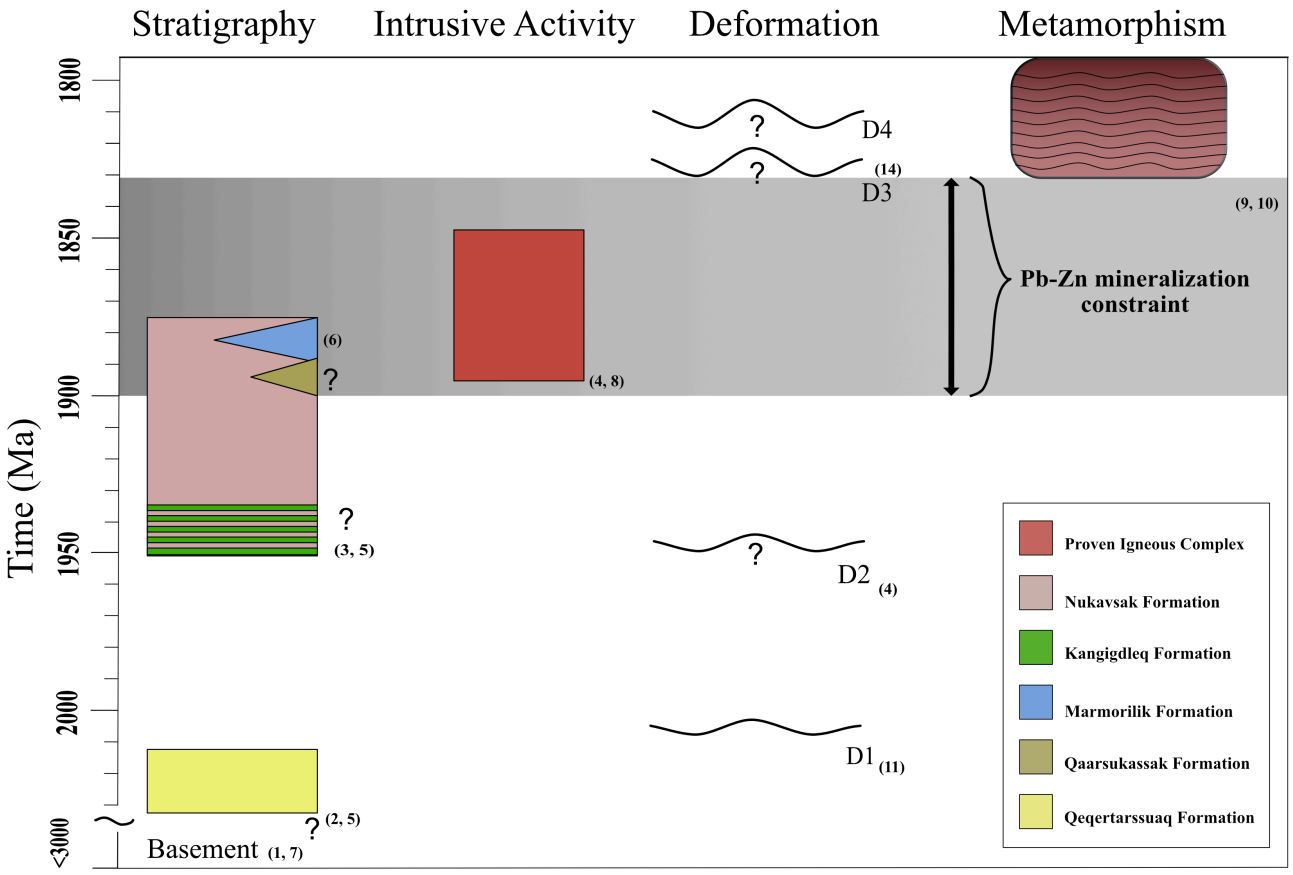

Figure 8.9 Revised schematic diagram showing a possible time-frame for the Pb-Zn mineralization to occur. Accompanied are the relative and absolute age constraints within the Karrat Group. Important differences from Figure 3.7 include: changing the timing of the D3 deformation, now coeval with metamorphism; confirming an age range for the Marmorilik Formation (this study); and extending the maximum age constraint for the Upper Marmorilik (M. McConnell, pers. comm). References can be found in Figure 3.7. Error bars for absolute ages not included.

8.1.4 Implications for a deposit model

Defining a deposit model for the Black Angel is challenging, given polyphase deformation of the orebodies. Both SEDEX and MVT type deposit models have both been suggested for the Black Angel Mine (Rosa et al., 2017; Pedersen, 1980; Thomassen, 2006). Using the new data generated in this study, the following summarizes the main conclusions with respect to specific deposit models described in Table 2.1.

While carbonate-dominated host rocks have been a typical characteristic for MVT deposits around the globe (and previously described as such for the Black Angel Mine), SEDEX deposits can be hosted in carbonates as well (Leach et al., 2005), making it an inadequate argument for a MVT model. The Black Angel Mine has also been interpreted (Pedersen 1980,1981) to have stratiform banded and massive ores in lesser deformed areas of the mine, suggesting a syngenetic/diagenetic hydrothermal process. Conversely, local "breccia textures" surrounding angular and folded marble fragments has been used to suggest that ore deposition was synchronous with or postdates regional deformation (Horn et al., in press). The petrographic observations in this study are not conducive to solving this debate, nor is it possible to distinguish whether there were multiple mineralization events, however, the petrographic and field observations suggest that the Pb-Zn mineralization was prior to or synchronous with the main deformation within the Karrat Group.

Rosa et al. (2017) proposed a MVT style of mineralization based on the presence of anhydrite in the Marmorilik Formation. However, $\delta^{34}S$ data in this study suggest seawater sulfate to be the likely source of sulfur, which was reduced via BSR and TSR processes, typical for SEDEX style of mineralization. The $\delta^{34}S$ sulfur data in this study is analogous to other SEDEX deposits when comparing it to other known sedimentary-hosted deposits throughout geologic time (Figure 7.3). Additionally, Horn et al. (in press) suggests that the anhydrite is unlikely to reflect the source of sulfur due to the anhydrites' close proximity to the ore deposit and other formations of the Karrat Group not containing any evaporites, thus favouring a SEDEX type of deposition.

Pb-Pb analysis on galena from the Marmorilik Formation yields a homogenous signature from three separate ore zones. This would suggest that the Marmorilik Formation mineralization would be favorable to a SEDEX type model in contrast to an MVT model, which are typically characterized by anomalous radiogenic linear trends that do not fit standard evolution models

(Heyl et al., 1996). However, a homogenous signature can suggest either a single source or a homogenization of multiple sources. Therefore, it is difficult to evaluate the number of possible sources involved in an ore body that exhibits a relatively homogenous Pb isotope signature (i.e. SEDEX vs. MVT mineralization).

This study constrains the Pb-Zn mineralization age between ~1900 Ma and 1830 Ma (Figure 7.9). This large time span (>70 million years) does not resolve the question of whether the mineralization is syngenetic, diagenetic, or epigenetic with respect to the presumed host rock age (~1.88 to 1.87 Ga), which would indicate if the Pb-Zn mineralization is a SEDEX or MVT type of deposit.

In conclusion, this study provides new insights into the Pb-Zn mineralization, however, it cannot ultimately resolve the origin of ore deposition of the Marmorilik Formation (i.e. the Black Angel Mine) nor the Qaarsukassak Formation. The sulfur isotope results, however, favor a SEDEX type model.

8.2 Future work

The petrographic observations did not unambiguously indicate multiple mineralization events. Further petrographic studies involving all the ore zones/ facies as well as re-assessing the presence of rogenpyrite, interpreted by Pedersen (1980) would help bolster the structural understanding of the ore deposition.

The results of sulfur analyses of pyrite grains from deformed ore zones lack certain controls to better understand the possible mechanisms involved (e.g. TSR, BSR, etc.). Further investigations on samples from lesser deformed areas of the Black Angel Mine would be interesting to compare as the undeformed pyrite might reveal greater variation in sulfur values that the results in this study.

The interpretations on Pb-Pb data are highly speculative at this stage and further information on the all the potential sources is required to support the model. Future analyses focused on galena in the Qaarsukassak could resolve if the mineralization is coeval to the Marmorilik Formation. Further work could utilize the Rb-Sr isotopic system. Rb-Sr geochronology of sphalerites have been beneficial in various of sedimentary-hosted deposits and

could decisively help to resolve the age relationships and constrain the origin of metals (Tillber et al., 2017; Christensen et al., 1995).

9.0 References

Bachinski DJ (1969) Bond strength and sulfur isotopic fractionation in coexisting sulfides. Econ Geol 64:56–65. doi: 10.2113/gsecongeo.64.1.56

Barton Jr. PB, Bethke PM (1987) Chalcopyrite disease in sphalerite: pathology and epidemiology. Am Mineral 72:17

Berner RA (1989) Biogeochemical cycles of carbon and sulfur and their effect on atmospheric oxygen over phanerozoic time. Glob Planet Change 1:97–122. doi: 10.1016/0921-8181(89)90018-0

Bradley DC, Leach DL (2003) Tectonic controls of Mississippi Valley-type lead–zinc mineralization in orogenic forelands. Miner Deposita 38:652–667

Brenan JM, Cherniak DJ, Rose LA (2000) Diffusion of osmium in pyrrhotite and pyrite: implications for closure of the Re–Os isotopic system. Earth Planet Sci Lett 180:399–413. doi: 10.1016/S0012-821X(00)00165-5

Cardozo N, Allmendinger RW (2013) Spherical projections with OSXStereonet. Comput Geosci 51:193–205. doi: 10.1016/j.cageo.2012.07.021

Carne RC, Cathro RJ (1981) Sedimentary exhalative (sedex) zinc-lead-silver deposits, northern Canadian Cordillera. Archer, Cathro & Associates

Christensen J.N, Halliday Ian, Leigh K, et al Direct dating of sulfides by Rb-Sr: A critical test using the Polaris Mississippi Valley-type Zn-Pb deposit. 7

Connelly JN, Thrane K (2005) Rapid determination of Pb isotopes to define Precambrian allochthonous domains: An example from West Greenland. Geology 33:953–956. doi: 10.1130/G21720.1

Connelly JN, Thrane K, Krawiec AW, Garde AA (2006) Linking the Palaeoproterozoic Nagssugtoqidian and Rinkian orogens through the Disko Bugt region of West Greenland. J Geol Soc 163:319–335. doi: 10.1144/0016-764904-115

Cook NJ, Hoefs J (1997) Sulphur isotope characteristics of metamorphosed Cu (Zn) volcanogenic massive sulphide deposits in the Norwegian Caledonides. Chem Geol 135:307–324. doi: 10.1016/S0009-2541(96)00119-2

Coppard J, Swatton S, Harris CJ (1992) Karrat exclusive exploration licence. 1992 year end report, 19 pp. Unpubl Rep RTZ Min Explor Ltdin Arch Geol Surv Den Greenl GEUS Rep File 21297

Corfu F, Andersen TB, Gasser D (2014) The Scandinavian Caledonides: main features, conceptual advances and critical questions. Geol Soc Lond Spec Publ 390:9–43. doi: 10.1144/SP390.25

Craig JR, Vokes FM, Solberg TN (1998) Pyrite: physical and chemical textures. Miner Deposita 34:82–101. doi: 10.1007/s001260050187

Crowe DE, Vaughan RG (2015) Characterization and use of isotopically homogeneous standards for in situ laser microprobe analysis of 34S/32S ratios. Am Mineral 81:187–193. doi: 10.2138/am-1996-1-223

Delevaux MH, Doe BR, Brown GF (1967) Preliminary lead isotope investigations of brine from the Red Sea, galena from the Kingdom of Saudi Arabia, and galena from United Arab Republic (Egypt). Earth Planet Sci Lett 3:139–144

Deloule E, Allegre CJ, Doe BR (1986) Lead and sulfur isotope microstratigraphy in galena crystals from mississippi valley-type deposits. Econ Geol 81:1307–1321. doi: 10.2113/gsecongeo.81.6.1307

Dickin AP (2005) Radiogenic Isotope Geology. Cambridge University Press

Eglington BM, Harmer RE Geodate For Windows Version 1: Isotope Regression and Modelling Software. 26

Escher JC, Pulvertaft TCR (1995) Geological map of Greenland: Copenhagen. Geological Survey of Greenland. Scale 1:500000

Farquhar J, Wu N, Canfield DE, Oduro H (2010) Connections between Sulfur Cycle Evolution, Sulfur Isotopes, Sediments, and Base Metal Sulfide Deposits. Econ Geol 105:509–533. doi: 10.2113/gsecongeo.105.3.509

Faure G (1986) Principles of isotope geology. Second edition

Garde AA, others (1978) The Lower Proterozoic Marmorilik Formation, east of Mârmorilik, West Greenland. Nyt Nordisk Forlag

Goodfellow WD (1987) Anoxic stratified oceans as a source of sulphur in sediment-hosted stratiform Zn-Pb deposits (Selwyn Basin, Yukon, Canada). Chem Geol Isot Geosci Sect 65:359–382. doi: 10.1016/0168-9622(87)90014-5

Goodfellow WD (2004) Sediment Hosted Lead-Zinc Sulphide Deposits. CRC Press

Goodfellow WD, Lydon JW (2007) Sedimentary exhalative (SEDEX) deposits. Miner Depos Can Synth Major Depos Types Dist Metallog Evol Geol Prov Explor Methods Geol Assoc Can Miner Depos Div Spec Publ 163–183

Goodfellow WD, Lydon JW, Turner RJW (1993) Geology and genesis of stratiform sediment-hosted (SEDEX) zinc-lead-silver sulphide deposits. Miner Depos Model Geol Assoc Can Spec Pap 40:201–251

Grocott J, McCaffrey KJW (2017) Basin evolution and destruction in an Early Proterozoic continental margin: the Rinkian fold–thrust belt of central West Greenland. J Geol Soc 174:453–467. doi: 10.1144/jgs2016-109

Grocott J, Pulvertaft TCR (1990) The Early Proterozoic Rinkian belt of central West Greenland. Early Proterozoic Trans-Hudson Orogen N Am Geol Assoc Can Spec Pap 37:443–463

Grotzinger JP (1989) Facies and Evolution of Precambrian Carbonate Depositional Systems: Emergence of the Modern Platform Archetype

Guarnieri P, Partin CA, Rosa D (2016) Palaeovalleys at the basal unconformity of the Palaeoproterozoic Karrat Group, West Greenland. Geol Surv Den Greenl Bull 63–66

Gulson BL, Porritt PM (1987) Base metal exploration of the Mount Read Volcanics, western Tasmania; Pt. II, Lead isotope signatures and genetic implications. Econ Geol 82:291–307. doi: 10.2113/gsecongeo.82.2.291

Harrison AG, Thode HG (1957) The kinetic isotope effect in the chemical reduction of sulphate. Trans Faraday Soc 53:1648–1651

Henderson G, Pulvertaft TCR (1967) The stratigraphy and structure of the Precambrian rocks of the Umanak area, West Greenland

Henderson G, Pulvertaft TCR (1987) Geological map of Greenland, 1: 100 000, Mârmorilik 71 V. 2 Syd. Nûgâtsiaq

Heyl AV, Landis GP, Zartman RE (1974) Isotopic evidence for the origin of Mississippi Valley-type mineral deposits: A review. Econ Geol 69:992–1006

Hitzman MW, Large D (1986) A review and classification of the Irish carbonate-hosted base metal deposits. Geol Genes Miner Depos Irel Dublin Ir Assoc Econ Geol 217–238

Ho SE, McNaughton NJ, Groves DI (1994) Criteria for determining initial lead isotopic compositions of pyrite in Archaean lode-gold deposits: a case study at Victory, Kambalda, Western Australia. Chem Geol 111:57–84. doi: 10.1016/0009-2541(94)90082-5

Holmes A (1946) An estimate of the age of the earth. Nature 157:680–684

Hu G, Rumble D, Wang P-L (2003) An ultraviolet laser microprobe for the in situ analysis of multisulfur isotopes and its use in measuring Archean sulfur isotope mass-independent anomalies. Geochim Cosmochim Acta 67:3101–3118

Jahn B, Cuvellier H (1994) Pb Pb and U Pb geochronology of carbonate rocks: an assessment. Chem Geol 115:125–151. doi: 10.1016/0009-2541(94)90149-X

Kajiwara Y, Krouse HR (1971) Sulfur Isotope Partitioning in Metallic Sulfide Systems. Can J Earth Sci 8:1397–1408. doi: 10.1139/e71-129

Kalsbeek F (1981) The northward extent of the Archaean basement of Greenland — a review of Rb Sr whole-rock ages. Precambrian Res 14:203–219. doi: 10.1016/0301-9268(81)90039-5

Kalsbeek F, Pulvertaft TCR, Nutman AP (1998) Geochemistry, age and origin of metagreywackes from the Palaeoproterozoic Karrat Group, Rinkian belt, West Greenland. Precambrian Res 91:383–399

Kelley KD, Selby D, Falck H, Slack JF (2017) Re-Os systematics and age of pyrite associated with stratiform Zn-Pb mineralization in the Howards Pass district, Yukon and Northwest Territories, Canada. Miner Deposita 52:317–335. doi: 10.1007/s00126-016-0663-y

Kesler SE, Reich MH (2006) Precambrian Mississippi Valley–type deposits: Relation to changes in composition of the hydrosphere and atmosphere. Geol Soc Am Mem 198:185–204. doi: 10.1130/2006.1198(11)

Kirk J, Ruiz J, Chesley J, et al (2002) A major Archean, gold-and crust-forming event in the Kaapvaal Craton, South Africa. Science 297:1856–1858

Kiyosu Y, Krouse HR (1990) The role of organic acid in the abiogenic reduction of sulfate and the sulfur isotope effect. Geochem J 24:21–27

Large RR, Bull SW, McGoldrick PJ, Walters SG (2005) Stratiform and Strata-Bound Zn-Pb-Ag Deposits in Proterozoic Sedimentary Basins, Northern Australia. Econ Geol 100th:931–963

Leach D, Sangster D, Kelley K, et al (2005) Sediment-hosted lead-zinc deposits: A global perspective. Econ Geol 100th:561–607

Leach DL, Bradley D, Lewchuk MT, et al (2001) Mississippi Valley-type lead-zinc deposits through geological time: Implications from recent age-dating research. Miner Deposita 36:711–740

Leach DL, Bradley DC, Huston D, et al (2010) Sediment-Hosted Lead-Zinc Deposits in Earth History. Econ Geol 105:593–625. doi: 10.2113/gsecongeo.105.3.593

Leach DL, Sangster DF (1993) Mississippi Valley-type lead-zinc deposits. Miner Depos Model Geol Assoc Can Spec Pap 40:289–314

Li Y, Selby D, Feely M, et al (2016) Fluid inclusion characteristics and molybdenite Re-Os geochronology of the Qulong porphyry copper-molybdenum deposit, Tibet. Miner Deposita 1–22

Ludwig KR (2003) User's manual for IsoPlot 3.0. Geochronological Toolkit Microsoft Excel 71:

Lyons TW, Gellatly AM, McGoldrick PJ, Kah LC (2006) Proterozoic sedimentary exhalative (SEDEX) deposits and links to evolving global ocean chemistry. Geol Soc Am Mem 198:169–184. doi: 10.1130/2006.1198(10)

Machel HG, Krouse HR, Sassen R (1995) Products and distinguishing criteria of bacterial and thermochemical sulfate reduction. Appl Geochem 10:373–389. doi: 10.1016/0883-2927(95)00008-8

Mathur R, Ruiz J, Tornos F (1999) Age and sources of the ore at Tharsis and Rio Tinto, Iberian Pyrite Belt, from Re-Os isotopes. Miner Deposita 34:790–793

Morelli RM, Bell CC, Creaser RA, Simonetti A (2010) Constraints on the genesis of gold mineralization at the Homestake Gold Deposit, Black Hills, South Dakota from rhenium–osmium sulfide geochronology. Miner Deposita 45:461–480. doi: 10.1007/s00126-010-0284-9

Morelli RM, Creaser RA, Selby D, et al (2004) Re-Os Sulfide Geochronology of the Red Dog Sediment-Hosted Zn-Pb-Ag Deposit, Brooks Range, Alaska. Econ Geol 99:1569–1576. doi: 10.2113/gsecongeo.99.7.1569

Neuerburg GJ (1975) Procedure, Using Hydrofluoric-Acid, For Quantitative Mineral Separations From Silicate Rocks. J Res Us Geol Surv 3:377–378

Ohle EL (1980) Some considerations in determining the origin of ore deposits of the mississippi valley type; Part II. Econ Geol 75:161–172. doi: 10.2113/gsecongeo.75.2.161

Ohmoto H (1972) Systematics of sulfur and carbon isotopes in hydrothermal ore deposits. Econ Geol 67:551–578

Ohmoto, H., 1986. Stable isotope geochemistry of ore deposits. In: Valley, J.W., Taylor, H.P., O'Neill, J.R. (Eds.), Stable Isotopes in High Temperature Geological Processes. Reviews in Mineral- ogy, vol. 16. Mineralogical Society of America, Washington, DC, pp. 491–599.

Ohmoto H, Goldhaber MB (1997) Sulfur and carbon isotopes. Geochem Hydrothermal Ore Depos 3:517–611

Parr JM, Stevens BPJ, Carr GR, Page RW (2004) Subseafloor origin for Broken Hill Pb-Zn-Ag mineralization, New South Wales, Australia. Geology 32:589–592. doi: 10.1130/G20358.1

Pedersen FD (1980) Remobilization of the massive sulfide ore of the Black Angel Mine, central West Greenland. Econ Geol 75:1022–1041. doi: 10.2113/gsecongeo.75.7.1022

Pedersen FD (1981) Polyphase deformation of the massive sulphide ore of the Black Angel Mine, central West Greenland. Miner Deposita 16:157–176. doi: 10.1007/BF00206461

Rosa D, Guarnieri P, Partin CA, et al (2016) Architecture and mineral potential of the Paleoproterozoic Karrat Group, West Greenland - Results of the 2015 season.

Rosa D, Guarnieri P, Partin CA, et al (2017) Architecture and mineral potential of the Paleoproterozoic Karrat Group, West Greenland - Results of the 2016 season.

Rye RO, Ohmoto H (1974) Sulfur and carbon isotopes and ore genesis: a review. Econ Geol 69:826–842

Sakai H (1968) Isotopic properties of sulfur compounds in hydrothermal processes. Geochem J 2:29–49. doi: 10.2343/geochemj.2.29

Sanborn-Barrie M, Thrane K, Wodicka N, Rayner N (2017) The Laurentia – West Greenland connection at 1.9Ga: New insights from the Rinkian fold belt. Gondwana Res 51:289–309. doi: 10.1016/j.gr.2017.07.002

Sangster, D.F (1990) Mississippi Valley Type and sedex lead-zinc deposits: A comparative examination. Trans Teh Inst Min Metall Sec B 99:B-21-B-42

Sasaki A, Krouse HR (1969) Sulfur isotopes and the Pine Point lead-zinc mineralization. Econ Geol 64:718–730. doi: 10.2113/gsecongeo.64.7.718

Schwarcz HP, Burnie SW (1973) Influence of sedimentary environments on sulfur isotope ratios in clastic rocks: a review. Miner Deposita 8:264–277. doi: 10.1007/BF00203208

Seal RR (2006) Sulfur Isotope Geochemistry of Sulfide Minerals. Rev Mineral Geochem 61:633–677. doi: 10.2138/rmg.2006.61.12

Selby D, Creaser RA, Fowler MG (2007) Re–Os elemental and isotopic systematics in crude oils. Geochim Cosmochim Acta 71:378–386. doi: 10.1016/j.gca.2006.09.005

Singer DA (1995) World class base and precious metal deposits; a quantitative analysis. Econ Geol 90:88–104

Smoliar MI, Walker RJ, Morgan JW (1996) Re-Os Ages of Group IIA, IIIA, IVA, and IVB Iron Meteorites. Science 271:1099–1102. doi: 10.1126/science.271.5252.1099

Snyder FG (1967) Criteria for origin of stratiform ore bodies with application to southeast Missouri.

Stacey JS, Kramers JD (1975) Approximation of terrestrial lead isotope evolution by a two-stage model. Earth Planet Sci Lett 26:207–221. doi: 10.1016/0012-821X(75)90088-6

Stein HJ, Markey RJ, Morgan JW, et al (2001) The remarkable Re–Os chronometer in molybdenite: how and why it works. Terra Nova 13:479–486

St-Onge MR, Gool JAMV, Garde AA, Scott DJ (2009) Correlation of Archaean and Palaeoproterozoic units between northeastern Canada and western Greenland: constraining the pre-collisional upper plate accretionary history of the Trans-Hudson orogen. Geol Soc Lond Spec Publ 318:193–235. doi: 10.1144/SP318.7

Tang Y-Y, Bi X-W, Fayek M, et al (2014) Microscale sulfur isotopic compositions of sulfide minerals from the Jinding Zn–Pb deposit, Yunnan Province, Southwest China. Gondwana Res 26:594–607. doi: 10.1016/j.gr.2013.07.021

Taylor RD, Leach DL, Bradley DC, Pisarevsky SA (2009) Compilation of mineral resource data for Mississippi Valley-type and clastic-dominated sediment-hosted lead-zinc deposits

Thomassen B (1991) The Black Angel lead-zinc mine 1973–90. Rapp Grønl Geol Unders 152:46–50

Thomassen B (2003) The Black Angel lead-zinc mine at Maarmorilik in West Greenland. Geol Ore 2:1–12

Thorne KG, Fyffe LR, Creaser RA (2013) Re-Os geochronological constraints on the W-Mo mineralizing event in the Mount Pleasant Caldera Complex: implications for the timing of subvolcanic magmatism and caldera development

Thrane K, Baker J, Connelly J, Nutman A (2005) Age, petrogenesis and metamorphism of the syn-collisional Prøven Igneous Complex, West Greenland. Contrib Mineral Petrol 149:541–555

Thrane K, Connelly JN, Garde AA, et al (2003) Linking the Palaeoproterozoic Rinkian and Nagssugtoqidian belts of central West Greenland: implications of new U-Pb and Pb-Pb zircon ages. p 9275

Tillberg M, Drake H, Zack T, et al (2017) In Situ Rb-Sr Dating of Fine-grained Vein Mineralizations Using LA-ICP-MS. Procedia Earth Planet Sci 17:464–467. doi: 10.1016/j.proeps.2016.12.117

Vokes FM (1969) A review of the metamorphism of sulphide deposits. Earth-Sci Rev 5:99–143. doi: 10.1016/0012-8252(69)90080-4

Vokes FM (1993) The metamorphism of pyrite and pyritic ores: an overview. Miner Mag 57:3–18

Von Gehlen K, Nielsen H, Chunnett I, Rozendaal A (1983) isotopes in metamorphosed Precambrian sulphides and baryte at Aggeneys Gamsberg, South Africa. Mineral Mag 47:481–6

Walker RJ, Morgan JW (1989) Rhenium-Osmium Isotope Systematics of Carbonaceous Chondrites. Science 243:519–522. doi: 10.1126/science.243.4890.519

Walker RN, Gulson B, Smith J (1983) The Coxco Deposit; a Proterozoic Mississippi Valley-type deposit in the McArthur River District, Northern Territory, Australia. Econ Geol 78:214–249. doi: 10.2113/gsecongeo.78.2.214

Whelan JF, Rye RO, deLorraine WF (1984) The Balmat-Edwards zinc-lead deposits; synsedimentary ore from mississippi valley-type fluids. Econ Geol 79:239–265. doi: 10.2113/gsecongeo.79.2.239

Wilkinson JJ (2014) 13.9-Sediment-Hosted Zinc–Lead Mineralization: Processes and Perspectives

Zheng YF (1990) Sulfur isotopes in metamorphic rocks. NEUES Jahrb Mineral-Abh 161:303–325

Zhimin Z, Yali S (2013) Direct Re-Os Dating of Chalcopyrite from the Lala Iocg Deposit in the Kangdian Copper Belt, China. Econ Geol 108:871–882. doi: 10.2113/econgeo.108.4.871

10.0 Appendix

Table 10.1 Sample localities for the preliminary sulfur isotopic analysis using conventional IRMS

Name	Sample no.	Mineral Analyzed	Latitude (N)	Longitude (W)	Brief Description
(NZ1) Nunngarut 1	367929	Pyrite	71.089	-51.269	"Buckshot"/Porphyroclastic ore
(NZ2) Nunngarut 2	367931	Pyrite	71.093	-51.266	"Buckshot"/Porphyroclastic ore
(AZ) Angel Zone	367904	Pyrite	71.125	-51.205	"Buckshot"/Porphyroclastic ore
(CZ) Cover Zone	367907	Pyrite	71.124	-51.062	"Buckshot"/Porphyroclastic ore
(BZ) Banana Zone	367918	Pyrite	71.112	-50.917	"Buckshot"/Porphyroclastic ore
(TZ) Tributary Zone	367921	Pyrite	71.138	-51.002	"Buckshot"/Porphyroclastic ore
(DIZ) Deep Ice Zone	367924	pyrite	71.137	-50.801	"Buckshot"/Porphyroclastic ore

Table 10.2 Sample localities for the main sulfur isotopic analysis using SIMS analysis

Name	Sample no.	Mineral Analyzed	Latitude (N)	Longitude (W)	Brief Description
(SLO) South Lakes Outcrop	569813	Pyrite, sphalerite	71.082	-51.009	Pb-Zn "boxwork" mineralizing outcrop
(DISC) Main Discovery Ore-Zone	572204-4	Pyrrhotite, Sphalerite	71.332	-51.439	Massive sphalerite with pyrrhotite
(DISC) Main Discovery Ore-Zone	572204-3	Pyrrhotite, Sphalerite	71.332	-51.439	Massive sphalerite with pyrrhotite
(AZ) Angel Zone	367904	Pyrite, Sphalerite	71.125	-51.205	"Buckshot"/Porphyroclastic ore
(QO) Qaarsukassak Outcrop	572201	Pyrite, Pyrrhotite, sphalerite	71.112	-50.917	Massive pyrite with sphalerite and pyrrhotite
(NZ2) Nunngarut 2	367931	Pyrite, Sphalerite	71.093	-51.266	"Buckshot"/Porphyroclastic ore

Table 10.3 Sample localities for the Pb-Pb analysis

Name	Sample no.	Mineral Analyzed	Latitude (N)	Longitude (W)	Brief Description
(AZ) Angel Zone	367904	Galena	71.125	-51.205	"Buckshot"/Porphyroclastic ore
(DIZ) Deep Ice Zone	367924	Galena	71.137	-50.801	"Buckshot"/Porphyroclastic ore
(IZ) Angel Zone	?	Galena	71.12236	-51.183	"Buckshot"/Porphyroclastic ore
(KS) Gossan area	572207	Gossan (Galena?)	71.188	-52.222	Gossan sample

Table 10.4 Sample localities for the Re-Os analysis

Name	Sample no.	Mineral Analyzed	Latitude (N)	Longitude (W)	Brief Description
(BZ) Banana Zone	367918	Pyrite	71.112	-50.917	"Buckshot"/Porphyroclastic ore
(BZ) Banana Zone	367918	Pyrite	71.112	-50.917	"Buckshot"/Porphyroclastic ore
Archive sample	367920	Pyrite	71.333	-51.439	Massive sulfide sample including pyrite and sphalerite

Table 10.5 Short Descriptions of photomicrography observations

Sample no.	Latitude (N)	Longitude (W)	Sulfide assemblage	Gangue minerals	Brief Description/ Observations	Notable Textural Remarks
367904 Angel Zone	71.089	-51.269	Sph>Py>> Gn	Qtz, Cb, Trem	Porphyroclastic pyrite with sphalerite and galena infilling void spaces	Pyrite annealing, carbonate brecciated Remobilization occurred
367907 Cover Zone	71.093	-51.266	Py>Sph>> Gn	Qtz, Cb, Trem	Porphyroclastic pyrite, sphalerite and galena replacing pyrite. Later stage carbonate appears to be replacing pyrite?	Pyrite fractures, pyrite annealing, Deformed carbonate. Remobilization occurred
367918 Banana Zone	71.125	-51.205	Sph>Py>Gn >>Cpy	Qtz, Cb, Trem, Chl	Porphyroclastic pyrite with a later, euhedral stage pyrite. Sphalerite and galena replace pyrite grains subsequently.	Well deformed pyrite grains in proximity to euhedral pyrite grains. Skeletal structures among pyrite grains Remobilization occurred
367921 Tributary Zone	71.124	-51.062	Sph>Py>> Gn >Cpy	Cb, Qtz, Trem,	Porphyroclastic pyrite, sphalerite and galena replacing pyrite	Fractured and Pyrite, Fractures include “inclusions”

						Remobilization occurred
367924 Deep Ice Zone	71.112	-50.917	Py>Sph>Gn >>Cpy	Cb, Qtz,	Porphyroclastic pyrite, sphalerite and galena replacing pyrite	Majority of pyrite is annealing to each other. Remobilization occurred
367929 Nunngarut Zone 1	71.138	-51.002	Py>Sph>> Gn >>Cpy	Cb, Qtz,	Porphyroclastic pyrite, sphalerite and galena replacing pyrite	Majority of pyrite is annealing to each other. Remobilization occurred
367931 Nunngarut Zone 2	71.093	-51.266	Sph>Py>Gn	Cb, Qtz, Trem, Gph	Well-rounded pyrite and carbonate grains with sphalerite, smaller pyrite and galena in the matrix	Derchwer begun texture Remobilization occurred
569813 South Lakes Outcrop (SLO)	71.082	-51.009	Sph>Py>Gn >>Cpy	Cb, Qtz, Trem,	Porphyroclastic pyrite, sphalerite and galena replacing pyrite; Carbonate clasts with foliation including pyrite	Marble clasts, Fractured pyrite grains Remobilization occurred
572201 Qaarsukas -sak Outcrop (QO)	71.112	-50.917	Py>>Po> Sph	Qtz	Massive pyrite with pyrrhotite and sphalerite crystallized within a fracture	-
572204 Discovery Outcrop (DISC)	71.332	-51.439	Sph>Po>> Py >Cpy	Qtz, Gph, Cb, Hem	Deformed sphalerite cross-cutting pyrrhotite; Minor amounts of pyrite and	Chalcopyrite disease Sphalerite deformed.

					chalcopyrite detected along sphalerite fractures; Clasts of host rock contain graphite and pyrrhotite with 2nd pyrrhotite phase cross-cutting the clasts	
572207	71.137	-50.801	Po	Qtz, Cb, Gph,	Disseminated pyrrhotite in host rock with graphite cross-cutting the host rock	-